

# Investigation of Electro-Nuclear Spin States in LiHoF<sub>4</sub> Using Cavity-Magnon-Polariton Technique

Présentée le 9 mars 2023

Faculté des sciences de base Laboratoire de magnétisme quantique Programme doctoral en physique

pour l'obtention du grade de Docteur ès Sciences

par

#### Yikai YANG

Acceptée sur proposition du jury

Prof. J. H. Dil, président du jury

Prof. H. M. Rønnow, Dr I. Zivkovic, directeurs de thèse

Prof. M. Müller, rapporteur

Prof. T. Rosenbaum, rapporteur

Prof. G. Aeppli, rapporteur

博观而约取,厚积而薄发 — 苏轼

To my wife, Kara M. Reich, and my parents, 杨青健 & 杨咸

## Acknowledgements

The author would like to give his first and foremost gratitude to Dr. Henrik M. Rønnow for his patient guidance and unreserved sharing of expertise over the years, owing to whom I enjoyed a perfect balance between freedom and supervision to explore freely but grow continuously, making the past four years the best career life I have had so far. I am also grateful for Dr. Richard Gaal for his consistent help and persistent friendship, which chased away many technical difficulties and relieved much of the burdens along this arduous path. A tip of the hat to Dr. Peter Babkevich for getting me up to speed early on, as well as his candid friendship, which hopefully will last far beyond this program. Many thanks also goes without saying to Dr. Ivica Živković for being there whenever I needed help and for his generous trust. Much appreciation for Dr. Markus Müller, whose persistence and patience kept many mistakes at bay in the process of finalizing this thesis. The author would also like to thank Dr. Colbois Jeanne, Dr. Virgile Favre, and Dr. Alexandra Turini for numerous inspiring discussions that have greatly broadened my horizon. Finally, saving my best gratitude for the last for my loving and beloved wife, Kara M. Reich, who has been the pillar and joy of my life, and who has enabled me to pursue my ideal while living happily in the moment.

Lausanne, February 16, 2023

Yikai Yang

### **Abstract**

LiReF<sub>4</sub> ("Re" stands for rare-earth element) and their doped derivatives have long been recognized as a family of compounds that exhibit rich phenomena in quantum magnetism, drawing wide attention to them from both fundamental researchers and industrial application designers. In particular, LiHoF4 is considered one of the best real-world realizations of the 3D dipolar Ising model, which is of tremendous importance in facilitating our understanding of quantum phase transition, critical behaviors, and magnetism in general. However, despite of decades of study, LiHoF4 is yet to be fully described and a thorough understanding of it is hindered by complications arising from its dominant long range interaction, many-body effect, and diverse inter-particle interactions. One particular example is the strong hyperfine interaction present in LiHoF<sub>4</sub> that has a plethora of physical consequences with unclear mechanisms in addition to the further split of electronic spin states. Partly due to the fact of that these finer electro-nuclear states lie above the operating frequency of conventional NMR, and below the energy resolution of most neutron scattering instrument, scarce reports exist on the investigation of the hyperfine splitting of electronic states in LiHoF<sub>4</sub>. In the present text, we take advantage of a high-finesse re-entrant cavity resonator to resolve these electro-nuclear spin states. In addition, by deriving an adequate theoretical description of the cavity-spin hybrid system under existing frameworks, we also make an attempt to understand their effects on some of the magnetic properties of LiHoF<sub>4</sub>.

### Résumé

Les matériaux de la famille des LiTRF4 ("TR" signifie Terre Rare) et leurs dérivés dopés sont reconnus depuis longtemps comme une famille de composés qui sont associés à une vaste de gamme de phénomènes liés au domaine du magnétisme quantique. Ils attirent particulièrement l'attention des chercheurs en science fondamentale et à la fois aussi des concepteurs d'applications industrielles. Le LiHoF4 est en particulier considéré comme l'une des meilleures réalisations expérimentales du modèle d'Ising dipolaire en trois dimensions, et relève donc d'une importance capitale dans l'amélioration de la compréhension des transitions de phase quantiques, des comportements critiques ainsi que du magnétisme en général. Cependant, en dépit de décennies d'études, il reste toujours à établir un modèle complet décrivant le LiHoF4 et sa compréhension approfondie est entravée par des complications résultant de l'interaction longue portée, dominante dans le système, d'effets de physique à plusieurs corps, et de diverses interactions entre particules. Un exemple de ces complications est la forte interaction hyperfine présente dans le LiHoF4 qui induit une pléthore de conséquences aux mécanismes abscons, s'ajoutant à la levée de dégénérescence des états électroniques de spin. Ces états fins électro-nucléaires sont associés à une fréquence caractéristique trop élevée pour être sondés par la Résonnance Magnétique Nucléaire (RMN), et ne sont pas non plus étudiables au travers de techniques habituelles de diffusion de neutrons, qui présentent une résolution en énergie trop grossière. Le manque d'adéquation des techniques expérimentales conventionnelles a considérablement limité le nombre d'études de la structure hyperfine du LiHoF<sub>4</sub>. Dans la dissertation ci-après, une cavité résonante réentrante à haute finesse est utilisée pour observer ces états de spin électro-nucléaires. De plus, en établissant une description théorique ad hoc du système hybride spin-cavité, un cadre général est établi, permettant une meilleure compréhension de certaines des propriétés magnétiques du LiHoF4...

# Contents

kno	wledgements	i
ostra	act (English/Français/Deutsch)	iii
Ove	erview of topics	1
1.1	Overview	1
1.2	${ m LiHoF_4}$ as a quantum magnet	2
1.3	Cavity magnonics	6
The	eoretical methods	9
2.1	Mean Field Approximation of Spin Hamiltonian	9
2.2	Dynamical Susceptibility	16
	2.2.1 Linear Response Theory	16
	2.2.2 Random Phase Approximation	21
2.3	Scattering Parameters	24
2.4	Input-Output Formalism	25
MF	-RPA model for LiHoF $_4$	35
3.1	Connection to the Ising models	35
	3.1.1 Ising model with exchange anisotropy	35
	3.1.2 Ising model with single-ion anisotropy	42
3.2	Mean Field Calculation for LiHoF <sub>4</sub>	47
3.3	RPA Calculation for LiHoF <sub>4</sub>	56
Exp	perimental setup	65
Exp	perimental results and discussion	71
5.1	Off-Resonance Results and Analysis	72
	5.1.1 Field-Ramping measurement ( $\sim 5~\mathrm{GHz}$ )	72
	5.1.2 Field-Ramping measurement (~ 2 GHz)	82
	2.1 2.2 2.3 2.4 MF 3.1 3.2 3.3 Exp	1.2 LiHoF <sub>4</sub> as a quantum magnet 1.3 Cavity magnonics  Theoretical methods 2.1 Mean Field Approximation of Spin Hamiltonian 2.2 Dynamical Susceptibility 2.2.1 Linear Response Theory 2.2.2 Random Phase Approximation 2.3 Scattering Parameters 2.4 Input-Output Formalism  MF-RPA model for LiHoF <sub>4</sub> 3.1 Connection to the Ising models 3.1.1 Ising model with exchange anisotropy 3.1.2 Ising model with single-ion anisotropy 3.2 Mean Field Calculation for LiHoF <sub>4</sub> 3.3 RPA Calculation for LiHoF <sub>4</sub> Experimental setup  Experimental results and discussion 5.1 Off-Resonance Results and Analysis 5.1.1 Field-Ramping measurement (~5 GHz)

vii

#### Contents

		0.1.0	Temperature-Ramping Measurement (~5 GHz)	88
	5.2	On-Re	esonance Results and Analysis	92
		5.2.1	Low Power Excitation	93
		5.2.2	High Power Excitation	104
6	Sur	nmary	& Outlook	109
A	MF	-RPA S	Susceptibility Tensor	113
В	CE	F para	meter choice	117
<u></u>	ırric	ulum	Vitae	129

# Contents

## 1 Overview of topics

#### 1.1 Overview

As a member of the LiReF<sub>4</sub> compound family that harbors rich physics[34, 79], LiHoF<sub>4</sub> has been the subject of intense research for decades[6, 32, 9, 13, 72] with a primary focus on its magnetic properties. Being a 3D insulating magnet, LiHoF4 exhibits a Curie temperature much lower than the boiling point of Helium-4 at 1.53 K[34, 51], below which and down to 0 K, LiHoF<sub>4</sub> enters an ordered state by spontaneous symmetry breaking where all of its electronic spins are ferromagnetically aligned. Moreover, as we shall see in details in later chapters that, the crystal electrostatic field (CEF) effect present in LiHoF<sub>4</sub> results in a doublet as its ground state and the first excited state lies far above it, and ultimately allows one to map the magnetic hamiltonian of LiHoF4 onto the Ising model[9]. Furthermore, when an external magnetic field is applied perpendicular to the crystallographic c-axis of LiHoF4, it induces quantum fluctuations in the spin ensemble, granting the magnetic system a quantum nature. These features of LiHoF4 made it one of the ideal naturally occurring candidates for studying the Ising model and its dynamic properties. Since an analytical solution to 3D Ising model is yet to be found, LiHoF4 is also under the spotlight as a potential platform for testing new theories on the topic. At large fields, the ferromagnetic order is destroyed when crossing the quantum critical points (QCP), a phenomenon known as quantum phase transition that is found in a plethora of many-body-systems. This provides yet another strong incentive for studying LiHoF4 with the aim of better understanding of quantum phase transition and related critical phenomena.

Moreover, the dominant contribution to the many-body effects in LiHoF4 is from the

long-range dipole-dipole interaction, which is roughly 10 times bigger than the exchange interaction[61]. Such a long-range interaction becomes intractable as the system size grows, and therefore very little about Ising models with a long-range interaction in the thermodynamic limit is known analytically. However, in the meantime, dipolar interaction is prevalent among magnetic systems and particularly strong for dense ensembles of large spins, the latter of which is desirable for applications in quantum computing. Therefore studying dipolar ferromagnetic systems such as  $LiHoF_4$  is not only of fundamental research interests, but also helps on the application end to illuminate effects that dipole-dipole interaction may have on the coherence time of qubit states, their decay dynamics and subjects alike.

Lastly, LiHoF<sub>4</sub> is also relevant to another vibrant field of condensed matter physics in the recent past, namely the study of random and disordered systems, where quench dynamics and glass transitions have attracted a lot of attention. Among all the systems, spin glass is one of the most prominent subjects that is still being actively studied to date, and it is reported that LiHoF<sub>4</sub> doped with non-magnetic ions such as Yttrium can experimentally realize such a system[62, 68, 58]. Furthermore, there are diverse and intriguing behaviors of LiHo<sub>x</sub>Y<sub>1-x</sub>F<sub>4</sub> at different levels of doping, with the most notably a decrease of magnetic phase transition temperature with increasing impurity concentration until it undergoes a spin-glass transition near  $x \sim 20\%[2, 27]$ . Once again, apart from the research interests in these systems at a fundamental level, some motivations for studying LiHo<sub>x</sub>Y<sub>1-x</sub>F<sub>4</sub> systems as well stems from their potential applications in the realm of quantum computing and quantum information due to its unique dynamical properties[26, 70].

#### 1.2 LiHoF<sub>4</sub> as a quantum magnet

Having been put under magnifying glass for decades, there had been a number of interesting experimental discoveries on LiHoF $_4$ . One important realization about LiHoF $_4$  as a 3D Ising magnet was that it isn't perfect in terms of its magnetic phase diagram which deviates quite appreciably from that of at ideal Ising model at low temperatures[9]. This is revealed by a direct comparison between the experimentally measured phase boundary of LiHoF $_4$  and the calculated phase boundary for an ideal Ising magnet, both of which are shown in figure 1.1(a) with the former plotted in solid circles and the latter in asterisks. The difference in critical fields at zero temperature measures to nearly 2 T by extrapolation, and is largely visible below 400 mK.

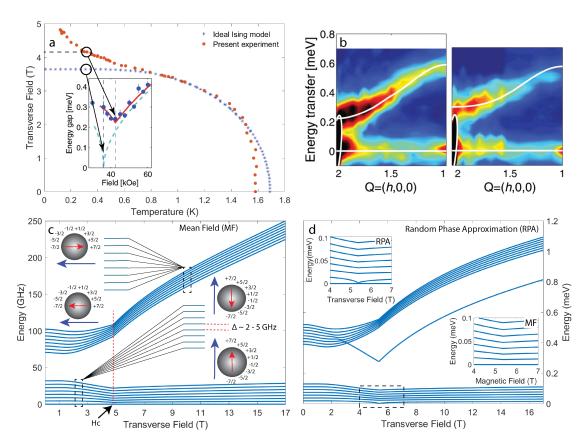


Figure 1.1: (a) Magnetic phase diagram of LiHoF<sub>4</sub>, solid markers are measured values from the present experiment. The dotted line is the calculated values for an ideal Ising magnet without hyperfine interaction. Inset: Lowest electronic excitation mode of LiHoF<sub>4</sub> measured (Solid markers) by inelastic neutron scattering experiment. The solid and dashed lines represent calculations of the excitation mode by 1/z expansion method with and without the inclusion of hyperfine interactions[40, 61]. Figure credit: Ref. [60]. (b) Measurement results at 300 mK on the excitation spectra of LiHoF<sub>4</sub> by inelastic neutron scattering at the critical field of 4.2 T (left panel) and 3.6 T (right panel). Figure credit: Ref. [60]. (c) Hyperfine splitting of the ground state doublet for the single-ion-hamiltonian of LiHoF<sub>4</sub>. Solid blue lines represent electro-nuclear spin states. The insets illustrate the electronic (blue arrows) and nuclear spin (red arrows) configurations in different ordering state (ferromagnetic or polarized paramagnetic) under a transverse magnetic field. (d) Reproduction of the RPA excitation modes from the ground state ( $|0\rangle \rightarrow |n\rangle$ ) from Ref. [48]. Insets: expanded view near the QCP of the lowest manifold of excitations.

The mechanism for this enhancement of critical field is well understood and attributed to the presence of hyperfine interaction, which will be detailed in later chapters. Here we only provide a hand-waving explanation: In  $\text{LiHoF}_4$ , all contributions to the net magnetic

moment come from the 4f electrons of  $Ho^{3+}$  ions, whose L-S coupling results in a set of 17 eigen-states then split by the CEF as mentioned above. The most important net effect is a doublet ground state with a larger spin projection along the quantization axis at zero temperature than that along the external field direction in the polarized paramagnetic state. The holmium ions in LiHoF4 are predominantly Ho-165 with a nuclear spin moment of  $\frac{7}{2}$ . An outcome of the Holmium's 4f orbit being very close to the nuclei is the presence of a strong onsite hyperfine interaction ( $A \sim 3.361 \times 10^{-3}$  meV), which is roughly 30 times bigger than the exchange interaction in LiHoF<sub>4</sub> [61]. Consequently, at temperatures comparable to this energy scale ( $\leq 280mK$ ), the coupling of the electronic spin degree of freedom to that of the nuclear spin becomes so important that it affects the stability of ordered state, and ultimately facilitates an increase of critical fields[9] with the help of a comparatively bigger diagonal spin projection mentioned above[13]. This enhancement of critical field was also recorded by inelastic neutron scattering measurement in Ref. [60], the key result is taken from the literature and presented in the inset of figure 1.1(a), where the solid markers trace out an experimentally measured excitation spectrum of LiHoF4 at ~ 300 mK, whose cusp marks the corresponding critical field. The value of this critical field is apparently shifted toward higher field comparing to the calculated value (dashed line) without taking into consideration the hyperfine interaction.

On the other hand, a related experimental observation in regard to the excitation spectrum of LiHoF $_4$  was also recorded in the same experiment, which is the halt of complete softening of the electronic excitation mode at the QCP[60]. The authors of the same report showed that the origin of this incomplete mode softening is again the hyperfine interaction, and it can be seen again in the inset of figure 1.1(a): the calculated electronic excitation mode softens completes at the QCP when the hyperfine interaction is excluded (dashed line), while the same mode softens only to a finite gap at the QCP and agrees with the experimental results when the hyperfine interaction is included (red solid line). Accompanied by this finite gap is a "transfer" of spectral weight, manifested as neutron absorption intensities, to electro-nuclear excitation modes at energies lower than the resolution of the instrument used here. This observation is captured in the experimental absorption data at finite momentum transfer given in figure 1.1(b), where the left and right panels show respectively, the same measurement repeated at and below the critical field. The former has an obviously bigger absorption intensity than the latter owing to the soft mode at the elastic line.

The experimental observation of incomplete softening of electronic excitation mode in

LiHoF<sub>4</sub> then in turn motivated some theoretical works on the subject. This is because it raises a controversial issue about the quantum phase transition in LiHoF<sub>4</sub> since it may imply a violation of basic thermodynamics, which prescribes for all continuous phase transitions a diverging double-time-correlation-function at the QCP that ultimately results in the closing of an energy gap, or in other words, a completely soft mode[64]. One notable example of these theoretical works is Ref. [48], where the electronic excitation mode indeed doesn't soften completely, instead, the softening was found by RPA calculations to be transferred to the lowest electro-nuclear excitation mode.

A summary of the finding from Ref. [48] is reproduced and plotted in figure 1.1(d) to be compared to the MF results in figure 1.1(c), where we also provide a pictorial illustration of the electro-nuclear spin configurations between ordered and disordered states in the inset. In both figures, the two bundles of blue curves are the electronic ground state doublet, as functions of transverse magnetic field, that each is split by the hyperfine interaction. By comparison, though much of the eigen-states remained the same, two differences stand out prominently in figure 1.1(d). The first is again the up shift of critical field marked by the cusps in the eigen-states. The second change is the modification of two single electro-nuclear spin states out of each electronic spin state manifold, with the one from the upper state softening incompletely at the critical point, shown in the main panel, and the one from the ground state manifold softens completely at the QCP as made clear in the insets of the same figure. Although these findings satisfyingly resolve the conflict of established thermodynamics theorems and experimental observations and echo both the observation and proposition of Ref. [60], to date, an experimental smoking-gun-evidence remains elusive despite some early promising success reported in Ref. [45].

Apart from the aforementioned problems, other issues such as the sudden "collapse" of the ordered state at high temperature regime (seen in fig. 1.1), to a large degree, remain a mystery despite a recent progress[19]. These fundamental research interests along with the prospective applications in quantum computing give plenty of life to  $LiHoF_4$  as a research subject. Motivated by these aspects of the topic, we carried out our work on the compound with a focus on the hyperfine interaction and its effect on the dynamical properties of  $LiHoF_4$ . Given the energy resolution required is not easily accessible by conventional techniques such as NMR, ESR, and neutron scattering, we employ techniques from the recent field of cavity magnonics at radio frequency (RF) as a spectroscopic method to study these electro-nuclear spin states and excitation modes in  $LiHoF_4$  [41, 45].

All of these theoretical and experimental findings motivate us to look into the hyperfine

interactions in LiHoF4 that promise both interesting fundamental physics and future technological applications. But due to the constrain of relevant energy scales the interaction strength puts on the energy resolution, some of the conventional experimental techniques either fall short on that aspect (e.g. NMR, EPR) or are not optimized for those energy scales (e.g. neutron scattering). However, there do exist techniques that can probe at great precision the hyperfine states such as optical absorption spectroscopy in Ref. [47]. Another technique is to use 2D radio-frequency (RF) co-planar cavity to couple directly "pump and probe" hyperfine levels with photons of appropriate energies such as in Ref. [66] and Ref. [41], the latter of which became the precursor of the present work. Despite the concept of this technique being fairly straightforward, the implementation of it is very challenging, primarily due to the fact that mode volumes of co-planar cavities are innately small, this combined with typically low quality factor for being semi-open to the free space, greatly hinders coupling to the spin ensembles strongly enough to for the "pump and probe" scheme to work. Therefore, for our purpose, we take a step forward and employ a well established spectroscopic technique that is sometimes known as the Cavity Magnon-Polariton (CMP) method, which uses high-finesse 3D cavities to excite the spin ensembles, for the current and on-going work on the investigation of hyperfine interaction and its implications in LiHoF<sub>4</sub>.

#### 1.3 Cavity magnonics

Cavity magnonics, built on the well developed principles of quantum electrodynamics (QED) and quantum optics, is an emerging field of perturbative spectroscopic method[59]. The chief idea is to hybridize magnetic excitations of spin ensembles inside cavities with the photon/electromagnetic (EM) fields of the cavities in quantum/classical limit with the aim of studying the underlying spin systems. Cavity resonators employed for magnon-polariton coupling can take on different forms, such as co-planar cavity resonators[66], 3D cavity[1], optical ring cavity[16] and so on. Regardless of the detailed format of the cavity, the common feature is that, due to the physical and electromagnetic properties of an EM cavity and the resulting boundary conditions, standing waves with well defined resonating frequencies can sustain on these structures. By merit of such a frequency selection, one gains control over the EM environment of the spin system inside the cavity. Energies can then be injected and stored using these standing EM waves that would last for a long duration, or many periods, before they decay through incoherent dissipation or cavity leakage.

Conventionally, the magnetic materials being studied using cavity magnonics are mostly paramagnetic salt such as DPPH[1, 10]. In principle, the higher the photon density and the more spins, the stronger the coupling, which is desirable because it maximizes the energy transfer for faster information extraction or efficient spin manipulation. However, since in practice the photon density cannot increase unbounded, and the number of participating spins are limited by sample volume and spin density, there is a limit to the coupling strength for light-matter interaction one can achieve this way. Consequently, some of the focus in the field lately has been on the realization of strong and ultra-strong coupling between cavity fields and magnetic materials via other means. Some recent works have turned attention to ferromagnetic materials with large effective spins such as yttrium iron garnet (YIG)[50, 54] and achieved strong coupling in the sub-mm regime. Some efforts on achieving strong coupling with 2D superconducting cavity and diamond NV-centers were also reported [66], demonstrating the possibility of interacting coherently with nuclear spin states. Meanwhile, so called ultra-strong coupling has also been demonstrated in both superconducting artificial atoms and doped YIG samples[55, 37].

Other research focuses on the light-matter interaction inside an EM cavity have also progressed. Notable examples include cavity mediated spin current manipulation[5], active control of magnon-polariton coupling strength[33, 11], dissipative magnon-polariton coupling[75, 78, 57], and magnon dark mode[8, 80]. Due to their limited relevance to the present work, we will leave out the details.

Over the last decade, the field of cavity magnonics has experienced rapid development with some of the sophisticated experimental and analytical techniques becoming mature and standardized. The plethora of existing literature provide a wealth of information on how to adapt it for different purposes. Driven by these appealing prospects, the accessibility to a wide frequency range, and the applicability for general purposes, we employed some of the aforementioned techniques of cavity magnonics to investigate the electro-nuclear spin states in LiHoF<sub>4</sub>, details of which will gradually unfold in the following chapters.

## 2 Theoretical methods

In this chapter, for completeness, we will review some of the central theoretical techniques or concepts employed in the project for the investigation of electro-nuclear spin states in  ${\rm LiHoF_4}$ . Many of these techniques were originally introduced a long time ago and have been undergoing development for decades. Plenty of literature existing prior to the present text gave detailed and thorough treatment of these subjects, we therefore only provide a concise, but self-contained, outline of them along with examples by applying them to simple toy models.

#### 2.1 Mean Field Approximation of Spin Hamiltonian

The mean field theory (MFT) has found a wide range of applications in multiple fields of condensed matter physics owing to its simplicity yet powerful capability of capturing equilibrium physics in bulk states, where fluctuations of internal degrees of freedom is of less importance. In essence, as its name implies, the MFT assumes uniformity over an entire system under investigation and hence reduces many-body problems to single-body problems. Because of the strong connection between LiHoF<sub>4</sub> and the Ising model, we thus choose to illustrate the main idea of MFT by applying it to the ideal transverse Ising model. We start with the definition of the model with the following hamiltonian:

$$\hat{\mathcal{H}} = \sum_{\langle i,j \rangle} \mathcal{J}_{ij} \hat{S}_i^z \hat{S}_j^z - \sum_i B^x \hat{S}_i^x \tag{2.1}$$

where  $\mathcal{J}_{ij}$  characterizes interacting strength between two spins. In general, for interaction ranges longer than the nearest neighbors,  $\mathcal{J}_{ij}$  becomes a function dependent on inter-spin distance.  $\hat{S}_i^{\alpha}$  stands for the  $\hat{\alpha}$  ( $\alpha = x, y, z$ ) Cartesian component of an effective spin on

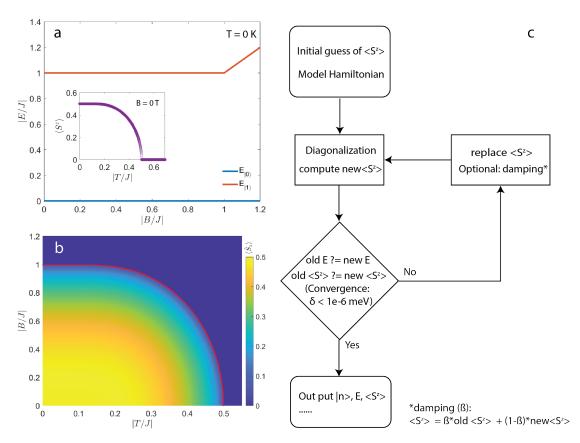


Figure 2.1: (a) MF eigen-states of the transverse Ising model at zero-temperature as a functions of magnetic field. Inset: expectation value of the spin projection along the quantization axis as a function of temperature at zero field. (b) Color plot: magnetic phase diagram from the MF solutions to the Ideal Ising model defined by Eq. 2.2, axes are in units of spin-spin interaction strength (J). Red curve: phase boundary defined by the vanishing point of  $\langle S^z \rangle$ . (c) Flow chart illustration of general steps for finding numerical solutions to a mean field spin hamiltonian.

lattice site  $i.\ B^x$  is the transverse magnetic field perpendicular to the quantization axis. In the present example, we have arbitrarily chosen it to be along  $\hat{x}$  and homogeneous across the entire spin system. The first term is clearly a many-body term as it sums over all the spin pairs on the lattice; and the second term, which doesn't commute with the first term and hence nor with the total hamiltonian, is what induces quantum fluctuation and gives the system its quantum nature. Consider the simple case of a single domain structure, it is then reasonable to assume that there exists a system-wide mean value for the expectation value of spins, denoted by  $\langle\langle \hat{S}^z \rangle\rangle$ . Here the double angle bracket implies it's an average on two levels, the first is a real space average over all sites of the system, and the second is a quantum mechanical expectation value. Subsequently the spin on each site can be

rewritten in terms of fluctuations around this mean value:  $\hat{\mu}_i^z = \langle \langle \hat{\mu} \rangle \rangle + \delta \hat{\mu}_i^z$  and the total hamiltonian can be rewritten as:

$$\hat{\mathcal{H}} = \sum_{i} \left\{ \sum_{j < i} \mathcal{J}_{ij} \left[ \langle \langle \hat{S}^{z} \rangle \rangle + \delta \hat{S}_{i}^{z} \right] \left[ \langle \langle \hat{S}^{z} \rangle \rangle + \delta \hat{S}_{j}^{z} \right] - B^{x} \hat{S}_{i}^{x} \right\}$$

$$= \sum_{i} \left\{ \sum_{j < i} \mathcal{J}_{ij} \left[ \langle \langle \hat{S}^{z} \rangle \rangle^{2} + \delta \hat{S}_{i}^{z} \langle \langle \hat{S}^{z} \rangle \rangle + \langle \langle \hat{S}^{z} \rangle \rangle \delta \hat{S}_{j}^{z} + \delta \hat{S}_{i}^{z} \delta \hat{S}_{j}^{z} \right] - B^{x} \hat{S}_{i}^{x} \right\}$$

$$= \sum_{i} \left\{ \sum_{j < i} \mathcal{J}_{ij} \left[ \langle \langle \hat{S}^{z} \rangle \rangle^{2} + 2 \langle \langle \hat{S}^{z} \rangle \rangle \right] \hat{S}_{i}^{z} - B^{x} \hat{S}_{i}^{x} \right\} + \sum_{j < i} \mathcal{J}_{ij} \delta \hat{S}_{i}^{z} \delta \hat{S}_{j}^{z}$$

$$\hat{\mathcal{H}}_{MF} \tag{2.2}$$

In the last step, we have also made the substitution  $\delta \hat{S}_i^z = \hat{S}_i^z - \langle \langle \hat{S}^z \rangle \rangle$  and discarded the resulting constant term, since all it does is shifting all the eigen-states uniformly with no effects on the excitation spectra and corresponding spectral weights that primarily interest us. The essence of MFT is to assume that fluctuations on different sites are random and not correlated, and therefore when integrated over the entire system the last term vanishes  $(\sum_{i < i} \delta \hat{S}_i^z \delta \hat{S}_j^z = 0)$ , leaving the dominant spin-spin interaction effect on individual spins entirely up to  $\langle\langle \hat{S}^z\rangle\rangle$ . This effectively replaces pair-wise summation over the lattice with a summation of single-site hamiltonian that each interacts with the same scalar internal field who oneself is a result of an averaged effect from the spin-spin interaction. In the new summation, all terms except for the very last one are essentially simple additives of single-site hamiltonians since the summation over j only affects the interaction strength  $\mathcal{J}_{ij}$  on an infinite lattice. The simplest case of this interaction is then the isotropic exchange interaction among nearest neighbors, where  $\mathcal{J}_{ij} = \mathcal{J}$  is merely a constant multiplied by the coordination number. In the case of dipole-dipole interaction, as is for LiHoF4 ,  $\mathcal{J}_{ij}$  is slightly more complicated as it depends on both the distance and relative bearing between spins, but it is nonetheless a trivial quantity to calculate under the MFT.

Since the mean field approximation completely ignores the spin-spin correlation, it naturally fails whenever this effect is strong, which is typically the case near critical points when the correlation function ( $\langle\langle\delta\hat{S}_i^z\delta\hat{S}_j^z\rangle\rangle\rangle$ ) diverges. One subsequently can immediately see that MF approximation is better suited for, 1. when fluctuations are small such as at low temperatures and away from critical points; and 2. long range interaction dominant systems. The reasoning for the latter assertion lies in the fact of that the more participants of the interaction, the less important is the fluctuation of an individual spin.

In some limiting cases, analytical solutions to the hamiltonian in Eq.2.2 can be found, and

hence various expectation values of the observables could be computed[64, 46]. However, in the case of LiHoF<sub>4</sub>, the dominant interaction is long range magnetic dipole interaction, which creates a rather big hurdle in finding analytical solutions. Despite the fact of that when all spins are considered equal, as they are in the MFT, the dipole-dipole interaction becomes a mere scalar field from integration, in practice we nonetheless resort to numerical methods for solutions. Therefore, we detail here the steps taken in finding such solutions: the eigen-states and functions are found by a self-consistent process kicked off with an educated guess of initial states, and the constructed hamiltonian in the basis of  $\hat{J}^z$  is diagonalized repeatedly until both the eigen-energies and the order parameter converge. An abridged flow chart of this process is given in figure 2.1(c).

Since we are primarily concerned with the magnetic properties, the natural choice for the order parameter here is magnetization, which is proportional to the expectation value of the spin moment under MF approximation. Shown in figure 2.1(a) is the MF solution obtained numerically to the eigen-states of a 1D transverse Ising model defined by Eq. 2.2, where  $\mathcal{J}_{ij} = \mathcal{J} < 0$  is finite only among nearest neighbors. We demonstrate the spontaneous symmetry breaking by plotting  $\langle S^z \rangle$  at zero field as the order parameter in the inset of the same figure. The value of  $\langle S^z \rangle$  can be seen to change continuously as a function of the temperature, betokening a continuous phase transition. The value of  $\langle S^z \rangle$  is also plotted in a color map in figure 2.1(b) now as a function of both temperature and magnetic field. A red curve is plotted on top of the color map, demonstrating a smooth and monotonic curvature over the entire variable range. It marks the magnetic phase boundary that separates the region where the order parameter is finite from those where it vanishes. Most notably, it marks the zero-field-critical-temperature at  $T_c = |\mathcal{J}|/2$  and the zero-temperature-critical-field at  $B_c = |\mathcal{J}|$ , which is consistent with the Ising phase boundary shown in blue asterisk in Fig. 1.1 from Chpt. 1.

As briefly mentioned in Chpt.1, an significant point of interest in LiHoF<sub>4</sub> is the presence of a strong hyperfine interaction and its consequences. Therefore, we also consider the case of an ideal Ising model with hyperfine interactions and add an appropriate term to the hamiltonian in Eq. 2.1:

$$\hat{\mathcal{H}} = \sum_{\langle i,j \rangle} \mathcal{J}_{ij} \hat{S}_i^z \hat{S}_j^z - \sum_i \left[ B^x \hat{S}_i^x + A \hat{S}_i \cdot \hat{I}_i \right]$$
 (2.3)

where  $\hat{I}_i$  represent the nuclear spin on lattice site i, and A is the hyperfine interaction strength. First of all, noting the matching subscripts between the electronic and nuclear

Eigen-vectors	$\alpha_{0,n}(0)$	$\alpha_{1,n}(0)$	$\alpha_{2,n}(0)$	$\alpha_{3,n}(0)$
0>	1	0	0	0
1>	0	~ -0.99	~ -0.099	0
$ 2\rangle$	0	0	0	1
3>	0	~ -0.099	~ 0.99	0

Table 2.1: Decomposition of the eigen-states to the Ising Hamiltonian with hyperfine interaction in Eq. 2.3.

spins, Eq. 2.3 takes into consideration only same-site (onsite) interactions, which is reasonable in most of cases due to the fact that: 1. nuclear moments are typically very small and the resulting dipole field decays rather fast; 2. nuclear moments are deeply buried in the electron clouds, and the strongest interaction takes place primarily between the nuclear spin moments and those from electrons that travel in orbits close to the nucleus; 3. the magnetic moments from the electron clouds partially shield the dipole field emanating from the nuclear spins. Moreover, the nuclear magnetic moment in principle also interacts with the external magnetic field, but in most of the cases it is an exceedingly weak interaction (e.g. it is more than 500 times smaller than the electronic Zeeman interaction in LiHoF $_4$  [48]), we therefore omit this interaction in the present case for simplicity. Lastly, noting the vector product between the nuclear and electronic spin moments, the hyperfine interaction can be isotropic or anisotropic, depending on tensor A. Since the hyperfine interactions is isotropic in LiHoF $_4$ , we will therefore add an isotropic hyperfine interaction to our simple two-level Ising model and continue our calculation with it.

The coupling of the two degrees of freedom then expand the dimension of the Hilbert space from 2 to 4, and the product state of the electronic and nuclear spins form a new set of orthogonal basis. Since they are both Ising spins, we can label these states using the shorthand notation  $|SI\rangle = |S\rangle \otimes |I\rangle$ :  $|\uparrow\uparrow\rangle$ ,  $|\uparrow\downarrow\rangle$ ,  $|\downarrow\downarrow\uparrow\rangle$ , where we use the bigger arrow for the electronic spin and the smaller one for the nuclear spin.

The rest of the procedure is the same as described before: the hamiltonian in Eq. 2.3 that is now expressed in the aforementioned new basis is first diagonalized numerically under the MF approximation, to find the eigen-states  $(E_n)$  and eigen-functions  $(|n\rangle)$ . Then the found solutions are used to compute for both expectation values of  $\hat{S}$  and  $\hat{I}$ . To carry out the calculation, we set |S| = |I| = 1/2 and  $A_x = A_y = A_z = -0.2|\mathcal{J}|$ . The eigen-states found

can be expressed in the electro-nuclear spin basis as  $|n\rangle(B^x) = \alpha_{0,n}(B^x)| \uparrow \uparrow \rangle + \alpha_{1,n}(B^x)| \uparrow \downarrow \rangle + \alpha_{2,n}(B^x)| \downarrow \downarrow \uparrow \rangle + \alpha_{3,n}(B^x)| \downarrow \downarrow \downarrow \rangle$ , where n=0,1,2,3 and the first subscript of  $\alpha$  keeps track of its corresponding basis vector. These coefficients (weights) of the expansion at zero field is summarized in table 2.1. The results of  $E_n$ ,  $\langle \hat{S} \rangle$ , and  $\langle \hat{I} \rangle$  are presented in figure 2.2(a-c) in the same order.

The important thing to note from these eigen-states is that, the hyperfine interaction entangles the spin states  $|\uparrow\downarrow\rangle$  and  $|\downarrow\uparrow\rangle$  and allows for flip-flop transitions even in absence of an external magnetic field. The subsequent application of the transverse field then further introduces tunneling among other electro-nuclear spin states.

Reading from figure 2.2(a-c), the eigen-states for the Ising model with hyperfine interaction are seen to resemble those in figure 2.1(a), except for that the each of the original electronic spin states is now split into a pair of electro-nuclear spin states. Each pair are parallel between themselves as functions of external magnetic field throughout the variable range.

As to the expectation values of the electronic and nuclear spins, it is clear from figure 2.2(b, c) that the presence of the nuclear degree of freedom, or spin bath, does not change the continuous nature of the phase transition, which is manifested in the continuous change of  $\langle \hat{S}^z \rangle$ . On top of that, the three Cartesian components of both electronic and nuclear spins are identical to each other as functions of magnetic field, "moving synchronously" throughout the variable range. Thus the spin projections along the quantization axis of both  $\hat{S}^z$  and  $\hat{I}^z$  vanish together, and at exactly the same location  $(B_c = |\mathcal{J}|)$  as before when hyperfine interaction was not considered.

These result seem to suggest that the hyperfine interaction does not affect the critical behavior of the Ising system. However, the situation becomes very different if one introduces an anisotropy to the hyperfine interaction[48]. To this end, we set  $A_x = A_y = -0.2|\mathcal{J}|$  and  $A_z = -|\mathcal{J}|$ , then carry out the same MF calculation and present the results in figure 2.2(d-f). According to the results, now as the hyperfine anisotropy makes the interaction between  $\hat{S}^z$  and  $\hat{I}^z$  5 times stronger than those between spin projections along the other two axes. The highest eigen-state is, on the one hand, pushed further up in energy at zero field, and, on the other hand, the eigen-states no longer evolve synchronously along the field axis but develop an uneven spacing among themselves at different external fields.

Furthermore, the anisotropic hyperfine interaction now creates a strong preference for the nuclear spin to align along the quantization axis, and hence introduces an indirect competition between the transverse (electronic) Zeeman interaction and the hyperfine

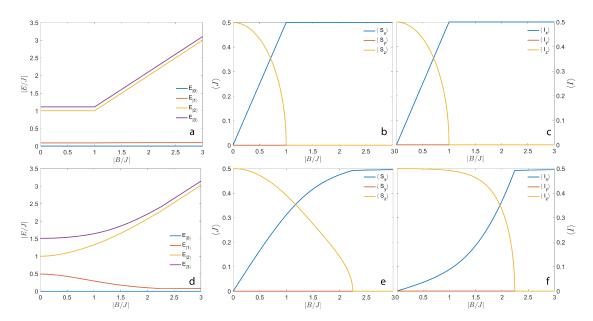


Figure 2.2: Eigen-states of Ising models with isotropic (a) and anisotropic (d) hyperfine interactions. (b, c) Expectation values of electronic and nuclear spins as functions of magnetic field for Ising model with isotropic hyperfine interaction ( $A_x = A_y = A_z = 0.2 \mathcal{J}$  and  $\mathcal{J}$  is exchange interaction strength). (e, f) The same as (b, c) but with anisotropic hyperfine interaction ( $A_x = A_y = 0.2 \mathcal{J}$ ,  $A_z = 1.0 \mathcal{J}$ ).

interaction as  $\langle \hat{S}^z \rangle$  diminishes while  $\langle \hat{S}^x \rangle$  grows. The foremost consequence of this competition is an enhanced critical field from the original value of  $B_c = |\mathcal{J}|$  to  $B_c = 2.2|\mathcal{J}|$ , which is again marked by the vanishing point of  $\langle \hat{S}^z \rangle$  along the field axis. Though in this case, the spin projections along the quantization axis for electronic and nuclear spins have overall different line shapes, they nonetheless vanish at the same field as seen in figure 2.2(e, f).

Thus we have shown that the addition of hyperfine interaction doesn't automatically warrant an increase of critical field for the simple two-level Ising model, but require an Ising anisotropy in the hyperfine interaction. This appears to be inconsistent with observations made in the case of  $LiHoF_4$ , where the hyperfine interaction is isotropic and causes an increase of critical field. If  $LiHoF_4$  is indeed described by the Ising model in a nuclear spin bath, there is then no obvious source from which an anisotropic hyperfine interaction would arise. Therefore, it appears that the simple two-level Ising model is insufficient to encompass all aspects of  $LiHoF_4$ , and we shall return to this point in Chpt. 3 to develop a more adequate toy model.

#### 2.2 Dynamical Susceptibility

As the name implies, dynamical susceptibility, as opposed to static susceptibility, characterizes a system's response to time-dependent excitations. It encompasses a vast zoo of excitations in magnetic, electronic, mechanical systems *etc*. There exists many well written books on the subject matter[39, 56, 20, 77, 46]. We will hence not spend pages to reinvent the wheel, but rather to just give an outline of relevant results in the specific context of an localized spin system under the excitation of a time-dependent external magnetic field. We will then make use of the model built in the previous section to demonstrate the application of these results.

#### 2.2.1 Linear Response Theory

We start by considering a quantum mechanical system under a longitudinal time-dependent magnetic field. For simplicity, we assume the field is homogeneous across the entire system. Thus the system can be described using the following hamiltonian:

$$\hat{\mathcal{H}} = \hat{\mathcal{H}}_0 - B^z(t) \sum_i \hat{\mu}_i^z; \tag{2.4}$$

where  $B^z(t)$  is the time-dependent longitudinal field. In the present pursuit, we would like to know how the system's response to this external excitation manifested in the observable  $\langle \hat{S}^z \rangle$ . For this purpose, we may define a response function  $(\chi_{zz}(t))$  that relates the expectation value of  $\hat{S}^z$  some point later in time (t) after the external field is turned on at  $t_0$  to  $B^z(t)$  itself as:

$$\langle \hat{S}^z(t) \rangle = \langle \hat{S}^z(t_0) \rangle + \frac{1}{g_L \mu_B} \int_{t_0}^t \chi_{zz}(t - t') B^z(t') dt'$$
 (2.5)

then, by assuming  $B^z(t)$  is adiabatically turned on at  $t_0$  and taking  $t_0$  to  $-\infty$ , a Fourier transformation to the frequency space yield a simple expression:  $g_L \mu_B \langle \hat{S}^z(\omega) \rangle = \chi_{zz}(\omega) | B^z(\omega) |$ , where  $\chi_{zz}(\omega)$  is the response function we sought after in the frequency space, and  $B^z(\omega)$  is the Fourier transform of the time-dependent field. To acquire the explicit expression of  $\chi_{zz}(\omega)$ , we consider the time evolution of density operator  $\hat{\rho}$ , which is governed by equation

of motion:

$$\frac{d}{dt}\hat{\rho}(t) = \frac{i}{\hbar}[\hat{\mathcal{H}}, \hat{\rho}]$$

$$= \frac{i}{\hbar}[\hat{\mathcal{H}}, \hat{\rho}_0 + \hat{\rho}(t)]$$

$$= \frac{i}{\hbar}\{[\hat{\mathcal{H}}, \hat{\rho}_0] + [\hat{\mathcal{H}}, \hat{\rho}(t)]\}$$
(2.6)

in the second step, we have separated the density operator into time-independent and time-dependent parts, and the linear response theory roots in discarding the second term, which is higher order due to  $\hat{\mathcal{H}}$  is already linearly proportional to a time-dependent function  $B^z(t')$ . Moreover, due to the fact that  $[\hat{\mathcal{H}}_0, \hat{\rho}_0] = 0$ , we thus have:

$$\frac{d}{dt}\hat{\rho}(t) = \frac{i}{\hbar} [\hat{\mathcal{H}}(t), \hat{\rho}_0] 
= \frac{i}{\hbar} [\sum_i \hat{\mu}_i^z, \hat{\rho}_0] B^z(t)$$
(2.7)

and this leads to

$$\hat{\rho}(t) = \hat{\rho}_0 + \frac{i}{\hbar} \int_{t_0}^t \left[ \sum_i \hat{\mu}_i^z, \hat{\rho}_0 \right] B^z(t') dt'$$
 (2.8)

since for any operator  $\hat{O}$ ,  $\langle \hat{O}(t) \rangle = Tr\{\hat{\rho}(t)\hat{O}\}$ , Eq. 2.5 implies:

$$\langle \hat{S}^{z}(t) \rangle = \langle \hat{S}^{z}(t_{0}) \rangle + \frac{i}{\hbar} Tr \{ \int_{t_{0}}^{t} [\sum_{i} \hat{\mu}_{i}^{z}, \hat{\rho}_{0}] \hat{S}^{z} B^{z}(t') dt' \}$$

$$= \langle \hat{S}^{z}(t_{0}) \rangle + \frac{i}{\hbar} \int_{t_{0}}^{t} Tr \{ \hat{\rho}_{0} [\hat{S}^{z}, \sum_{i} \hat{\mu}_{i}^{z}] \} B^{z}(t') dt'$$

$$= \langle \hat{S}^{z}(t_{0}) \rangle + \frac{1}{g_{L} \mu_{B}} \int_{t_{0}}^{t} \chi_{zz}(t - t') B^{z}(t') dt'$$

$$(2.9)$$

we took advantage of permutation rules of trace in the second step, and it immediately follows that:  $\chi_{zz}(t-t') = \frac{i}{\hbar} \langle [\hat{\mu}(t), \sum_i \hat{\mu}_i^z(t')] \rangle$ , where t > t'. Adopting Heisenberg picture, in which the eigen-states are time-independent whereas the operators are time-dependent and given by  $\hat{O}(t) = e^{\frac{i}{\hbar}\hat{\mathcal{M}}t}\hat{O}e^{-\frac{i}{\hbar}\hat{\mathcal{M}}t}$ , then setting t' = 0 and the response function can be

rewritten as:

$$\chi_{zz}(t) = \frac{i}{\hbar} \langle [\hat{\mu}(t), \sum_{i} \hat{\mu}_{i}^{z}] \rangle 
= \frac{i}{\hbar} Tr \left\{ e^{-\beta \hat{\mathcal{H}}} \left[ e^{\frac{i}{\hbar} \hat{\mathcal{H}} t} \hat{\mu} e^{-\frac{i}{\hbar} \hat{\mathcal{H}} t}, \sum_{i} \hat{\mu}_{i}^{z} \right] \right\} 
= \frac{i}{\hbar} \sum_{m,n} \frac{1}{Z} Tr \left\{ e^{-\beta \hat{\mathcal{H}}} |m\rangle \langle m| \left[ e^{\frac{i}{\hbar} \hat{\mathcal{H}} t} \hat{\mu} e^{-\frac{i}{\hbar} \hat{\mathcal{H}} t}, \sum_{i} \hat{\mu}_{i}^{z} \right] |n\rangle \langle n| \right\}$$
(2.10)

where  $|m\rangle$  and  $|n\rangle$  are eigen-states of  $\hat{\mathcal{H}}$ ,  $\beta=1/k_BT$ , and Z is the partition function given by  $Z=\sum_n e^{-\beta E_n}$ . Take into consideration of that spin operators on different lattice site commute with each other, denote the occupation number of state n as  $P_n=\frac{1}{Z}e^{-\beta E_n}$ , and by using standard contour integral technique, we eventually arrive at the spectral representation of the response function in frequency space as:

$$\chi_{zz}(\omega) = \sum_{m,n} \frac{\langle m | \hat{\mu}^z | n \rangle \langle n | \hat{\mu}^z | m \rangle}{E_n - E_m - \hbar \omega + i \hbar \gamma} (P_m - P_n)$$
 (2.11)

since we are specifically investigating how the magnetization of a system changes under the influence of a time-dependent magnetic field, this response function is in fact the dynamic susceptibility. Given the exact eigen-states of the many-body hamiltonian, the result of Eq. 2.11 is also exact, with the caveat that it is to the first order of time-dependence. Hence, the formulation should be regarded as perturbative, and only valid when the driving field is small. In practice, one rarely knows the exact wave function to a many-body system, but Eq. 2.11 can still be used with MF eigen-states to yield mean-field-dynamic-susceptibilities. To differentiate it from the exact result, thus calculated susceptibility is denoted by  $\chi_{zz}^{MF}$ .

Again as an example, we compute this susceptibility for the Ising model defined by Eq. 2.2 in the previous section by employing the MF eigen-function to obtain the off-diagonal elements  $(\langle m|\hat{\mu}^z|n\rangle,\ m\neq m)$ , and MF eigen-energies for  $E_n$  as well as calculating the partition function (Z) and population factors ( $P_n$ ). A side note here is that, though in general  $|\vec{\mu}_i^z| = g_L \mu_B |\vec{S}_i^z|$ , where  $g_L$  and  $\mu_B$  are Landé factor and Bohr magneton respectively. Since these pre-factors only affect the amplitude, which is of less importance here, we set  $g_L \mu_B = 1$  in the following calculations for simplicity.

In figure 2.3(a), we show the imaginary part of the result in the color map where the color scale represents the amplitude, from which one can see an excitation mode between the ground state and the excited state evolves as a function of magnetic field with a finite gap permanently open, identical to that in figure 2.1. The spectral weight of this

excitation mode also vary along the field axis, with it being much smaller at zero and low fields. The mechanism behind this observation is rather straightforward: at zero field, the total hamiltonian  $(\hat{\mathcal{H}})$  and the electronic spin projector along the quantization axis  $(\hat{S}^z)$  commute with each other, hence there are no off-diagonal elements for  $\hat{S}^z$  when using the eigen-states of the hamiltonian as the basis. But as the external magnetic field increases, the transverse Zeeman term grows stronger, and so does the degree to which  $\hat{\mathcal{H}}$  and  $\hat{S}^z$  don't commute. Therefore at higher fields, the off-diagonal elements  $(\langle m|\hat{S}^z|n\rangle,\ m\neq n)$  becomes bigger, and according to Eq. 2.11, it contributes to a higher amplitude of the longitudinal susceptibility. Physically, this can be thought of as a stronger longitudinal dynamic response facilitated by stronger tunneling between eigen-states that were induced by the transverse Zeeman interaction.

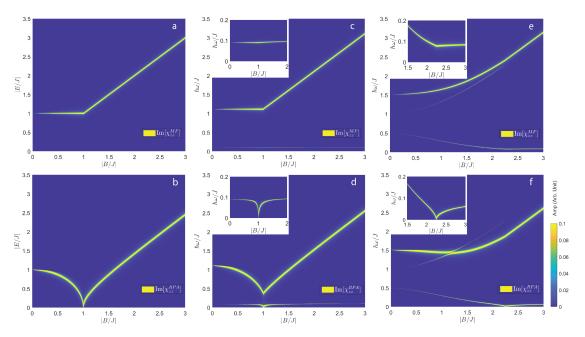


Figure 2.3: The imaginary part of MF (a) and MF-RPA (b) susceptibilities along z-axis  $(\chi_{zz})$  of the transverse Ising model with a nearest neighbor ferromagnetic interaction  $(\mathcal{J}_{ij} = \mathcal{J} < 0)$ . (c, d): The same as (a, b) but with isotropic hyperfine interaction  $(A_x = A_y = A_z = 0.2\mathcal{J})$ . (e, f): The same as (a, b) but with anisotropic hyperfine interaction  $(A_x = A_y = 0.2\mathcal{J}, A_z = \mathcal{J})$ .

The same calculation for susceptibilities was also carried out for the cases with hyperfine interactions. The imaginary parts of the result are presented in figure 2.3(b, c) for isotropic and anisotropic cases respectively. Similar to the case in absence of the hyperfine interaction, both the excitation modes in the susceptibility data follow the predictions of MF eigen-states and corresponding excitation spectra, and the amplitudes of modes increase

with growing magnetic fields. However, in the case of isotropic hyperfine interaction, the excitation mode  $|0\rangle \rightarrow |2\rangle$  is completely missing from the spectra, while being finite within some field range for the case of anisotropic hyperfine interaction.

For a better view, we plot in figure 2.4(a) the square root of the numerator of Eq. 2.11 as functions of magnetic field at zero temperature, and with different degrees of anisotropy of the hyperfine interaction. The results indeed reveal that, the specific excitation mode between the ground state the second excited state vanishes for the isotropic case. At the same time, it remains finite up until the critical field for all other cases as long as the hyperfine interaction is anisotropy. Furthermore, the peak amplitude of this off-diagonal matrix element is proportional to  $|A_z/A_{\perp}|$ , where  $|A_{\perp}| = |A_x| = |A_y|$ .

To understand this, we first realize that this missing excitation mode corresponds to, at zero field, the excitation from the ground state of having the electronic and nuclear spins being parallel to each other and the external field  $(|\uparrow\uparrow\rangle)$ , to the state of having both spins parallel to each other but anit-parallel to the external magnetic field  $(|\downarrow\downarrow\rangle)$ . Thus, for both cases of hyperfine interaction, this excitation mode vanishes at zero field:  $\langle 2|\hat{S}^z|0\rangle \stackrel{B=0}{=} \langle \downarrow\downarrow |\hat{S}^z|\uparrow\uparrow\rangle = 0$ .

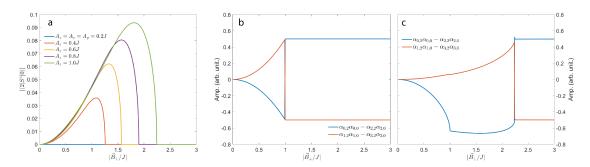


Figure 2.4: (a) Amplitudes of the off diagonal matrix element  $(\langle 2|\hat{S}^z|0\rangle)$  as functions of transverse magnetic field with different anisotropies of the hyperfine interaction. (b, c) The two contributing parts to (a) as functions of transverse magnetic field for the case of isotropic (b) and anisotropic (c) hyperfine interactions.

Secondly, as mentioned before, the eigen-function to the total hamiltonian can be expressed in the electro-nuclear spin product states:  $|n\rangle = \alpha_{0,n}| \uparrow \uparrow \rangle + \alpha_{1,n}| \uparrow \downarrow \rangle + \alpha_{2,n}| \downarrow \downarrow \uparrow \rangle + \alpha_{3,n}| \downarrow \downarrow \downarrow \rangle$ , where n=0,1,2,3 and we have used the shorthand notation  $\alpha_{m,n}=\alpha_{m,n}(B^x)$ . Therefore,

the amplitude of this excitation mode is:

$$\begin{split} \langle 2|\hat{S}^z|0\rangle &= \alpha_{0,2}\alpha_{0,0}s_0^z\langle \uparrow \uparrow \mid \uparrow \uparrow \rangle + \alpha_{1,2}\alpha_{1,0}s_1^z\langle \uparrow \downarrow \mid \uparrow \downarrow \rangle + \alpha_{2,2}\alpha_{2,0}s_2^z\langle \downarrow \downarrow \mid \downarrow \downarrow \rangle + \alpha_{3,2}\alpha_{3,0}s_3^z\langle \downarrow \uparrow \mid \downarrow \downarrow \uparrow \rangle \\ &= \frac{1}{2}[\alpha_{0,2}\alpha_{0,0} + \alpha_{1,2}\alpha_{1,0} - \alpha_{2,2}\alpha_{2,0} - \alpha_{3,2}\alpha_{3,0}] \end{split} \tag{2.12}$$

where we have used the fact that  $\hat{S}^z|\uparrow X\rangle = (+1/2)|\uparrow X\rangle$  and  $\hat{S}^z|\Downarrow X\rangle = (-1/2)|\Downarrow X\rangle$ , and X represent any nuclear spin state. Thus the amplitude of response function depends on  $(\alpha_{0,2}\alpha_{0,0}-\alpha_{2,2}\alpha_{2,0})+(\alpha_{1,2}\alpha_{1,0}-\alpha_{3,2}\alpha_{3,0})$ . In figure 2.4(b,c), we plot the two parts of this expression grouped in different brackets as functions of magnetic field for both isotropic and anisotropic hyperfine interactions. We see that, in the isotropic case, the two parts are identical but carry opposite signs and hence cancel out identically. Whereas in the anisotropic case, only at zero field and above the critical field, the two parts cancel out, giving rise to non-vanishing amplitude of the response function in between the two field locations.

#### 2.2.2 Random Phase Approximation

As demonstrated before, MF solutions ignore completely fluctuations and correlations. An easy step forward to amend this problem is the so called random phase approximation (RPA), in which effects from uncorrelated fluctuations of spins are included. We will primarily follow Ref. [39] to show its application to our problem, and eventually arrive at a susceptibility that, to a degree, takes into account spin-spin correlation effects. To begin, we again introduce a vanishing fictitious time-dependent longitudinal field  $(B_i^z(t-t_0))$  that turns on adiabatically at some point  $(t_0)$  in time. The subscript i emphasize the locality of the field but it should be noted that this field can be uniform over the entire system as well. Then, following the previous definition of response function, the susceptibility may be defined in the frequency space by  $\langle \hat{\mu}_i^z(\omega) = \sum_j \chi_{zz}(ij,\omega)\vec{B}_j(\omega)$ , where  $\vec{B}_j(\omega)$ , where the summation is over all the interacting neighbors of the spin on site i. Next we continue with the Hamiltonian defined in Eq. 2.2, and express it in the Heisenberg picture:

$$\hat{\mathcal{H}} = \hat{\mathcal{H}}_{MF} - \sum_{i < j} \delta \hat{\mu}_{i}^{z} \delta \hat{\mu}_{j}^{z}$$

$$= \hat{\mathcal{H}}_{MF}(t) - \sum_{i} \left[ \hat{\mu}_{i}^{z}(t) - \langle \hat{\mu}^{z}(t_{0}) \rangle \right] \left[ \sum_{j \neq i} J_{ij} \left[ \hat{\mu}_{j}^{z}(t) - \langle \hat{\mu}^{z}(t_{0}) \rangle \right] + B_{i}^{z}(t - t_{0}) \right]$$

$$(2.13)$$

the RPA comes in the form of treating the simultaneous fluctuation of spins in the system as completely "random" and uncorrelated, such that  $\sum_j (\hat{\mu}_j^z(t) - \langle \hat{\mu}^z(t) \rangle) \sim 0$ , or equivalently  $\hat{\mu}_j^z(t) \sim \langle \hat{\mu}^z(t) \rangle$ , therefore the terms in the bracket in Eq. 2.13 become a scalar field  $(B_i'(t-t_0))$ . Assuming the fictitious field is homogeneous across the entire system, after Fourier transform, we have a simple relation for the expectation value of single-site spin projection:

$$\langle \hat{\mu}_{i}^{z}(\omega) \rangle = \chi_{zz}(ii,\omega)B_{i}'(\omega)$$
 (2.14)

where  $B_i'(\omega) = \sum_{j \neq i} \mathscr{J}_{ij} \hat{\mu}_j^z(\omega) + B_i^z(\omega)$  is the Fourier transform of the scalar field as a result of RPA. Comparing the above expression to our definition of two-site susceptibility, we arrive at a RPA corrected MF magnetic susceptibility upon another Fourier transform to the reciprocal space:

$$\chi_{zz}^{\text{RPA}}(\vec{k},\omega) = \frac{\chi_{zz}^{\text{MF}}(\omega)}{1 - \chi_{zz}^{\text{MF}}(\omega) \mathcal{J}(\vec{k})}$$
(2.15)

In contrast to the original mean field susceptibility, the RPA susceptibility now has a momentum dependence ( $\vec{k}$ -dependence) owing to accounting for spin-spin correlations. However, as we have seen in the steps leading to this expression, it is still only valid when the fluctuations are either small or uncorrelated so that a summation over the relevant sites results in a net zero contribution to the total hamiltonian. Therefore, despite being an improvement, RPA susceptibility is still a zeroth order result just like the MF result. Further improvement will necessarily require the theory to account for the self-energy, which usually is an infinite expansion series that becomes particularly intractable for systems with long range interactions. Due to both limited capacity and focus, we will leave such improvement out of the present text.

It is worth noting that Eq. 2.15 can be generalized to tensor calculations, more specifically it reads [39]:

$$\bar{\bar{\chi}}^{RPA}(\vec{k},\omega) = [\bar{\bar{I}} - \bar{\bar{\chi}}^{MF}(\omega)\bar{\bar{\mathcal{J}}}(\vec{k})]^{-1}\bar{\bar{\chi}}^{MF}(\omega)$$
 (2.16)

where  $\bar{I}$  is the identity matrix, and both  $\bar{\mathcal{J}}(\vec{k})$  and  $\bar{\chi}^{MF}(\omega)$  are  $3\times 3$  matrices, which naturally result in  $\bar{\chi}^{RPA}(\vec{k},\omega)$  being a matrix of the same rank. We have used the double-bar over the operator to indicate the tensorial nature of them. In comparison to Eq. 2.15, extra care must be taken with the order of multiplication since in general tensor product

is not commutative. In the case of

$$\bar{\bar{\mathcal{J}}}(\vec{k}) = \begin{pmatrix} 0 & 0 & 0 \\ 0 & 0 & 0 \\ 0 & 0 & \mathcal{J}_z(\vec{k}) \end{pmatrix} \quad \bar{\bar{\chi}}^{MF}(\omega) = \begin{pmatrix} \chi_{xx}^{MF}(\omega) & 0 & 0 \\ 0 & \chi_{yy}^{MF}(\omega) & 0 \\ 0 & 0 & \chi_{zz}^{MF}(\omega) \end{pmatrix}$$
(2.17)

Eq. 2.16 reduces to Eq. 2.15.

Next, in keeping up with the same format of previous sections, we now give examples of RPA calculations using the Ising model with and without hyperfine interactions as defined in Eq. 2.2 and Eq. 2.3 respectively. For the calculation, we use Eq. 2.15, and the starting points are the MF susceptibilities ( $\chi_{zz}^{RPA}$ ) presented in figure 2.3(a-c), the corresponding results are given in the same column of the same figure (fig. 2.3(d-f)). The most striking feature of RPA susceptibility compared to the MF susceptibility is the so called "soft mode", in other words, an excitation mode that goes to zero energy/frequency. For the present case, the RPA susceptibility predicts in all three examples that an energy gap closes at the critical points, which is consistent with established knowledge of continuous phase transitions. The softening of mode is the most visible in figure 2.3(d) for the Ising model without hyperfine interaction, in which case there exists a sole excitation mode between the  $|\uparrow\rangle$  and  $|\downarrow\rangle$  states for the single-ion hamiltonian as seen in figure 2.3(a). As described above, by taking into consideration to a degree the spin-spin correlation, RPA can predict collective modes of an interacting spin ensemble, and hence goes beyond the simple single-ion picture without inclusions of higher order effects. Thus despite such zero-energy excitation being forbidden by the eigen-states of single-ion hamiltonian, it is allowed to exist as a collective excitation.

One important feature to note is that the softening of the excitation mode that occurs to the electronic spin states in figure 2.3(d) is halted in figure 2.3(e), such incomplete softening of the electronic excitation is strongly reminiscent of the experimental observation made on LiHoF<sub>4</sub>, shown in the inset of figure 1.1(a) from Chpt. 1. Here for the Ising mode with isotropic hyperfine interaction, we see the softening is "transferred" to the first excited electro-nuclear spin state. An expanded view is provided in the inset of figure 2.3(e), in contrast to that of figure 2.3(b). The same transfer of mode softening also took place for the Ising model with anisotropic hyperfine interaction given in figure 2.3(f). In addition, viewed in combination with figure 2.2(d) and figure 2.3(c), the direct hybridization that resulted in a typical "avoid crossing" pattern as well as the swap of spectral weights between the two upper states is also clearly visible in figure 2.3(f).

## 2.3 Scattering Parameters

Scattering parameters are frequently referred to as S-parameters, and are a concept introduced for electrical network analysis and useful characterizing radio-frequency (RF) circuits. It is conceptually similar to the S-matrix in that it describes the subject as a standalone unit whose interaction with the environment is entirely captured by two quantifiable processes per port: forward transmission, and backward reflection. These processes are visualized by considering waves traveling in the circuit to  $(\vec{a})$  and from  $(\vec{b})$  the load, which is the subject under investigation. For conciseness, we consider a one dimensional four-port system and label them numerically 1 and 2, then a simple relation between the waves:

$$\begin{pmatrix} \vec{b}_1 \\ \vec{b}_2 \end{pmatrix} = \begin{pmatrix} S_{11} & S_{12} \\ S_{21} & S_{22} \end{pmatrix} \begin{pmatrix} \vec{a}_1 \\ \vec{a}_2 \end{pmatrix}$$
 (2.18)

where the square matrix contains the four S-parameters that describe the aforementioned two processes at the two ports. It is then easy to deduce  $S_{11} = \vec{b}_1/\vec{a}_1$ ,  $S_{21} = \vec{b}_2/\vec{a}_1$ ,  $S_{12} = \vec{b}_1/\vec{a}_2$ , and  $S_{22} = \vec{b}_2/\vec{a}_2$ . Furthermore, for a reciprocal 2-port system, it is easy to show that  $S_{12} = S_{21}$ ,  $|S_{11}|^2 + |S_{21}|^2 = 1$ , and  $|S_{22}|^2 + |S_{12}|^2 = 1$ . In practice, in a microwave circuit, assuming the characteristic impedance  $Z_0$  of the transmission line is real, the traveling waves are given by [43]:

$$\vec{a}_1 = \frac{\vec{U}_1 + \vec{I}_1 Z_0}{2\sqrt{Z_0}} \tag{2.19}$$

$$\vec{b}_1 = \frac{\vec{U}_1 - \vec{I}_1 Z_0}{2\sqrt{Z_0}} \tag{2.20}$$

where  $\vec{U}_i$  and  $\vec{I}_i$  stand for the voltage and current propagating toward port i. Thus knowing the voltage and current on a microwave pathway on all the ports is enough to fully characterize the load circuit without a detailed knowledge of the internal circuit. This forms the foundation of our experimental investigation, where we treat the cavity loaded with  $\text{LiHoF}_4$  as an isolated system that only couples to the environment through a limited number of channels. Then by analyzing the S-parameters associated with these ports, we are able to extract information regarding the cavity-LiHoF4 ensemble and infer the dynamical properties of LiHoF4.

In the classical regime, a cavity resonator has the same characteristics as an RLC circuit[10, 41], whose impedance and resonant frequency are given respectively by  $Z_0 = \sqrt{L/R^2C}$  and  $\omega_0 = 1/\sqrt{L_0C_0}$ , where  $L_0$  is the inductance and  $C_0$  is the capacitance. When a sample is

placed inside the cavity that interacts with the photon field, to a large degree, it can be treated as a dielectric/magnetic filling material that interacts with either the electrical or magnetic, or both, components of the EM field. Thus the characteristic capacitor (C) and inductor (L) would change according to:

$$C_0 = \frac{Q}{|\vec{E}|d} = \epsilon_0 \frac{A}{d} \Rightarrow C = \frac{Q}{|\vec{P}|d} = \epsilon_r C_0$$
 (2.21)

$$L_0 = \Phi \frac{N}{I} = \mu_0 \frac{N^2 A}{l} \Rightarrow L = \mu_r \mu_0 \frac{N^2 A}{l} = \mu_r L_0$$
 (2.22)

therefore, at the presence of a dielectric/magnetic sample, the resonant frequency changes to  $\omega_c = \omega_c/\sqrt{\epsilon_r \mu_r}$ . Denoting the characteristic impedance of the transmission line by  $Z_t$ , then  $|S_{11}|$  can be expressed classically as[3]:

$$|S_{11}| = \frac{i\omega Z_t C}{1 - i\omega 2RC - 2\omega^2 CL}$$

$$= \frac{i\omega Z_t C_0}{\epsilon^{-1} - i\omega 2RC_0 - 2\mu_r \omega^2 C_0 L_0}$$
(2.23)

where we have assumed that there is no significant change to R due to the sample, or in other words there is no dissipation of energy due to the sample, but this is not to confuse with absorption process which is captured by the imaginary part of both  $\epsilon_r$  and  $\mu_r$ . Thus we have shown that, in the classical regime, S-parameters from a cavity resonator loaded with a dielectric/magnetic sample can be used to extract bulk permittivity and permeability of the sample. However, to study the microscopic spin structure in a sample by the same method, one needs to develop a quantum theory for the above result, which will be given below.

# 2.4 Input-Output Formalism

All experiments for the present project were carried out in an re-entrance cavity in the RF range. The decay and excitation of atoms in a controlled electromagnetic (EM) environment, such as a cavity resonator have long been subjected to investigation, notable models includes Dicke model[18], Jaynes-Cummings model[38], and the related Tavis-Cummings model[73]. One important technique for describing photon fields inside a cavity resonator quantum mechanically was later developed in the 1980s primarily due to C. W. Gardiner and M. J. Collett[23, 24], which is the so called input-output formalism that forms the core analytical tool of this thesis. Many existing literature give detailed account of the original input-output formalism[25, 52, 74], we hence bypass providing an abridged version

of its account which is somewhat redundant, but instead provide below a self-contained technical description of its application to the subject of this thesis.

We begin by considering some magnetic moments immersed in a cavity photon field, the interaction between these two ensembles form a quasi-particle named magnon-polariton. In principle, the hamiltonian of such a system can be conveniently compartmentalized in three interacting parts: 1. the cavity resonator. 2. the spin ensemble, and 3. the photon reservoir. More explicitly, this is written as:

$$\hat{\mathcal{H}} = \hat{\mathcal{H}}_{cavity} + \hat{\mathcal{H}}_{reservoir} + \hat{\mathcal{H}}_{spin} + \hat{\mathcal{H}}_{cav-Res}^{int} + \hat{\mathcal{H}}_{cav-spin}^{int} + \hat{\mathcal{H}}_{res-spin}^{int}$$
 (2.24)

where the first three terms are the aforementioned individual subsystems, and the other three terms are the pairwise interaction terms among them. In practice, the reservoir refers to the greater environment enclosing both the cavity and spin ensemble, its direct interaction with the spins  $(\hat{\mathcal{H}}_{res-spin}^{int})$  is kept minimal in order to reduce incoherent photon losses. Therefore, to the leading order, we can safely discard this term. For the purpose of present experiment, we employ a linearly polarized EM field in a re-entrance cavity, and accordingly impose quantization rules for cavities of arbitrary shape and inhomogeneous field distributions such that the magnetic component of the EM field reads  $\vec{B}(r,t) = \sum_k i \sqrt{\mu_0 \hbar \omega_k/2} (\hat{a}_k(\mathbf{r}) + \hat{a}_k^{\dagger}(\mathbf{r}))$ . Since the interaction between the cavity photon field and a localized spin ensemble is in essence the Zeeman interaction, we can express this part of Hamiltonian explicitly thus forth:

$$\hat{\mathcal{H}}_{cav-spin}^{int} = -\int_{\omega} \int_{V_s} \vec{\mu} \cdot \vec{B}(\omega, \mathbf{r}) dr d\omega$$
 (2.25)

$$= -\sum_{c} \int_{V_s} g_c[\hat{a}_c(\mathbf{r}) + \hat{a}_c^{\dagger}(\mathbf{r})] \cdot \vec{\mu} dr$$
 (2.26)

where  $\vec{\alpha}$  stands for the magnetic moment and the integration is over the sample volume  $(V_s)$ . Furthermore, we have used the subscripts "c" on the cavity photon creation and annihilation operators  $(\hat{a}_c^{(\dagger)} = \hat{a}^{(\dagger)}(\omega_c))$ , as well as the pre-factor  $g_c = g(\omega_c)$  in combination with the definition  $g(\omega_k) = i\sqrt{\mu_0\hbar\omega_k/2}$  [25], to indicate their correspondence to the discrete cavity modes. We similarly define operators  $\hat{b}(\omega)$  and  $\hat{b}^{\dagger}(\omega)$  for the reservoir photons, which are continuous functions in free space. The total Hamiltonian now reads (with the

**r**-dependence of  $\hat{a}_c$  omitted for simplicity):

$$\hat{\mathcal{H}} = \sum_{c} \hbar \omega_{c} \hat{a}_{c}^{\dagger} \hat{a}_{c} + \int_{\omega} \hbar \omega \hat{b}^{\dagger}(\omega, t) \hat{b}(\omega, t) + \hat{\mathcal{H}}_{spin}$$

$$+ \iiint_{V} \left\{ \sum_{c} \left[ \int_{\omega} K(\omega) (g_{c}^{*} \hat{a}_{c}^{\dagger} + g \hat{a}_{c}) [g^{*}(\omega) \hat{b}^{\dagger}(\omega, t) + g(\omega) \hat{b}(\omega, t)] \right] + (g_{c}^{*} \hat{a}_{c}^{\dagger} + g_{c} \hat{a}_{c}) \hat{\mu}^{\alpha} \right\} dV$$

$$(2.27)$$

 $K(\omega)$  characterizes the coupling between the cavity and reservoir fields and is dependent on the the physical details of the cavity. Without knowing the detailed form of  $\hat{\mathscr{H}}_{spin}$ , it is only assumed that there exists a complete set of eigen-states  $|n\rangle$  that diagonalize it, namely  $\hat{\mathscr{H}}_{spin}|n\rangle=E_n|n\rangle$ . In the present study, the frequency window ( $\leq 200$  MHz) within which the experiments were carried out is far smaller than the resonant frequencies themselves ( $\sim 2-5$  GHz). Therefore it is appropriate to apply rotating wave approximation (RWA) to cavity-reservoir interaction to discard  $\hat{a}^{\dagger}\hat{b}^{\dagger}$  and  $\hat{a}\hat{b}$ [67], which further simplifies the reservoir-cavity interaction part of the hamiltonian to:

$$\hat{\mathcal{R}}_{Cav-Res}^{int} = \int_{\omega} d\omega \, i [\tilde{K}(\omega) a_c^{\dagger} b(\omega, t) - \tilde{K}^*(\omega) b^{\dagger}(\omega, t) a_c]$$
 (2.28)

where we have absorbed  $|g_c^*g(\omega)|$  and  $|g^*(\omega)g_c|$  into  $\tilde{K}(\omega)$  and  $\tilde{K}^*(\omega)$ . Physically, the reservoir-cavity interaction encompasses both the driving of the cavity as well as the incoherent losses of photons from the cavity. Therefore the treatment of  $\tilde{K}^{(*)}(\omega)$  can be very complicated, but to a good approximation, we can adopt the first Markovian approximation[12, 15] to assume the coupling strength between the cavity field and environment is frequency independent with an explicit expression:  $K(\omega) = \hbar \kappa_e$  to remove it from the above integrand.

As to the interaction term between the cavity field and the spin ensemble, it plays a central role in characterizing our experimental setup. For the sake of generality, we will not resort to the usual semi-classical approximations for the description of the spin ensembles such as macro-spins [69] or Holstein-Primakoff transformation [36, 81]. A benefit of this approach that will emerge later is that, we do not need to create one species of quasi-particle for each magnon mode. Since the distribution of spins is discrete in real space we transform the real space integration into a summation over all the lattice sites. In addition, we normalize the EM field amplitude in the same fashion as in Ref. [22] for application to arbitrary

shaped cavity, the cavity-spin interaction hamiltonian subsequently reads:

$$\begin{split} \hat{\mathcal{H}}_{cav-spin}^{int} &= -\sum_{c} \sqrt{\frac{\mu_{0}\hbar\omega_{c}}{2}} (\hat{a}_{c} + \hat{a}_{c}^{\dagger}) \frac{\int_{V_{s}} \vec{\mu} \cdot \vec{B}(\mathbf{r}) dr}{\sqrt{\int_{V_{c}} |\vec{B}(\mathbf{r}')|^{2} dr'}} \\ &= -\sum_{c} \sqrt{\frac{\mu_{0}\hbar\omega_{c}}{2}} (\hat{a}_{c} + \hat{a}_{c}^{\dagger}) \int_{V_{s}} dr \left(\frac{1}{\sqrt{N_{s}}} \sum_{\mathbf{q}} \vec{\mu}_{q} e^{i\mathbf{q}\cdot\mathbf{r}}\right) \cdot \int \frac{d^{3}\mathbf{k}}{(2\pi)^{3}} \frac{\vec{B}_{\mathbf{k}} e^{i\mathbf{k}\cdot\mathbf{r}}}{\sqrt{\int_{V_{c}} |\vec{B}(\mathbf{r}')|^{2} dr'}} \\ &= -\sum_{c} \sqrt{\frac{\mu_{0}\hbar\omega_{c}}{2}} \frac{\hat{a}_{c} + \hat{a}_{c}^{\dagger}}{\sqrt{\int_{V_{c}} |\vec{B}(\mathbf{r}')|^{2} dr'}} \frac{1}{\sqrt{N_{s}}} \sum_{\mathbf{q}} \int \frac{d^{3}\mathbf{k}}{(2\pi)^{3}} \vec{\mu}_{q} \cdot \vec{B}_{\mathbf{k}} \int_{V_{s}} e^{i(\mathbf{q}+\mathbf{k})\cdot\mathbf{r}} dr \\ &= -\sum_{c} \sqrt{\frac{\mu_{0}\hbar\omega_{c}}{2}} \frac{\hat{a}_{c} + \hat{a}_{c}^{\dagger}}{\sqrt{\int_{V_{c}} |\vec{B}(\mathbf{r}')|^{2} dr'}} \frac{1}{\sqrt{N_{s}}} \sum_{\mathbf{q}} \int \frac{d^{3}\mathbf{k}}{(2\pi)^{3}} \vec{\mu}_{q} \cdot \vec{B}_{\mathbf{k}} \frac{N_{s}}{V_{s}} \delta(\mathbf{q} + \mathbf{k}) \\ &= -\sum_{c} \sqrt{\frac{\mu_{0}\hbar\omega_{c}\rho_{s}}{2}} (\hat{a}_{c} + \hat{a}_{c}^{\dagger}) \sum_{\mathbf{q}} |\vec{\mu}_{q}| \sqrt{\frac{[\int_{V_{s}} |\hat{e}^{\mu} \cdot \vec{B}(\mathbf{r})| e^{i\mathbf{k}\cdot\mathbf{r}} dr]^{2}}{V_{s} \int_{V_{c}} |\vec{B}(\mathbf{r}')|^{2} dr'}} \end{split}$$

where we have introduced Fourier transformations  $\vec{\mu} = \frac{1}{\sqrt{N_s}} \sum_{\mathbf{q}} \vec{\mu}_q e^{i\mathbf{q}\cdot\mathbf{r}}$  and  $\vec{B}(\mathbf{r}) = \int \frac{d^3\mathbf{k}}{(2\pi)^2} \vec{B}_{\mathbf{k}} \cdot e^{i\mathbf{k}\cdot\mathbf{r}}$ , and use  $N_s = V_s \rho_s$  to represent the total number of spins in the ensemble. Finally,  $\hat{e}^\mu$  is the unit vector along the spin orientation is accounted. For convenience, define  $\eta_c^2 = |\int_{V_s} \hat{e}^\mu \cdot \vec{B}(r) e^{i\mathbf{k}_c \cdot \mathbf{r}} dr|^2 / [V_s \int_{V_c} |\vec{B}(r')|^2 dr']$  as the filling factor that captures the degree to which the mode volume overlaps between the sample and cavity field, in the long wavelength and homogeneous field limit,  $\vec{B}(r)$  becomes r-independent, and hence the filling factor takes on the simple form of a volume ratio:  $\eta_c^2 = |\vec{B}^2 V_s|^2 / V_s |\vec{B}|^2 V_c = V_s / V_c$ . Now  $\hat{\mathcal{H}}_{cav-spin}^{int}$  eventually becomes:

$$\hat{\mathcal{H}}_{Cav-Spin}^{int} = \sum_{c} i \eta_c g_c \sqrt{\rho_s} \left( \hat{a}_c^{\dagger} \hat{\mu}_{k_c}^{\alpha} + \hat{a}_c \hat{\mu}_{-k_c}^{\alpha} \right)$$
 (2.30)

where  $\rho_s$  stands for the volume density of spins in the sample. Next, introduce a multilevel transition operator [25]:  $\hat{\sigma}_{mn} = |m\rangle\langle n|$ , where  $|m\rangle$  and  $|n\rangle$  are eigen-states of the spin Hamiltonian ( $\hat{\mathscr{H}}_{spin}|n\rangle = E_n|n\rangle$ ), so that we are able to write  $\hat{\mu}_q^\alpha = \sum_{m,n} \langle m|\hat{\mu}_q^\alpha|n\rangle \hat{\sigma}_{mn}$ , where the summation runs over the entire Hilbert space. Evidently ( $\hat{\mu}_q^\alpha$ )<sup>†</sup> =  $\hat{\mu}_{-q}^\alpha$ , since  $\sum_{m,n} \langle m|\hat{\mu}_q^\alpha|n\rangle \hat{\sigma}_{mn} = \sum_{m,n} \langle n|\hat{\mu}_{-q}^\alpha|m\rangle^* \hat{\sigma}_{nm}^\dagger$ .

All the data to be presented in this study were taken in the form of  $S_{11}$  parameters, thus the experimental setup can be abstracted as a single sided lossy cavity with an input field  $(\hat{a}_i^{\dagger}\hat{a}_i)$  and an output field  $(\hat{a}_o^{\dagger}\hat{a}_o)$ [74]. The Heisenberg equation of motion then gives:  $\partial_t \hat{b} = (i/\hbar)[\hat{\mathcal{H}}, \hat{b}]$  and  $\partial_t \hat{a} = (i/\hbar)[\hat{\mathcal{H}}, \hat{a}]$ , from which we arrive at a dynamical equation for

the cavity field operator:

$$\partial_t \hat{a}_c = -i\omega_c \hat{a}_c + \int \kappa_e^* \hat{b}_0(\omega) e^{-i\omega t} d\omega + \sum_c \kappa_e^2 \hat{a}_c + \eta \sum_c \sqrt{\frac{\mu_0 \omega_c \rho_s}{2\hbar}} \hat{\mu}_{k_c}^{\alpha}$$
(2.31)

by defining  $\hat{a}_i = -\int \hat{b}_0(\omega) e^{-i\omega(t)} d\omega$  (t < 0) and  $\hat{a}_o = \int \hat{b}_0(\omega) e^{-i\omega(t)} d\omega$  (t > 0)[52], we obtain a set of PDEs:

$$\partial_t \hat{a}_c = \sum_c \left( \Gamma(\omega_c) \hat{a}_c + i \sqrt{\frac{\mu_0 \omega_c \rho_s \eta}{2\hbar}} \hat{\mu}_{k_c}^{\alpha} \right) + \sqrt{\kappa_e} \hat{a}_i$$
 (2.32)

$$\partial_t \hat{a}_c = \sum_c \left( \Gamma(\omega_c) \hat{a}_c + i \sqrt{\frac{\mu_0 \omega_c \rho_s \eta}{2\hbar}} \hat{\mu}_{k_c}^{\alpha} \right) - \sqrt{\kappa_e} \hat{a}_o \tag{2.33}$$

where  $\Gamma(\omega_c) = -i\omega_c + (\kappa_i - \kappa_e)/2$ . Here we have added an additional Langevin force characterized by  $\kappa_i$  to account for the internal dissipation of the cavity field. Though this is equivalent to adding an imaginary term to the Hamiltonian and breaks its hermicity, it is necessary since it allows us to capture the impedance matching condition between the load (cavity) and drive (VNA + circuit), which in the real world is never perfect yet difficult to quantify. More detailed discussions about this term and the reasoning behind it can be found in Ref. [65, 44]. Using the same Heisenberg equation of motion on  $\hat{\mu}_k$  yields:

$$\begin{split} \partial_{t}\hat{\mu}_{k_{c}}^{\alpha} &= -\frac{i}{\hbar}[\hat{\mathcal{H}}_{spin}, \hat{\mu}_{k_{c}}^{\alpha}] - \frac{i}{\hbar}[\hat{\mathcal{H}}_{cav-spin}^{int}, \hat{\mu}_{k_{c}}^{\alpha}] \\ &= -\frac{i}{\hbar}[\hat{\mathcal{H}}_{spin}, \hat{\mu}_{k_{c}}^{\alpha}] - i\eta\sqrt{\frac{\mu_{0}\omega_{c}\rho_{s}}{2}} \sum_{\substack{m,n \\ p,q}} \langle m|\hat{\mu}_{k_{c}}^{\alpha}|n\rangle\langle p|\hat{\mu}_{k_{c}}^{\alpha}|q\rangle[\hat{\sigma}_{mn}, \hat{\sigma}_{pq}]\hat{a}_{c} \end{split} \tag{2.34}$$

Recall the definition  $\hat{\mu}_{k_c} = \sum_{m,n} \langle m | \hat{\mu}^{\alpha}_{k_c} | n \rangle \hat{\sigma}_{mn}$ , and the fact that our only constraint on  $\hat{\mathcal{H}}_{spin}$  is that it is hermitian and hence can be diagonalized unitarily, which equates to require:  $\hat{\mathcal{H}}_{spin} = \sum_q \epsilon_q \hat{\sigma}_{qq}$  [25]. We thus can write  $[\hat{\mathcal{H}}_{spin}, \hat{\mu}^{\alpha}_{k_c}] = \sum_{m,n} (\epsilon_m - \epsilon_n) \hat{\sigma}_{mn}$ . Define  $\Omega_{mn} = (\epsilon_m - \epsilon_n) / \hbar$  for convenience and Fourier transform Eq.2.34, we arrive at:

$$\hat{\mu}_{k_c}^{\alpha} = \eta \sqrt{\frac{\mu_0 \omega_c \rho_s}{2\hbar}} \sum_{\substack{m,n \\ p,q}} \frac{\langle m | \hat{\mu}_{k_c}^{\alpha} | n \rangle \langle n | \hat{\mu}_{-k_c}^{\alpha} | m \rangle [\hat{\sigma}_{mn}, \hat{\sigma}_{pq}]}{i(\omega - \Omega_{mn} + i\gamma_{mn})} \hat{a}_c$$
(2.35)

where the summation of m, n, p, and q runs over all the eigen-states of  $\hat{\mathcal{H}}_{spin}$  and therefore accounts for contributions from all possible excitations. An infinitesimal variable  $\gamma_{mn}$  is added to the denominator to avoid divergence at resonance, which is physically equivalent to spectral line width. The commutation relation in the nominator can be further expanded as  $[\hat{\sigma}_{mn}, \hat{\sigma}_{pq}] = \delta_{np}\hat{\sigma}_{mq} - \delta_{mq}\hat{\sigma}_{pn}$ [25], so that for any eigen-state of the spin system  $|\psi\rangle$ , it may be projected as  $\hat{\sigma}_{nn}|\psi\rangle = \langle n|\psi\rangle|n\rangle$ . Under the MF approximation,

the spectral weights in equilibrium are entirely governed by the Boltzmann distribution, therefore  $\langle n|\psi\rangle=e^{-\beta E_n}/Z$  and  $\hat{\sigma}_{nn}=P_n$ . By the merit of all the aforementioned definitions and manipulations, plus Eq.2.11, we are able to express the last term of Eq.2.31 as:

$$-\eta^{2} \frac{\mu_{0}\omega_{c}\rho_{s}}{2} \sum_{m,n} \frac{\langle m|\hat{\mu}_{k_{c}}^{\alpha}|n\rangle\langle n|\hat{\mu}_{-k_{c}}^{\alpha}|m\rangle}{i\hbar(\omega - \Omega_{mn}) - \hbar\gamma_{mn}} (P_{n} - P_{m})$$

$$= i|\tilde{g}(\omega_{c})|^{2} \chi_{\alpha\alpha}(k_{c}, \omega)$$
(2.36)

where we have defined  $\tilde{g}(\omega_c) = i\eta \sqrt{\mu_0 \hbar \omega_c/2} = g(\omega_c) \sqrt{\eta^2 \rho_s/\hbar}$ . Finally, Fourier transforms of Eq.2.32 and Eq.2.33 with some straightforward algebra offer us a simple expression for the  $|S_{11}|$  parameter:

$$|S_{11}| = \left| 1 + \frac{2\kappa_e}{i(\omega - \omega_c) - (\kappa_e + \kappa_i) + i|\tilde{g}(\omega_c)|^2 \gamma_{\alpha\alpha}(k_c, \omega)} \right|$$
(2.37)

which, as far as the authors are aware, has never been derived microscopically without the aid of semi-classical approximations as in the present text. In principle, Eq. 2.37 applies to all systems alike in the linear response regime. Rewriting the generalized susceptibilities in explicit real and imaginary parts  $(\chi_{\alpha\alpha}(k_c,\omega) = \text{Re}[\chi_{\alpha\alpha}(k_c,\omega)] + i \cdot \text{Im}[\chi_{\alpha\alpha}(k_c,\omega)])$  subsequently gives:

$$|S_{11}| = \left| 1 + \frac{2\kappa_e}{i(\omega - \omega_0 + |\tilde{g}(\omega_c)|^2 \text{Re}\left[\chi_{\alpha\alpha}(k_c, \omega_c)\right]) - (\kappa_e + \kappa_i + |\tilde{g}(\omega_c)|^2 \text{Im}\left[\chi_{\alpha\alpha}(k_c, \omega_c)\right])} \right| (2.38)$$

from which the roles played by the real and imaginary parts of the susceptibility are clearly seen: the former is responsible for the shifting of resonant frequencies of the cavity-magnon-polariton system, while the latter affects the overall dissipation rate and hence the resonant line width.

To visually illustrate the model, we take the eigen-states (fig. 2.2(d)) and corresponding MF magnetic susceptibility (fig. 2.3(c)) found for the ideal Ising model with an anisotropic hyperfine interaction, and simulate the  $|S_{11}|$  that one would obtain in experiments with cavities of three different resonance frequencies ( $f_0$ ). Since the eigen-energies are measured in units of spin-spin interaction strength, for the simulation, we set  $\mu_B = g_L = 1$  for convenience, the magnon mode line width  $\gamma = 1 \times 10^{-4} |\mathcal{J}|$ , and use correspondingly an arbitrary unit for the resonant frequency of cavity:  $f_0 = 0.3$ , 0.8, and 4.0  $E/(\hbar |\mathcal{J}|)$ .

The results are presented in figure 2.5. In fig. 2.5(a), we reiterate the eigen-states of the Ising model with hyperfine interaction strength:  $A_x = A_y = -0.2|\mathcal{J}|$ ,  $A_z = -1.0|\mathcal{J}|$ .

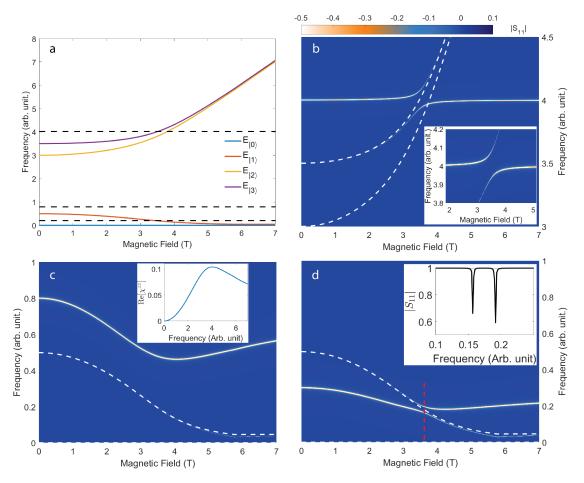


Figure 2.5: (a) Eigen-states of an ideal Ising model defined in Eq. 2.3 with an  $A_x = A_y = 0.2$   $\mathcal{J}$ ,  $A_z = 1.0$   $\mathcal{J}$ . The horizontal dashed lines represent the cavity resonance frequencies for the simulation. (b-d) On- and off-resonance  $|S_{11}|$  simulation with cavity resonance frequency at 4.0 GHz (b), 0.8 GHz (c), and 0.3 GHz (d). The white dashed lines represents the eigen-modes. The inset in (b) shows an expanded view of the anti-crossing pattern as a result of strong hybridization between the cavity mode and the spin excitation mode. The red dashed line in (d) marks the field location at which the  $|S_{11}|$  is singled out to show in the inset of the figure.

The three horizontal dashed lines are the cavity resonance frequencies chosen for the simulation. As we can read off from Eq. 2.38, when  $\chi=0$  or when there is no direct hybridization between the cavity mode and magnon modes, the  $|S_{11}|$  measured takes on a line shape with a single peak resembles that of a Lorentzian. While when there is a strong hybridization, a double peak emerges that forms a typical avoid-crossing (anti-crossing) pattern[35]. This is consistent with what is revealed in figure 2.5(b), where the resonance frequency is single-valued for the most part of magnetic field range except for near 3.5 T when the magnon mode (indicated by the white dashed lines) crosses path with, and hence

directly hybridizes to, the cavity mode. An expanded view of the avoid-crossing pattern is given in the inset of this figure, in which the symmetrical solutions to the resonance frequency of the spin-cavity ensemble as a result of strong hybridization is better visible.

An additional feature is that, despite the fact that there are two magnon modes of non-vanishing amplitudes (see fig. 2.3(c)) the crosses path with the cavity mode, only one of them ( $|0\rangle \rightarrow |3\rangle$ ) hybridized with the cavity mode while the other one ( $|0\rangle \rightarrow |2\rangle$ ) is virtually invisible. This is primarily due to the large discrepancy in the spectral weights of different modes that resulted in different coupling strengths.

In fig. 2.5(c), we have set  $f_0 = 0.8 \, E/(\hbar |\mathcal{J}|)$ , and hence no direct hybridization between the cavity mode and magnon modes are expected. Unsurprisingly, the loaded cavity resonance frequency remained single-peaked throughout the field range. However, the absence of mode hybridization does not mean no interplay between the cavity mode and magnon modes. Instead, in this case, it is manifested as the position of the resonance peak being shifted non-monotonically with increasing magnetic field strength due to changes in the real part of magnetic susceptibility. The direct correlation of functional behaviors between  $\text{Re}[\chi^{zz}]$  and the loaded cavity resonance frequency is observed with the inset of fig. 2.5(c), in which the real part of the AC magnetic susceptibility at  $0.8 \, E/(\hbar |\mathcal{J}|)$  is plotted as a function of magnetic field. The cavity resonance frequency and  $\text{Re}[\chi^{zz}]$  are seen to display the opposite trend as the field strength is increased from 0 to 7 T, in accordance with the description of Eq. 2.38.

Finally, we show in figure 2.5(d) another example of direct hybridization of cavity and magnon modes with the inset showing the symmetrical solutions of resonance frequencies of the cavity-spin ensemble at  $\sim 3.68$  T (marked by the red dashed line in the main frame of the figure. For this case, we increased the filling factor ( $\eta$ ) by almost ten fold from that in figure 2.5(b). The tails of the avoid crossing pattern now extends over much wider field range, revealing more parts of the magnon modes underneath as seen by comparing to the magnon mode represented by the white dashed line. Recalling the missing mode in figure 2.5(b) and the weaker avoid crossing pattern, these two figures show the importance of increasing coupling strength, by bigger filling factors, longer effective spins, etc, when using the RF cavity as a spectroscopy method.

For the last part of the chapter, we conduct a dimension analysis on the various quantities, as one of the measures to validate our model. First, we define the glossary using SI unit system: [J], [T], [s], [m], and [rad] represent respectively the unit Joule, Tesla, Second,

Meter, and radian. Then recall our definition of filling factor and it is easy to show that:

$$[\eta_c^2] = \frac{|\int_{V_s} \hat{e}^{\alpha} \cdot \vec{B}(r) e^{i\mathbf{k}_c \cdot \mathbf{r}} dr|^2}{[V_s \int_{V_c} |\vec{B}(r)|^2 dr]} = \frac{|[T][m^3]|^2}{[m^3][T]^2 [m^3]} = 1$$
(2.39)

which shows that the filling factor is a dimensionless parameter. Next we turn to the generalized susceptibility  $\chi$  from Eq. 2.11:

$$\begin{split} [\chi_{\alpha\alpha}] &= [\sum_{m,n,i} \frac{\langle m|\hat{\mu}_{i}^{\alpha}|n\rangle\langle n|\hat{\mu}_{i}^{\alpha}|m\rangle}{E_{n} - E_{m} - \hbar\omega + i\hbar\gamma} (P_{m} - P_{n})] \\ &= \frac{[\mu_{B}]^{2}}{[J]} [1] = \frac{[J/T]^{2}}{[J]} \\ &= [J][T]^{-2} \end{split} \tag{2.40}$$

In Eq. 2.37, the pre-factor of the susceptibility is  $|\tilde{g}(\omega_c)|^2$ , thus we also examine the dimension of this coefficient:

$$\begin{split} [\tilde{g}(\omega_c)^2] &= [\eta^2 \frac{\mu_0 \omega_c \rho_s}{2}] \\ &= [1]^2 [\frac{J}{mA^2} \frac{\text{rad}}{s} \frac{1}{m^3}] = [\frac{J^2}{m^4 A^2} \frac{\text{rad}}{s} \frac{1}{J}] \\ &= [T]^2 [J]^{-1} [\text{rad/s}] \end{split}$$
(2.41)

Thus  $[|\tilde{g}(\omega_c)|^2\chi_{\alpha\alpha}(k_c,\omega_c)] = [J]^{-1}[T]^2[J][T]^{-2}[\mathrm{rad/s}] = [\mathrm{rad/s}]$ , which has the same unit of angular frequency, consistent with the rest quantities in the denominator of Eq. 2.37. Since we have already defined  $\kappa_e$  as the dissipation rate, which is also in unit of angular frequency after being multiplied by a  $2\pi$ , it is therefore straight forward to see that  $|S_{11}|$  is a dimension less quantity. This concludes our dimension analysis of the model as a consistency check.

# 3 MF-RPA model for LiHoF<sub>4</sub>

In this chapter, we present detailed results from MF-RPA calculations using previously described theories and show some of the findings. Dictated by the logical steps taken, the chapter is divided roughly in two parts: Mean field calculations and dynamic susceptibility. First, we establish the direct relation between  ${\rm LiHoF_4}$  and Ising model in order to both show relevance of preceding contents, as well as to provide some anticipation about the magnetic properties of  ${\rm LiHoF_4}$ . Then we give MF solutions to the full hamiltonian of  ${\rm LiHoF_4}$  before using it to compute its AC susceptibilities both with and without random phase approximation. In order to show the validity of our theoretical model, and gain insights into the complex physics involved in  ${\rm LiHoF_4}$ , we carry out our calculation piece by piece, starting from the bare minimum of the Hamiltonian, and at each step add an additional term until the full spin Hamiltonian is constructed.

# 3.1 Connection to the Ising models

## 3.1.1 Ising model with exchange anisotropy

LiHoF<sub>4</sub> has a Scheelite crystal structure ( $|\vec{a}| = |\vec{b}| = 5.175$  Å,  $|\vec{c}| = 10.750$  Å[60]) that exhibits S<sub>4</sub> point group symmetry. The crystal structure is shown using a conventional unit cell in figure 3.1(a-c). Furthermore, as indicated by the spin configuration in the ordered state in fig. 3.1(d), nearly all contributions to the effective magnetic moment in LiHoF<sub>4</sub> come from the 4f electrons in Ho<sup>3+</sup>, whose electronic configuration is  $[Xe]4f^{10}$ . By Hund's rule, this configuration gives an orbital angular momentum of 6 and spin angular momentum of 2, resulting in a total angular momentum of 8 by so called L-S coupling. Consequently, the effective spin of Ho<sup>3+</sup> can assume 2J + 1 = 17 values within the first

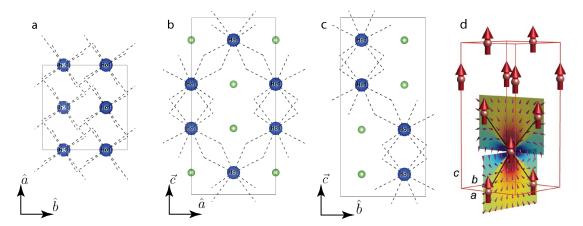


Figure 3.1: (a) The crystal structure of a conventional cell of LiHoF<sub>4</sub> in crystallographic abplane (a), ac-plane (b), and bc-plane (c). Illustrations drawn using Vesta3[53](d): Electronic spin configuration of LiHoF<sub>4</sub> in the ordered state. Figure credit: Ref. [42]

#### manifold.

As previously shown in Eq. 2.1 in Chpt. 2, the transverse (as well as longitudinal) Ising hamiltonian is bipartite, with one term capturing the inter-spin interaction and the other for the usual Zeeman interaction that contains the most important tunable parameter in an experiment, namely the external magnetic field. With respect to the inter-spin interaction, it is dominated by the dipole-dipole interaction in  $\text{LiHoF}_4$ , hence one may naively write the following bipartite hamiltonian to describe  $\text{LiHoF}_4$ :

$$\hat{\mathcal{H}} = -\sum_{i \neq j} \sum_{\alpha\beta} \hat{J}_i^{\alpha} [(g_L \mu_B)^2 D_{ij}^{\alpha\beta} + J_{ex}] \hat{J}_j^{\beta} - g_L \mu_B \sum_i \hat{J}_i \cdot \vec{B}$$
(3.1)

where  $D_{ij}^{\alpha\beta}$  is the dipole interaction tensor, and  $J_{ex}$  is the antiferrogmagnetic exchange interaction tensor, that is only finite among the nearest neighbors, with all of its principle axis elements equal to 0.1  $\mu$ eV[61].  $\alpha$  and  $\beta$  again are used to denote Cartesian components.  $\hat{J}$  is the electronic spin operator that can take any integer value between -8 and 8, and  $\vec{B}$  is the external magnetic field that is considered homogeneous across the crystal.

However, despite of the similar appearances, the hamiltonian in Eq. 3.1 does not qualify  $\text{LiHoF}_4$  as an Ising magnet since the dipole-dipole interaction couples not just the spin projections along the quantization axis on different sites but projections along all axes together. Secondly, due to the possible values of J, the present model involves seventeen eigen-states instead of two as in the case of Ising model. In order to see the latter point more clearly, we diagonalize this hamiltonian at zero temperature under MF approximation

and obtain corresponding eigen-states as well as spin expectation values.

To start, we first have to compute the long range dipolar interaction, which is numerically trivial under the MF approximation (this is due to the fact that all spins on the lattice are considered equal by MFT and therefore the spin operator can be separated from the summation/integration over the real space and to become merely a multiplicative factor). As a test, we summed over spherical single domains of different radii measured in unit cells of  $LiHoF_4$ , the resulting energy convergence is presented in figure 3.2 as a function of summation range, where we compare energies from summation over various ranges but below 300 unit cells to that over exactly 300 unit cells. The result shows that the summation converges to less than 0.1% of error (inset) by the time it reaches 100 unit cells.

Therefore, for the calculation,  $\sum\limits_{j}D_{ij}^{\alpha\beta}$  is summed over a spherical single domain, centered around site "i", that has an radius of 100 unit cells. Then a Lorentz term  $(\frac{4\pi}{3})$  was added after the summation to obtain the effective mean field dipolar coupling strength at zero wave vector. As a checkpoint, we note that our results for the longitudinal part  $(\sum\limits_{j}D_{ij}^{zz}=6.821~\mu\text{eV})$  is of the same value obtained in Ref. [61] and only marginally bigger than that in Ref. [48].

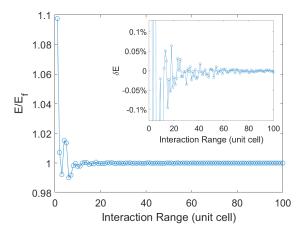


Figure 3.2: Ratio between the dipolar energy at different summation ranges and that over 300 unit cells. Horizontal axis measures in unit cells. Inset: normalized error in reference to the dipolar energy summed over 300 unit cells

The solutions to Eq. 3.1 are then plotted in fig. 3.3(a, c) for the longitudinal field case and in fig. 3.3(b, d) for the transverse field case respectively. The blue lines in Fig. 3.3(a) and (b) represent the eigen-energies in units of GHz while the red dashed lines represent the excitation spectra. Given the allowed values of  $|\vec{J}|$ , the eigen-states split into 17

non-degenerate symmetrical states due to the dipolar interaction, and evolve as functions of the external magnetic field owing to the Zeeman interaction. Moreover, all  $\delta I^z=1$  excitations can be seen to collapse onto the first excited state, indicating all eigen-states are equally spaced in energy. In figure 3.3(c, d) we plot the expectation values of Cartesian components of spin operators at zero temperature. The spins are always polarized under a longitudinal field in the first scenario as expected, whereas in the transverse field model, the system indeed ferromagnetically orders along the easy axis until the external magnetic field overcomes it and force the system to go through a quantum phase transition into polarized paramagnetic state. Hence, by combining the two sets of figures, it is easy to see that, despite the ferromagnetic order and subsequent continuous phase transition to paramagnetic order at higher fields, it cannot be reasonably regarded as a two-level system at any given point.

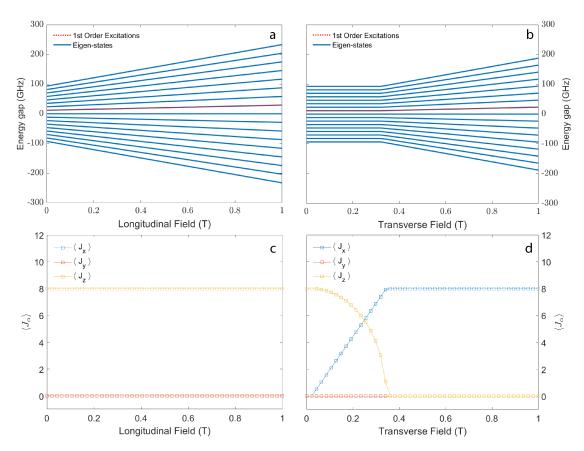


Figure 3.3: (a, b) Single-ion eigen-states (blue lines) and the corresponding excitation spectra (red dashed lines) among neighboring states in energy ( $\delta I^z = 1$ ) for the Hamiltonian defined in Eq. 3.1 under longitudinal (a) and transverse (b) magnetic fields respectively. (c, d) MF expectation values for the three Cartesian components of the electronic spin operators as functions of longitudinal (c) and transverse (d) magnetic fields.

This thus leads us to an important ingredient that ultimately allows us to characterize LiHoF<sub>4</sub> as an Ising system, which is the crystal electrostatic field (CEF). As previously stated, in the ionic state of Ho in isolation, the eigen-states of the magnetic hamiltonian are 17-fold-degenerate in accordance with the degeneracy of  $\langle \hat{J}^z \rangle$ . However, this degeneracy is lifted due to the presence of crystal electrostatic field in LiHoF<sub>4</sub>, and results in a non-Kramers doublet as the ground state owing to the fact of that the effective spin isn't a half integer. These doublet states are what lay the foundation for a direct mapping of LiHoF<sub>4</sub> 's hamiltonian onto that of an ideal Ising model without the spin-spin interaction term. To demonstrate this mapping in detail, we trim the full magnetic hamiltonian of LiHoF<sub>4</sub> down to only the CEF term and the Zeeman term. The former can be conveniently expressed using Steven's operators with appropriate prefactors that have been refined over the past decades [7, 13, 60, 4]. For the present study, we use the values given in Ref. [61] with a minor refinement to  $B_6^4(c)$ , details of this choice can be found in the appendix B. Now the hamiltonian reads:

$$\hat{\mathcal{H}} = \underbrace{\sum_{l=2,4,6} B_l^0 \hat{O}_l^0 + \sum_{l=4,6} [B_l^4(c) \hat{O}_l^4 + B_l^4(s) \hat{O}_l^4] - g_L \mu_B \sum_{i} \hat{J}_i \cdot \vec{B}_i}_{\hat{\mathcal{H}}_{Zeeman}}$$
(3.2)

where  $\hat{O}_{l}^{n}$  are the Steven's operators and  $B_{l}^{n}$  are corresponding coefficients.  $g_{L}$  and  $\mu_{B}$  are Landé factor and Bohr magneton respectively. The calculated results are given in figure 3.4.

In fig. 3.4(a), the 17 now again non-degenerate eigen-states can be seen to evolve as functions of the magnetic field with uneven spacing in energies. More importantly, the ground state doublet (highlighted in red) is separated from the rest of the states by more than 10 K throughout the entire magnetic field range. Consequently, at temperatures far smaller than this energy separation, a subspace of the Hilbert space spanned by the ground state doublet can adequately capture most of the spin physics of LiHoF<sub>4</sub>. A expanded view of these two states is given in Fig. 3.4(b), and they are seen to be degenerate at zero field but develop an energy gap between each other at finite fields. If we label these two states  $|0\rangle$  and  $|1\rangle$ , it can then be shown that  $\langle 0|\hat{J}^z|0\rangle = -\langle 1|\hat{J}^z|1\rangle$  everywhere and  $\sim 5.54$  at zero field, which is consistent with previous reports[13, 48]. This symmetry in the expectation value of  $\hat{J}^z$  of the ground state doublet, and ultimately the wavefunctions themselves, serves as another corner stone that allows one to equate this pair of ground state doublets to the spin-up ( $|\uparrow\rangle$ ) and spin-down ( $|\downarrow\rangle$ ) states in the sing model.

The ground state doublet can be expanded in the basis of eigen-vectors of the angular momentum operator  $(\hat{J}^z)$  as  $|\Psi\rangle = \sum_j \alpha_j |j^z\rangle$ , where  $\alpha_j$  is the expansion coefficient for the basis vector  $|j^z\rangle$ , and  $|\Psi\rangle$  can represent either  $|\Uparrow\rangle$  or  $|\Downarrow\rangle$ . The specific values of these complex coefficients for the ground state doublet, in absence of external magnetic fields, are numerically solved and provided in figure 3.4(c) in real and imaginary parts separately. Furthermore, the results are also presented in the form of  $sgn(\alpha_j)\sqrt{\alpha_j}$  to emphasize small but finite values. We use upward and downward triangles to represent respectively the spin-up and spin-down states. In addition, the solid lines with filled markers are used for the real parts, while the dashed lines with open markers are for the imaginary parts. In both cases, it can be seen that the two doublet states are perfectly symmetric in their components.

Thus at temperature far bellow the energy gap between the ground state doublet and the first excited state, the Hilbert space of LiHoF<sub>4</sub> can be reduced to a subspace spanned by this doublet. As a consequence of this truncation, the ranking of the total Hamiltonian in matrix form is now 2 with symmetrical diagonal elements. Since all 2 matrices can be rewritten as linear combinations of Pauli matrices and identity matrix, the single-ion hamiltonian can thus be expressed in the basis of  $(|\uparrow\rangle \pm |\downarrow\rangle)/\sqrt{2}$  as [13, 48]:

$$\hat{\mathcal{H}} = E(B_{\perp})\sigma^z - \Delta(B_{\perp})\sigma^x \tag{3.3}$$

where  $\sigma^{\alpha}$  ( $\alpha=x,y,z$ ) stand for the Pauli matrices.  $\Delta(B_{\perp})$  then serves as the effective transverse field that induces tunneling ( $\langle 1|\Delta(B_{\perp})|0\rangle$ ) between the two eigen-states. This effective field as a function of the actual magnetic field is shown in figure 3.4(d), and the inset of the which zooms in on the low magnetic field regime, it is important to note from them that  $\Delta(B_{\perp})$  behaves roughly as a quadratic function of  $B_{\perp}$ .

To understand this quadratic functional behavior, one recalls from before that every the other expansion coefficient for the ground state doublet in the basis of  $|j^z\rangle$ ,  $|j^z| = 8,7,\ldots,-7,-8$  vanishes. More specifically:  $|\uparrow\rangle = \alpha_7|+7\rangle + \alpha_{-5}|-5\rangle + \alpha_3|+3\rangle + \alpha_{-1}|-1\rangle$  and  $|\downarrow\rangle = \alpha_{-7}|-7\rangle + \alpha_5|+5\rangle + \alpha_{-3}|-3\rangle + \alpha_1|+1\rangle$ . This means that a single flip of either the spin-up or spin-down state of the ground state doublet would not result in projection to the other state, only two (or even number of times of) consecutive single flips of the same sign would do so. Since  $\hat{J}^x = \frac{1}{2}(\hat{J}^+ + \hat{J}^-)$  and  $\hat{J}^y = \frac{1}{2i}(\hat{J}^+ - \hat{J}^-)$ , a transverse field along the x-axis (or y-axis) will result in terms  $\propto (\langle \hat{J}^+ \rangle \pm \langle \hat{J}^- \rangle)$ , it would then necessarily imply that any off diagonal terms connecting the two ground state doublet  $(\langle \downarrow | \hat{O} | \uparrow \rangle)$  or  $\langle \uparrow | \hat{O} | \downarrow \rangle)$  is quadratically proportional in value to the transverse Zeeman interaction term in the

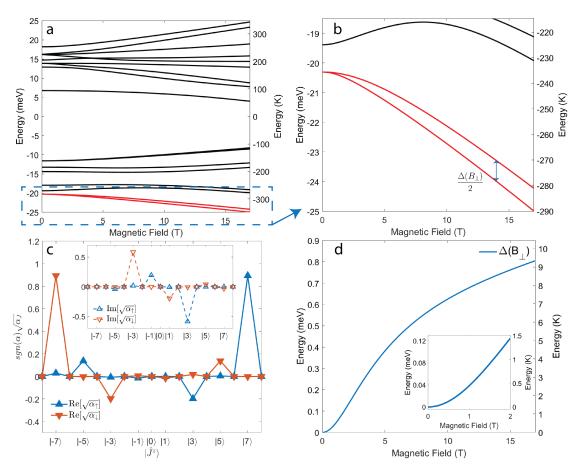


Figure 3.4: (a) Calculation of single-ion eigen-states of LiHoF<sub>4</sub> under crystal electrostatic field (CEF) splitting and a transverse magnetic field along the crystallographic a-axis (x-axis). (b) Expanded view of single-ion ground state doublet of LiHoF<sub>4</sub> shown in (a). (c) The real part of the expansion coefficients for the crystal field ground state doublet of LiHoF<sub>4</sub> at zero magnetic field. The coefficients are expressed in the basis of the eigen-vectors of  $\hat{J}^z$ . Inset: The imaginary parts of the expansion coefficients of the CEF ground state doublet of LiHoF<sub>4</sub> at zero field. (d) Effective transverse field as a function of the actual transverse magnetic field for LiHoF<sub>4</sub> upon Ising projection of the full Hamiltonian.

## hamiltonian.

In the real compound of LiHoF $_4$ , one does need to consider spin-spin interaction by dipolar and exchange interactions, but both of them only involve, to the leading order, modifications to the diagonal part of the hamiltonian [48, 19]. Therefore, we have shown that there is a direct correspondence between the magnetic hamiltonian of LiHoF $_4$  and model Ising hamiltonian.

### 3.1.2 Ising model with single-ion anisotropy

Despite of what was demonstrated in the last section, and in most literature, that LiHoF<sub>4</sub> can indeed be mapped onto the simple two-level Ising model. We have shown in Chpt. 2 Sec. 2.1 that it has deficiencies. More specifically, when the nuclear degree of freedom is included, the Ising model with exchange anisotropy can no longer qualitatively describe all the behaviors of LiHoF<sub>4</sub> without the introduction of an anisotropic hyperfine interaction. In this section, we will show that a better minimal model that captures the essential physics in LiHoF<sub>4</sub> is the Ising model with a single-ion anisotropy, whose Hamiltonian under a transverse magnetic field along x-axis reads (we set S = 1 for simplicity):

$$\hat{\mathcal{H}} = \sum_{\langle i,j \rangle} \underbrace{\mathcal{J}_{ij} \hat{S}_{i} \cdot \hat{S}_{j}}_{\text{spin-spin}} - \sum_{i} \left[ \underbrace{B^{x} \hat{S}_{i}^{x}}_{\text{Zeeman interaction}} + \underbrace{D_{z} (S_{i}^{z})^{2}}_{\text{Ising anisotropy}} \right]$$
(3.4)

where the last term introduces anisotropy with  $D_z$  being a scalar, and  $\hat{S}^z$  has three eigenvalues: -1, 0, and +1. Here  $D_z < 0$  plays the role of crystal electrostatic field in LiHoF<sub>4</sub> that energetically favors spin alignment along z-axis, resulting in single-ion ground state doublet of  $|S^z=+1\rangle$  and  $|S^z=-1\rangle$  at zero field while the  $|S^z=0\rangle$  state sits above them at a distance determined by  $D_z$ . Furthermore, with the additional Ising anisotropy term, we no longer have to require the spin-spin interaction being Ising in nature in order to model LiHoF<sub>4</sub>. But instead the inter spin interaction is kept Heisenberg like.

We then seek numerical solutions to Eq. 3.4 at 0 K and present the results in figure 3.5. For the example, we restrict the interaction range to the nearest neighbors only on a 1D spin-1 chain, and set  $\mathcal{J}_{ij} = \mathcal{J} < 0$  and  $D_z = 11$ . First, we show in fig. 3.5(a) the eigen-states of Eq. 3.4 without the spin-spin interaction term, where in total three states can be seen across the entire field range with two of which (highlighted in red) being degenerate at zero-field. This is quite easy to understand: At zero field, since  $[\hat{S}^z, \hat{\mathcal{H}}] = 0$ , the single-ion eigen-states can therefore be labelled by the eigen-values of operator  $\hat{S}^z$ :  $|S^z = -1\rangle$ ,  $|S^z = 0\rangle$ , and  $|S^z = +1\rangle$ . Due to the Ising anisotropy  $D_z(S_i^z)^2$ , a single-ion ground state doublet is formed by  $|S^z = \pm 1\rangle$  with  $|S^z = 0\rangle$  being the first excited state that sits above the former by  $D_z$  in energy. This is phenomenologically equivalent to the CEF terms in LiHoF<sub>4</sub> lifting the  $J^z$  degeneracy.

At finite transverse field, these states are mixed by the Zeeman interaction, which is off-diagonal in the basis of  $|\hat{S}^z\rangle \otimes |\hat{I}^z\rangle$ , to produce the new eigen-states of the Hamiltonian. The degeneracy of the ground state doublet is subsequently lifted, and the gap between them

is dependent of an effective transverse field that projects between these two eigen-states. Similar to the case in the previous section, this effective transverse field is quadratically proportional to the actual transverse magnetic field should the system again be projected onto the simple two-level Ising system. The numerical result of this effective transverse field as a function of the actual magnetic field is plotted in the inset of fig. 3.5(a) using a blue curve. In the same figure, a red curve representing a quadratic function of the actual field is also plotted and meant to serve as a visual guide. It can be seen that the effective transverse field indeed depends quadratically on the real field for small values of the field before becoming more linear at higher fields. The initial quadratic functional behavior is very much the same as in the LiHoF<sub>4</sub> as discussed before, a single spin flip only results in projections toward the first excited state  $\hat{S}^+|S^z=-1\rangle \rightarrow S^z=0\rangle$  ( $\hat{S}^-|S^z=+1\rangle \rightarrow S^z=0\rangle$ ), thus the off-diagonal terms that connects the two ground state doublet is as before quadratically proportional to the transverse Zeeman interaction term.

Upon the inclusion of the spin-spin interaction term, it allows the now many-body system to order, and the spontaneous symmetry breaking accompanying it introduces a finite energy gap between the ground state doublet even at zero field. At finite magnetic fields, the transverse field competes with the ordering along the Ising axis and eventually completely suppresses the spin order after inducing a quantum phase transition at the critical field. These behaviors can be readily read off from figure 3.5(b), where the MF solutions of normalized eigen-states to the Hamiltonian in Eq. 3.4 at 0 K is presented. In comparison to fig. 3.5(a), the ground state doublet are now always gapped and the excited state is pushed further up in energy.

Furthermore, excitation modes at 0 K can also be computed under MF-RPA, the results are presented in figure 3.5(b) using dashed lines. Since the red solid lines are the MF eigen-states normalized to the ground state, the upper eigen-states are equivalent to the single-ion excitation modes  $|0\rangle \rightarrow |1\rangle$  and  $|0\rangle \rightarrow |2\rangle$  respectively. In the same figure, the RPA excitation modes are plotted using black dashed lines on top of these excitations. From the comparison of the two, it is immediately clear that RPA impacts only the lowest electronic spin excitation mode, which deviates from the MF mode and softens completely at the critical field just as in all previous examples.

Next, we proceed to examine the consequences of the hyperfine interaction, to which end, we modify the Hamiltonian in Eq. 3.4 to:

$$\hat{\mathcal{H}} = \sum_{\langle i,j \rangle} \mathcal{J}_{ij} \hat{S}_i \cdot \hat{S}_j - \sum_i [B^x \hat{S}_i^x + D_z (S_i^z)^2 + A \hat{S}_i \cdot \hat{I}_i]$$
(3.5)

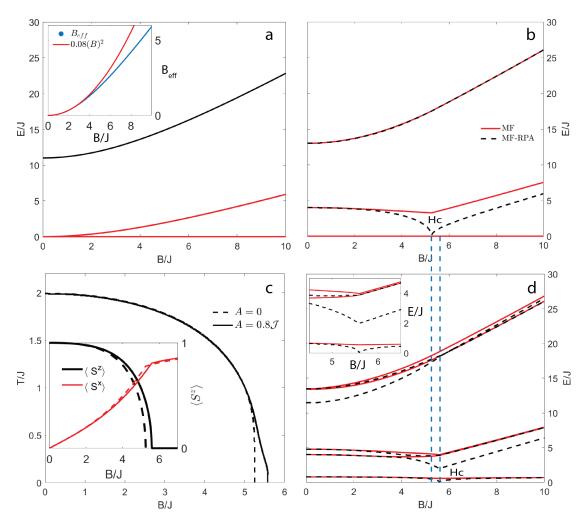


Figure 3.5: (a) Single-ion eigen-states of a Spin-1 model with single-ion anisotropy in transverse magnetic field along x-axis. Inset: The effective transverse field after Ising projection as a function of the actual transverse magnetic field. (b) MF (red solid lines) eigen-states and MF-RPA (black dashed lines) excitation modes from the ground state at 0 K for the spin-1 model with single-ion anisotropy. (c) Magnetic phase boundary of spin-1 model with (solid line) and without (dashed line) the hyperfine interaction. Inset: Expectation values of  $\langle S^x \rangle$  (red) and  $\langle S^z \rangle$  (black) for systems with (solid line) and without (dashed line) hyperfine interactions. (d) MF (red solid lines) and MF-RPA (black dashed lines) excitation modes from the ground state at 0 K. Inset: expanded view of the excitation modes near the critical field.

where  $\hat{I}_i$  is the nuclear spin moment on lattice site i, and A=0.8  $\mathscr{J}$  is isotropic. The MF solutions of normalized eigen-states to this Hamiltonian is given in figure 3.5(d) with the ground state being omitted for clarity. As expected, each state in figure 3.5(d) is now further split in two. For the MF solutions, not only the electronic ground state doublet is always gapped as in the case without hyperfine interaction, the split electro-nuclear

ground state manifold is also always gapped. In addition, it is worth noting that the first excited electronic state manifold, though appears to becomes degenerate above the critical field, it is in fact still split with a finite gap in this regime upon a close inspection of the locally expanded view shown in the inset.

The same as before, we plot on top of the MF eigen-states a set of black dashed curves representing the RPA excitation modes from the ground state at 0 K (in both the main and the inset of figure 3.5(d)). Now we see that although one of the electro-nuclear spin state in the first electronic spin state manifold still softens, such softening is no longer complete. Instead, the first excited state within the ground state manifold now softens to zero energy at the critical field. Moreover, since the contribution to the response function is dominated by the electronic moment, the impact of RPA is mostly felt by the flipping operation of electronic spins, resulting in only the electro-nuclear branch, within each electronic excitation manifold, that flips solely the electronic spin from the ground state is substantially revised from its MF values. This echos what is observed in LiHoF<sub>4</sub> as seen in figure 1.1(d) that only one electro-nuclear excitation mode from the upper electronic excitation manifold was heavily revised from the MF result inferred from figure 1.1(c).

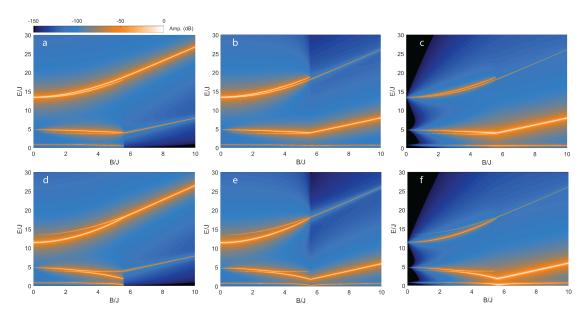


Figure 3.6: (a, b, c) The imaginary parts of the MF susceptibilities along x-, y-, and z-axis  $(\chi_{\alpha\alpha}, \alpha=x,y,z)$  for the Ising model with single-ion anisotropy in presence of the hyperfine interaction  $(A_x=A_y=A_z=0.8 \mathcal{J})$ . (d, e, f) The same as (a, b, c) but for the MF-RPA susceptibilities.

Apart from the further splitting of electronic spin states, another important effect of the

hyperfine interaction is the apparent increase of the critical field. This is made obvious by comparing figure 3.5(b) to figure 3.5(d) using the two vertical dashed lines connecting these two figures as a visual guide. The effect is similar to the case described in Sec. 2.1 of Chpt.  $2(more\ specifically\ in\ figure\ 2.2)$ . But the present model reproduces the enhancement effect on the critical field from the hyperfine interaction without the need of an artificial anisotropy in the latter. This again shows that the Ising model with single-ion anisotropy is more physically relevant to LiHoF<sub>4</sub> .

Such an enhancement of the critical field also happens at finite but low temperatures, which is illustrated in figure 3.5(c) where the magnetic phase diagrams of the present model with (solid line) and without (dashed line) the inclusion of hyperfine interaction are plotted as functions of temperature and magnetic field. The inset of fig. 3.5(c) gives the expectation values of  $\hat{S}^z$  and  $\hat{S}^x$  as functions of magnetic field at 0 K ( $\langle \hat{S}^y \rangle = 0$  and hence is omitted). The vanishing point of the  $\langle \hat{S}^z \rangle$  is used as usual to determine the critical points.

Finally, as in the previous case, we compute for both the MF and the MF-RPA magnetic susceptibilities at 0 K. Noting the spin-spin interaction is now a  $3 \times 3$  tensor, we use Eq. 2.11 and Eq. 2.16 respectively for the calculations. The results are presented in figure 3.6, and the three panels (a, b, c) are respectively  $\chi_{xx}$ ,  $\chi_{yy}$ , and  $\chi_{zz}$  for the Ising model with single-ion anisotropy in absence of the hyperfine interaction, whereas the panel (d, e, f) are the same but for the model in presence of the hyperfine interaction. In addition to the collective modes that were already revealed by the poles of RPA solutions, the susceptibilities also provide information on the spectral weight of the excitation modes. It is obvious from comparisons among each row of figure 3.6 that the spectral weight for the same mode differs depending on the specific tensor element, which eventually boils down to differences among  $\langle f | \hat{S}^x | i \rangle$ ,  $\langle f | \hat{S}^y | i \rangle$ , and  $\langle f | \hat{S}^z | i \rangle$  ( $\langle f |$  and  $| i \rangle$  stand for the final and initial states) according to Eq. 2.11.

Furthermore, some electro-nuclear modes vanish above the critical field for specific susceptibility tensor elements (e.g. the excitation mode within the electronic ground state manifold in fig. 3.6(a, d) for  $\chi_{xx}$ ). This is similar to the previous observation in figure 2.4 from Sec. 2.1 of Chpt. 2, and due to the cancellation of basis vectors. However, it is also intuitive to interpret them from a physical standpoint. Take fig. 3.6(a) as an example, above the critical field, the spins are fully polarized along the x-axis, and hence low energy response function along this direction vanishes. In other words, flipping of the nuclear spin is no longer viable through time-dependent modulation of the magnetic field along x-axis. However, at higher energies, it is still possible to flip the electronic spins, hence in

each electronic spin excitation manifold, the two branches (upper and lower) alternately vanishes above the critical field as evident in both figure 3.6(a) and figure 3.6(b).

In conclusion, we have shown that the Ising model with single-ion anisotropy has a more lucid connection to  $\text{LiHoF}_4$ , and hence is expected to be more instructive about the physics of  $\text{LiHoF}_4$ , than the Ising model with exchange anisotropy that is frequently used in the literature.

# 3.2 Mean Field Calculation for LiHoF<sub>4</sub>

Upon establishing the connection between LiHoF<sub>4</sub> and the toy models, we continue to build and solve the full magnetic hamiltonian of LiHoF<sub>4</sub>. By now, we have already gathered three ingredients, namely the CEF term, the dipole-dipole interaction term, and the electronic Zeeman interaction term. We subsequently diagonalize this hamiltonian and represent the eigen-states in blue and red curves in figure 3.7(a). Similar to the case in the previous section without dipole-dipole interaction, the inclusion of the CEF term split the 17 degenerate eigen-states unevenly along the energy axis as seen. However, in the current situation, with the inclusion of spin-spin interaction term and thus allowing the system to order, the ground state doublet is also split even in absence of external magnetic field. This can be seen more clearly in figure 3.7(b), where we provide an expanded view of the ground state doublet (highlighted in red) and the first excited singlet state from the region enclosed by a dashed box in fig. 3.7(a). A more convenient version of Fig. 3.7(b) is given in Fig. 3.7(c) by normalizing all energies to the ground state. The left and right vertical axes of both figure 3.7(c) and (d) are to the same scale but in different units.

All the experiments of the present study were carried out at temperatures below 4.3 K, which provides the first reference energy scale when considering the relevance of different eigen-states. It is clear from figure 3.7(b, c) that in this temperature range, there is no significant tunneling probability to the singlet state, only the ground state doublet are of relevance to us. Furthermore, the majority of the experiments were done at below 300 mK, and at this temperature there is also no substantial thermal occupation of the excited state of the ground state doublet. This statement can be quantified by calculating the occupation number ratio between the doublet defined as  $P_1/P_0 \approx e^{-\beta E_1}/e^{-\beta E_0}$ , where  $E_i$  and  $P_i$  are the eigen-energy and occupation number of the ith state and  $1/\beta = k_B T$ , in which T stands for temperature and  $k_B$  is the Boltzmann constant. In figure 3.8(a), we show both  $P_1/P_0$  and  $P_2/P_1$  at 300 mK to visualize the sharp contrast of occupation numbers at different

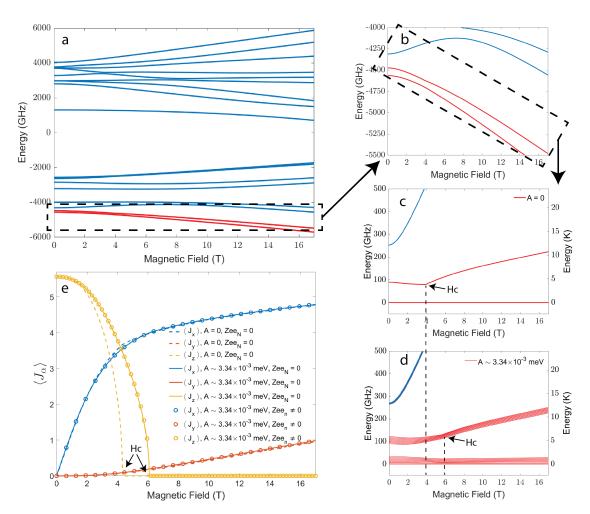


Figure 3.7: (a) MF eigen-states of LiHoF<sub>4</sub> Hamiltonian with the inclusion of CEF term under a transverse magnetic field up to 17 T. The red lines highlights the split ground state doublet. (b) Ground state doublet and the first excited singlet state. (c) The same as (b) but with eigen-energies normalized to the ground state. (d) The same as (c) but with hyperfine interaction included in the Hamiltonian. (e) Expectation values of the three Cartesian components of the electronic spin operator with (solid lines) and without (dashed lines) hyperfine interaction term in the Hamiltonian.

electronic states. It is clear from the figure that the thermal populations between the two double states are several orders of magnitudes apart, and that of the first excited singlet state is even further close to zero.

Now we add in one of the most important ingredients of  $LiHoF_4$ , namely the hyperfine interaction, and the total Hamiltonian now reads:

$$\hat{\mathcal{H}} = \hat{\mathcal{H}}_{CF} - \sum_{i \neq j} \sum_{\alpha\beta} \hat{J}_i^{\alpha} [(g_L \mu_B)^2 D_{ij}^{\alpha\beta} + J_{ex}] \hat{J}_j^{\beta} - \sum_i (g_L \mu_B \hat{J}_i \cdot \vec{B}_{\perp} + A \hat{I}_i \cdot \hat{J}_i)$$
(3.6)

where the  $I_i$  represents the nuclear spin on site "i", and we have also used the value from Ref. [61], that is  $A = 3.361 \times 10^{-3}$  meV.

The same set of electronic spin states shown in figure 3.7(c) is then recalculated with the hyperfine interaction included and the results are shown in figure 3.7(d) to provide a side-by-side comparison. We see the immediate effect of hyperfine splitting on each of the electronic states, each of which are now 8 finer eigen-states due to the 8 possible spin states of the nuclear spin  $(|\hat{I}| = \frac{7}{2})$  of Ho ions. This effect now provides us with the second important energy scale: within each electronic state manifold, the total hyperfine splitting is of an order of  $2 \cdot A |\hat{I}_{max}| = 2 \times 3.361 \times 10^{-3} \times \frac{7}{2} \approx 0.0235$  meV, or 272.7 mK. Thus it sets the upper temperature bound for resolving the hyperfine splitting in experiments.

At the MF level, since the expectation value of the spin component along the quantization axis is equivalent to the sample (spontaneous) magnetization that often is taken as the order parameter when considering magnetic phase transitions, we can therefore infer the state of ordering in LiHoF<sub>4</sub> by this expectation values along quantization axis  $(\langle \hat{J}^z \rangle)$ . We then are able to compare this value between cases of finite and vanishing hyperfine interactions, which are represented respectively by the yellow dashed lines and solid lines in figure 3.7(e). The two curves arrive at zeros at different fields, marked by the black arrows in the figure, showing a sizeable difference in critical field that is consistent with that measured between figure 3.7(c) and (d). It should be noted these two figures closely resemble fig. 3.5(d, e), echoing the connection in the physics between LiHoF<sub>4</sub> and the toy model. Subsequently, the same comparisons for the other two Cartesian components of the spin operator both yield only minute difference exclusively near the critical field. Thus we see another important effect of the hyperfine interaction, in addition to the eigen-state splitting, is the shift of critical field (Hc) toward higher values. There exist many literature that provide in-depth discussion of this phenomenon[9, 13, 60], we won't repeat the conclusion here, but rather provide a straight forward interpretation from the perspective of present MF model.

First of all, this enhanced stability of the ferromagnetic state is reminiscent of what we encountered in the Ising model in Chpt.2, explicitly shown in figure 2.2. In the previous encounter, we found that only an anisotropic hyperfine interaction can cause a shift of the critical point, whereas the hyperfine interaction in the hamiltonian described by Eq. 3.6 is isotropic at first glance. To understand the seemingly contradictory observation, we need to take into consideration of the anisotropy of electronic spin projections in LiHoF $_4$ . Similar to the previous model, A is negative, thus the nuclear spin moments again favors

alignment parallel to the electronic spin moment. Furthermore, as noted in figure 3.7(e), the effective spin for  $\hat{J}^z$  is larger than that for  $\hat{J}^x$  and  $\hat{J}^y$ , which ultimately is a result of the state mixing among the pure states due to the crystal field splitting as seen by contrasting figure 3.7(e) to figure 3.3(d). This anisotropy of effective spin projection then gives rise to an effectively anisotropic hyperfine interaction energy, leading to an increased stability of ferromagnetic state along the quantization axis. This point echos what we have found for the ideal Ising model in Chpt. 2 with the twist that here, it is not A that is anisotropic but instead is  $\langle J^\alpha \rangle$ ,  $\alpha = x, y, z$ . Hence, we conclude that the enhancement of the critical field in LiHoF<sub>4</sub> is, at MF level, a consequence of an interplay between the crystal electrostatic field and the hyperfine interaction.

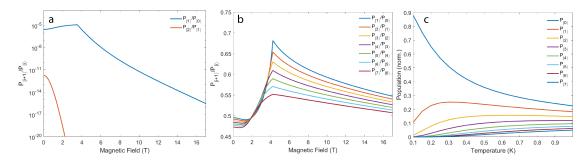


Figure 3.8: (a) Ratio of occupation numbers at 300 mK between adjacent states in LiHoF<sub>4</sub> for the first three electronic states from MF calculations without the inclusion of hyperfine interaction. (b) The same as (a) but with hyperfine interaction included. (c) The occupation numbers of electro-nuclear spin states within the electronic ground state manifold of LiHoF<sub>4</sub> as functions of temperature. Values were obtained from MFT calculations with the inclusion of hyperfine interaction, and are normalized to the ground state values.

Based on the above argument, it is then natural to ask what happens if we add the nuclear Zeeman interaction into the mix. Because of the presence of a transverse magnetic field, there is now an added indirect competition between the nuclear Zeeman interaction and the ferromagnetic state along the quantization axis. However, given the nuclear spin moment of Ho  $\mu_I = 4.173 \mu_N [17, 71]$ , where  $\mu_N = 3.15245 \times 10^{-5}$  meV/T is the nuclear magneton, one readily finds that the hyperfine interaction in LiHoF<sub>4</sub> ( $A\langle I\rangle\langle J\rangle\approx 9.41\times 10^{-2}$  meV) is about 200 times stronger than the nuclear Zeeman interaction at 4 T ( $\mu_I |\vec{B}| \approx 1.26\times 10^{-4}$  meV), therefore no sizeable effect from the nuclear Zeeman interaction should be expected. Again in figure 3.7(e), using open circles we show the MF expectation values of electronic spins with the nuclear Zeeman interaction included in the model, identified in the legend by "Zee<sub>N</sub>  $\neq$  0", and it is found that there is indeed no visible difference from the case without nuclear Zeeman interaction. However, owing to the simplicity of MFT, we will

nonetheless include in our calculations the nuclear Zeeman interaction simply defined by  $\hat{\mathcal{H}}_{nZ} = -\sum_i \vec{\mu}_N \cdot \vec{B}_{\perp}$ .

At finite temperatures, the high laying eigen-states start to mix in with the ground state through the partition function, this in turn changes the expectation values of  $\hat{J}^z$ , which again is used as the order parameter for the ferromagnetic phase. More importantly, as demonstrated in figure 3.7(e), by tracing out points in phase space where the order parameter  $(\langle \hat{J}^z \rangle)$  vanishes, we are able to acquire a magnetic phase diagram for LiHoF<sub>4</sub>. In figure 3.9(a) we show in a dashed line the phase boundary calculated in such a fashion on top of experimental data from Ref.[9] for comparison. It is clear at first glance that the MF calculation overestimates critical fields/temperatures in the entire regime. To rectify the problem, we resort to Ref. [40] and employ a renormalization factor ( $R^{-1} = 1.3004$ ) for the electronic moment to yield an effective spin value that accounts for fluctuations at higher orders, which is by definition neglected by MFT. The derivation of this renormalization factor is beyond the scope of this report and we leave the readers to Ref. [61] and Ref. [40] for more details. The resulting new phase boundary is plotted in the same figure (Fig. 3.9) using a solid line, and a much better agreement with experimental values is reached below 1.5 K. As to the large discrepancy at high temperature regime, it has been a persistent problem and an active research topic in the field. Though a recent study[19] offered an explanation beyond the MF method to the steep phase boundary near critical temperature, the final resolution of the issue is not entirely agreed upon. We therefore refrain from postulating about the mechanism, but only to note that MF calculations are known to overestimate critical temperatures since they completely ignore spin fluctuations and correlations. Despite having employed the aforementioned renormalization factor, the fluctuation near the critical temperature is far stronger an effect to be accounted for by the renormalization factor alone. Hence it should not be a complete surprise that the MF prediction fails at this part of the phase diagram, and we leave the issue for future studies with more sophisticated theoretical models.

As we have already established that at  $\leq 300mK$  there is virtually no thermal population in the excited electronic states (Fig. 3.8(a)), we therefore narrow our focus down to the hyperfine split electronic ground state manifold, whose eigen-energies at 300 mK is shown in the left panel of figure 3.9(b) and in the right panel we give the zero-field occupation number of each state. We also give the field dependence of the occupation numbers in figure 3.8(b) in the same fashion as (a). By combining these two figures and contrasting them with fig. 3.8(a), one finds that, unlike the large gap in the occupation number shown between

adjacent electronic states, the electro-nuclear states in the same manifold are populated to the same order of magnitude at 300 mK, suggesting comparable contributions from all of them to the collective response. Additionally, the zero-field temperature dependence of the thermal population is calculated and given in 3.8(c), though the thermal population for some of the states change several folds at different temperatures, all of them remain in the same order of magnitude in the entire temperature range considered.

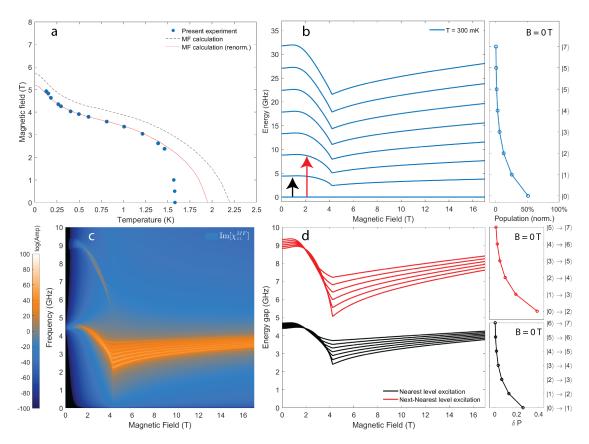


Figure 3.9: (a) Magnetic phase diagram of LiHoF<sub>4</sub>, solid circles: experimental data from off-resonance measurements of the present work. Dashed line: MFT calculation without renormalized spins. Solid line: MF calculation with renormalized spins based on Ref.[61]. (b) Left panel: The hyperfine-split electronic ground state manifold at 300 mK. The black arrow gives an example of excitations between states separated by  $\delta I^z = 1$  and the red arrow does for  $\delta I^z = 2$  excitation. Right panel: MF thermal population of the eigen-states shown in the left panel at zero field. (c) The imaginary part of the longitudinal AC magnetic susceptibility as a function of transverse magnetic field and frequency by MF calculations, the dummy spin line width used for the calculation is  $\gamma = 9 \times 10^{-5}$  meV. (d) Left panel: MF magnetic excitation spectra of the first and second order excitations as illustrated in (b). Upper right panel: differential occupation number for the second order excitations  $(P_n - P_{n+2})$ . Lower right panel: differential occupation number for the  $\delta I^z = 1$  excitations  $(P_n - P_{n+1})$ .

In addition to the spin expectation values, we can also calculate for excitation spectra of the system. In figure 3.9(b), we use a black arrow and a red arrow to indicate excitations that can occur between the  $\delta I^z = 1$  and the  $\delta I^z = 2$  excitations, whose corresponding excitation spectra are given in fig. 3.9(d). By applying the MF eigen-functions to Eq. 2.11 and using Eq. 2.15 in Chpt.2, we subsequently arrive at the AC susceptibility of LiHoF4 under RPA, represented in figure 3.9(c) as a color map at the same frequency and field range as figure 3.9(b). From comparison of the two, one immediately finds that, despite of having allowed ( $\delta I^z = 2$ ) excitations between 5 and 10 GHz, the corresponding AC susceptibility is much weaker than the  $\delta I^z = 1$  excitations. The reason for that lies in the off-diagonal matrix elements that govern these transitions. This argument can be deduced without explicitly showing the numerical values of the matrix elements as follow: use  $|i\rangle$  and  $|f\rangle$  to represent the initial and final states, recall and rewrite Eq. 2.11 as Eq. 3.7 with different ingredients color coded for best visualization. Then according to this expression, the AC susceptibility is roughly composed of three parts: a denominator (black), a numerator (red), and a multiplier (blue). The denominator determines the divergent behavior when the frequency matches the energy gap. For the calculation shown in figure 3.9(c), we arbitrarily set  $\gamma = 0.1 \mu \text{eV}$  for all the states to avoid numerical errors from the divergence. Hence this part is the same for all the spin excitation modes. The numerator part consists solely of off-diagonal matrix elements of the Hamiltonian in the chosen basis, and it hence contributes to the amplitude of the susceptibility. The multiplier is just a population factor that also moderates the amplitude of susceptibility and, importantly, it hinges on not the absolute occupation number of the states but rather the difference between the initial and final states. Therefore, in order to have a large susceptibility, it is necessary to have a large product of the off-diagonal matrix element and population factor. In the right panels of figure 3.9(b) we plot the calculated population factors of all the modes shown in the left panel and one finds they are all comparable in magnitudes, especially between the two sets of modes. At the same time, the final susceptibilities have amplitudes differ by orders of magnitudes, therefore the only logical explanation is then the corresponding off-diagonal matrix elements are different from each other by orders of magnitudes.

$$\chi_{zz}(\omega) = \sum_{i,f} \frac{\langle i|\hat{J}^z|f\rangle\langle f|\hat{J}^z|i\rangle}{E_f - E_i - \hbar\omega - i\gamma} (P_i - P_f)$$
(3.7)

Consequently, in order to couple to the cavity photon field strongly and resolve the electronuclear spin states, we restrict our focus to AC susceptibilities at frequencies below 5

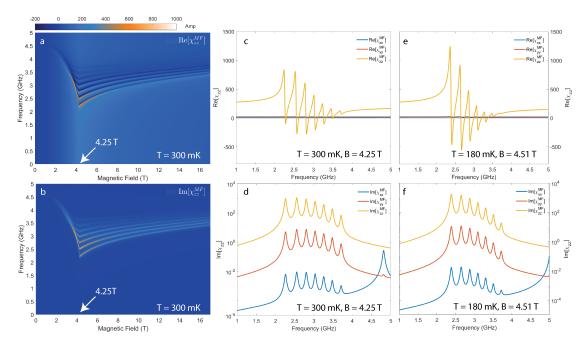


Figure 3.10: (a, b) The real and imaginary parts of the AC magnetic susceptibility from MFT calculations along the crystallographic c-axis of LiHoF<sub>4</sub> at 300 mK. (c, d) The real (c) and imaginary (d) parts of the MFT calculated AC susceptibilities of LiHoF<sub>4</sub> at  $B^x = 4.25$  T (marked by the white arrows in (a, b)) and 300 mK, presented separately for the three diagonal tensor elements. (e, f) The same as (c, d) but at  $B^x = 4.51$  T and 180 mK.

GHz for the rest of the discussion. It is found that the AC susceptibility along c-axis is the strongest[48], and a direct visualization of all the susceptibility tensor elements is provided in Appendix A. Here we use only a slice of data at 300 mK and at the critical field to compare the three diagonal elements.

In figure 3.10(a, b) we show calculated real and imaginary parts of the MF AC susceptibility along the quantization axis ( $\chi_{zz}^{\rm MF}$ ) as a function of magnetic field and frequency at 300 mK. In (c, d) of the same figure, we plot  $\chi_{\alpha\alpha}^{MF}$ ,  $\alpha=x,y,z$  at the same temperature and critical field (4.25 T) that is indicated by the white arrows in (a, b) for direct comparisons of the amplitudes among the three tensor elements. As in the previous section, we set the line width of all magnon modes to a small number ( $\gamma=0.1~\mu{\rm eV}$ ) so that it is easier to distinguish them from each other, and also to highlight differences that take place in other aspects. As to the real values of  $\gamma$  for different modes at different temperatures, we will extract them experimentally in Chpt. 5.

With respect to figure 3.10(c, d), our interpretation puts the emphasis on three important features: the first is that the real part of the AC susceptibility oscillates between positive

and negative near its poles; as we have seen in Eq. 2.38, this will shift the cavity resonant frequency up and down rapidly in the vicinity of mode hybridization. Secondly, a large peak corresponding to the excitation  $|0\rangle \rightarrow |2\rangle$  near 5 T is clearly visible in  $\chi_{xx}^{MF}$  and  $\chi_{yy}^{MF}$  in fig. 3.10(e) but not in  $\chi_{zz}^{MF}$ , this shows the importance of taking into consideration the cavity field polarization in relation to the crystallographic orientation. Finally, it is easy to see from the plots that the peak amplitudes of these three diagonal elements of the susceptibility tensor differ from each other by orders of magnitudes with  $\chi_{zz}^{MF}$  being the highest. To maximize the coupling strength between the photons and LiHoF<sub>4</sub> sample inside the cavity, we conduct all the experiments with the magnetic polarization of the cavity field arranged along the c-axis of LiHoF<sub>4</sub>.

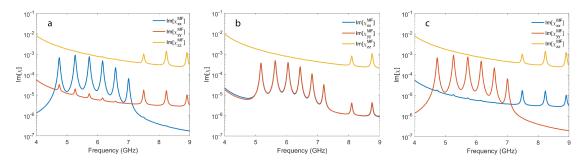


Figure 3.11: Tensor elements of the MF susceptibility at 300 mK as functions of frequencies under an external magnetic field at 4.25 T along x-axis (a), y-axis(b), and 45° in-plane (c) from both x- and y-axes.

Before moving on, we provide a brief side remark on the large peaks located around 4.7 GHz and 5.0 GHz in figure 3.10(d) and (f) respectively. These peaks, that correspond to single-ion excitation modes between eigen-states separated by  $\delta I^z=1$  as stated before, are most prominent in  $\chi_{xx}^{MF}$  and completely missing from  $\chi_{zz}^{MF}$ . Since the occupation numbers are the same regardless which spin projection one inspects, according to Eq. 3.7, the only obvious contribution to the differences in peak amplitudes are the off-diagonal elements  $\langle n+2|\hat{J}_{\alpha}|n\rangle$ ,  $\alpha=x,y,z$ . Furthermore, their amplitudes can be shown to depend on the orientation of the external magnetic field, or in another word, the polarization field. In figure 3.11(a-c), we plot calculated  $\chi_{\alpha\alpha}^{MF}$  between 4 and 9 GHz with the transverse magnetic field pointed, respectively, along x-axis, y-axis and 45° in between x- and y-axes. They show clearly that there is a correlation between the (normalized) peak amplitudes and the orientation of the polarizing field.

To demonstrate influences from the temperature, we repeat the same calculation at 180 mK and plot, in figure 3.10(e, f), a slice of the result at the critical field (4.182 T) for each

of the three diagonal tensor elements of susceptibility. In comparison to figure 3.10(c, d), while the overall amplitudes are within the same order of magnitude, there is an evident shift of it from higher frequency modes to the lower ones for both real and imaginary parts of susceptibility. This is expected due to an increase in the population factor  $(P_{|n\rangle} - P_{|n+1\rangle})$  for lower modes as a result of lower temperature and is particularly apparent for the imaginary part of the susceptibility. A steep and monotonic decrease of peak amplitudes toward higher frequencies is seen at 180 mK in contrast to that at 300 mK where all peaks have more or less the same amplitude. Thus, in terms of contribution to the bulk dynamical properties, those excitations from lower states gain more weight at lower temperatures. Furthermore, there is an overall shift of peak positions toward higher frequencies at lower temperatures as predicted by MF calculations.

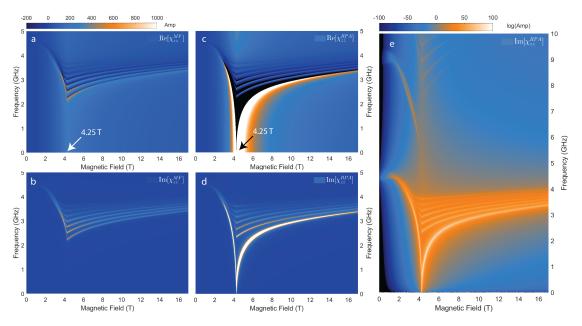


Figure 3.12: (a, b) The real and imaginary parts of the AC magnetic susceptibility of LiHoF<sub>4</sub> along z-axis ( $\chi_{zz}$ , between 0 and 5 GHz, along the quantization axis (c-axis) at 300 mK based on MFT calculations. (c, d) The same calculation but with random phase approximation (MF-RPA). (e, f) MF-RPA calculation of the AC susceptibility for LiHoF<sub>4</sub> along the quantization axis between 0 and 10 GHz.

## 3.3 RPA Calculation for LiHoF<sub>4</sub>

As the last part of AC susceptibility calculation, we apply RPA correction to the MF results at various temperatures and compare the two. Identical to the procedure in the earlier section for the Ising model with single-ion anisotropy, since the spin-spin interaction is a

tensor instead of scalar, we apply Eq. 2.16 to the previously calculated MF susceptibility tensor to obtain the RPA result. For such calculations, dipole and exchange interaction tensor at zero wave vector were obtained as previously described:

$$\sum_{j} D_{ij} = \begin{pmatrix} 3.912 & 0 & 0 \\ 0 & 3.912 & 0 \\ 0 & 0 & 6.822 \end{pmatrix}, \quad \sum_{j} J_{ex} = \begin{pmatrix} -0.4 & 0 & 0 \\ 0 & -0.4 & 0 \\ 0 & 0 & -0.4 \end{pmatrix}$$
(3.8)

In figure 3.12(a, b) we plot the real and imaginary parts of  $\chi_{zz}^{\text{MF}}$  respectively, and do the same for  $\chi_{zz}^{\text{RPA}}$  in (c, d). We remark that all four panels (fig. 3.12(a-d) share the same color scale. In comparison to the MF result, it appears that only the functional behavior of the lowest excitation mode is appreciably modified: 1. The mode now completely softens at the QCP. 2. There is an apparent and significant increase in the amplitude (spectral weight) of the lowest excitation mode that is clearly visible even from direct inspection, and is particularly pronounced near the QCP. The same calculation was also carried out at a wider frequency range shown in fig. 3.12(e), comparing to figure 3.9(c), it indeed appears that only the lowest electro-nuclear excitation mode was significantly affected by the RPA correction.

The last point becomes more evident when comparing the low energy excitation modes (within the ground state manifold of the electronic spin) at zero temperatures. In figure 3.13, we plot in solid lines MF excitation modes from the ground state  $(|0\rangle \rightarrow |n\rangle)$  as functions of transverse magnetic field, and plot in dashed lines the RPA excitation modes. A good agreement is achieved by all of them except for the lowest excitation mode  $(|0\rangle \rightarrow |1\rangle)$ , and the largest deviation takes place near the critical point as seen before. To take a closer examination, we plot a single slice of each of the two susceptibilities close to the critical field ( $B_c = 5.40$  T) in figure 3.13(b). The blue curve represents the imaginary part of the MF susceptibility and the red curve represents that of the RPA susceptibility. Using the two dashed lines connecting the two peaks and the y-axis as visual guide, one can easily see that there is a close to two orders of magnitude difference in peak amplitudes. This would naturally, by definition, mean a much stronger response to perturbations, and hence a much stronger coupling to the environment

Next we extend the investigation to the effect of RPA correction at finite temperatures. In figure 3.13(c, d), we plot isolated slice of both  $\chi_{zz}^{MF}$  and  $\chi_{zz}^{RPA}$  at 4.25 T (approximately the critical field at 300 mK) in real (c) and imaginary (d) parts. Again we use red curves for

RPA susceptibility and blue curves for the MF one. Between the two results, there is now an even larger increase of peak amplitudes for the lowest excitation mode. Comparing to Fig. 3.13(b), the RPA susceptibility peaks share very similar height, while the MF peak amplitude of the lowest mode decreased, primarily due to the thermal population spread at finite temperature. For the higher excitation mode, it is worth noting that they aren't completely free from the RPA correction, each of these modes is also red shifted to varying degrees depending on it proximity to the lowest excitation mode. It appears that the closer an excitation mode is to the fundamental mode in energy, the more red shift it experiences. At the same time, the peak amplitudes of these higher modes are barely affected. All these observations in the imaginary part of the susceptibility are consistent with those in the real parts, with a notable difference being that the amplitude change of the MF susceptibility by RPA correction is nearly three orders of magnitude.

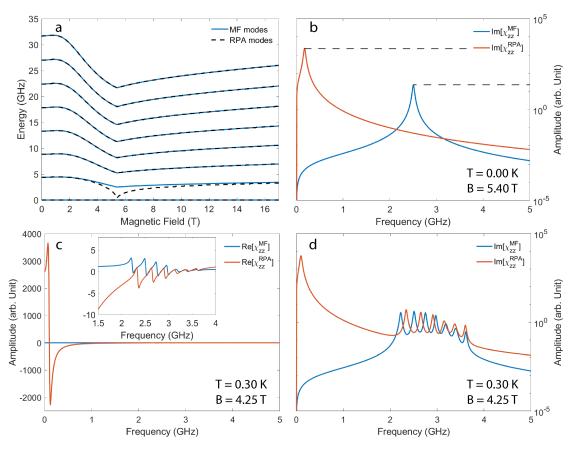


Figure 3.13: (a) zero-temperature electro-nuclear excitation modes from the ground state based on MF (blue solid lines) and MF-RPA (black dashed lines) calculations. (b) The imaginary parts of MF (blue) and MF-RPA (red) susceptibilities of LiHoF<sub>4</sub> at 0 K and 5.4 T. (c, d) The real (c) and imaginary (d) parts of the MF (blue lines) and MF-RPA (red lines) susceptibilities of LiHoF<sub>4</sub> at 300 mK and 4.25 T.

As the last note about the RPA, in principle it allows one to compute k-dependent susceptibilities. However, in the present case this is irrelevant since the wavelength of the photon field employed is far greater than the atomic spacing in LiHoF<sub>4</sub>, and we therefore are always working in  $\vec{k}=0$  limit. Hence we omit from the present document calculations of RPA susceptibilities at finite  $|\vec{k}|$ .

Before proceeding further, we take a brief detour for some practical considerations. So far we have only considered the scenario where we have a perfectly aligned transverse magnetic field, but the situations in real experiments are rarely perfect as such. Therefore, we consider two possible scenarios when, 1. the magnetic field is not perfectly aligned with one of the hard axis but remains in the crystallographic ab-plane, and 2. the magnetic field is slightly out of ab-plane and hence induces a small but finite longitudinal field. We will examine the effects of these scenarios on the single-ion excitation spectrum before investigating those on the RPA susceptibility, and finally look at their consequences on the magnetic phase diagram of LiHoF $_4$ .

In the first case, assuming the magnetic field rotates with respect to the crystallographic a-axis within the ab-plane, we denote  $\phi$  as the angle between the external magnetic field  $(\vec{B}_\perp)$  and  $\vec{e}_a$ , then the hamiltonian in Eq. 3.6 is diagonalized at zero temperature with  $\phi=0^\circ, 5^\circ$ , and  $45^\circ$  respectively. The resulting eigen-states in the electronic ground state manifold are normalized to the lowest hyperfine levels of the three angles and plotted, along with the corresponding excitation spectrum, in figure 3.14(a, c). Two important changes take place with such an in-plane rotation, the lowering of both energy and critical field with an increasing  $\phi$ , the latter is best seen in fig. 3.14(c), identified by the cusp in the magnon modes along the field axis. The mechanism behind the first changes is relatively trivial, and can be understood by considering the single-ion energy difference between  $\phi=0$  and  $\phi\neq0$ :

$$\Delta E = \hat{J}^x | \vec{B}_\perp | - (\hat{J}^x | \vec{B}_\perp | \cos\phi + \hat{J}^y | \vec{B}_\perp | \sin\phi)$$
(3.9)

$$=\hat{J}^{x}|\vec{B}_{\perp}|(1-\cos\phi-\frac{\hat{J}^{y}}{\hat{J}^{x}}\sin\phi)\geq 0 \qquad \forall \phi \in [0,90^{\circ}]$$
 (3.10)

where the condition of  $0 \le \phi \le 90^\circ$  is always fulfilled for symmetry reasons. Thus, any rotation of the magnetic field within the ab-plane necessarily lowers the energy. The second change from the field rotation is less obvious and more related to the wavefunction composition than energies; it can be made more transparent by examining the expectation values of the electronic spin operators, which vanishes at lower fields when the magnetic



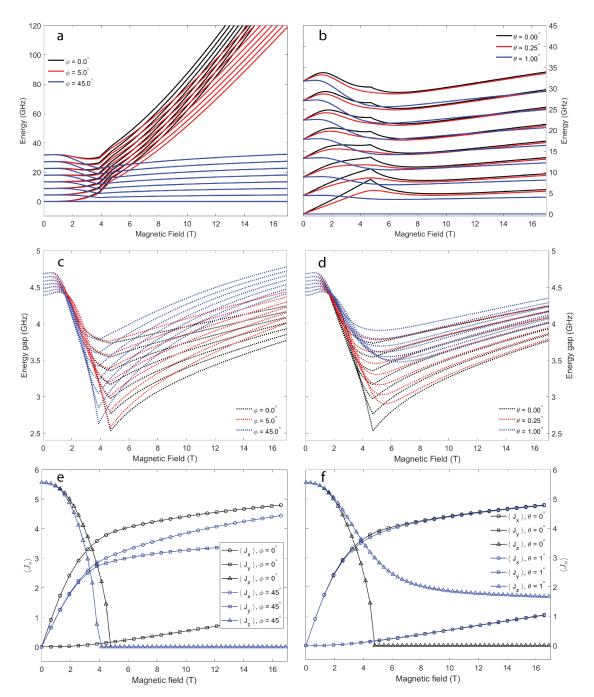


Figure 3.14: (a) Mean field eigen-energies in the electronic ground state manifold as a function of the external magnetic field at different rotation angles  $(\phi)$  within the crystallographic ab-plane. (b) The same as (a) but at different rotation angles  $(\theta)$  out of the ab-plane. (c, d) The corresponding respective electro-nuclear excitation spectra of (a, b). (e, f) The corresponding expectation values of electronic spin operators of (a, b).

For the second field rotation to be considered, we similarly define  $\theta$  as the angle between the magnetic field and  $\vec{a}$  inside ac-plane so that a finite value of this angle produces a finite longitudinal field. To isolate the effects, we fix  $\phi$  defined in the previous step to zero and only consider small angles to be relevant since its occurrence in the experiment is most likely due to misalignment and should therefore be minute. In figure 3.14(b, d) we show the MF eigen-states and first order excitations at  $\theta = 0^{\circ}$ , 0.25°, and 1°. In figure 3.14(f), we omit the case when  $\theta = 0.25^{\circ}$  for clarity and show only expectation values of electronic spins at  $\theta = 0^{\circ}$ ,  $1^{\circ}$ . In this case, the field rotation always generates a longitudinal field, which provides a bias through Zeeman interaction for the electronic spins during the spontaneous symmetry breaking at a phase transition, and determines the ordering orientation. Therefore, as long as the field polarity is not changed after the LiHoF<sub>4</sub> sample enters the ferromagnetic state,  $\theta$  is always less than 90°, and thus again always lowers the energy comparing to  $\theta = 0^{\circ}$  as shown in Fig. 3.14(b). In addition, a striking change from such a field rotation is the "rounding" of phase transition seen in Fig. 3.14(b, d). We postulate the mechanism with the help of figure 3.14(f), where we see that, while the expectation values of  $\hat{J}^x$  and  $\hat{J}^y$  barely change between the two cases of  $\theta$ , the behavior of  $\langle \hat{J}^z \rangle$  exhibit drastic change from rapidly vanishing at the critical field when  $\theta = 0$  to slowly evolving into a smaller but finite value. It suggests that, in contrary to the transverse field inducing quantum fluctuation via Zeeman interaction, the longitudinal field works against it and stabilizes the spin order, consequently halting the sharp decay of order parameter.

To see the effects that tilting angles have on the AC susceptibility under RPA, we plot  $\text{Re}[\chi_{zz}^{RPA}]$  and  $\text{Im}[\chi_{zz}^{RPA}]$  for finite  $\phi$  and  $\theta$  in figure 3.15(c, d) and figure 3.15(e, f) respectively. We also plot in figure 3.15(a, b) the case with  $\phi=\theta=0$  for reference. It is immediately clear from the figures that the soft mode persisted for a finite  $\phi$  (= 45°), with the only visible change being a steeper climb of the excitation spectra toward higher energies at higher fields in the paramagnetic phase (just as in the MF susceptibility). For a finite  $\theta$  (= 0.25°) as seen in figure 3.15(e, f), a more substantial change is apparent as a longitudinal field appears to have suppressed the complete softening of the collective excitation mode. Instead, the softening is halted at a finite frequency/energy, and a much rounded cusp is in place of the sharp transition found in the other two cases. The latter feature is consistent with the results in fig. 3.14(d) for the MF susceptibility. However, it is also different from the MF case in terms of both, that the lowest excitation mode is still red-shifted toward lower energies, and that the spectral weight is still much larger than other modes.

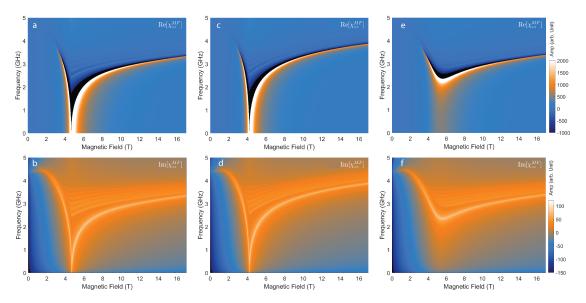


Figure 3.15: (a, b) The real and imaginary parts of the MF-RPA susceptibility of LiHoF $_4$  at 180 mK along the quantization axis (c-axis) as functions of frequency and an external magnetic field along a-axis. (c, d) The same as (a, b) but with the external magnetic field rotated within crystallographic ab-plane by 45°. (e, f) The same as (a, b) but with the external magnetic field rotated away from the ab-plane by 0.25°.

Lastly, a rotation of the magnetic field is also expected to revise the magnetic phase diagram, we therefore apply MF calculations and consider explicitly the influence of  $\phi$  and  $\theta$  on the phase boundary, which in practice is determined by identifying locations in the phase space where the order parameter,  $\langle \hat{J}^z \rangle$  in our case, vanishes. However, in the case of finite  $\theta$ , which necessarily results in a small longitudinal field , the symmetry is already broken by the longitudinal field and there isn't a real quantum phase transition. The order parameter  $\langle \hat{J}^z \rangle$  never truly vanishes, as one can see in figure 3.16(b) as an example at 1 K. Thus, in this case, despite that one may still distinguish between different phases at macroscopic levels (domain structures) as in Ref. [76]. At microscopic scale and at the MF level, the phase boundary in this case becomes ill defined.

Therefore we proceed to consider the phase diagram only when  $\theta=0$ . In figure 3.16(a), we plot calculated phase boundaries of LiHoF<sub>4</sub> under external magnetic fields within the crystallographic ab-plane on top of the experimental values obtained in the present work (details in Chpt. 5.1). The solid red and black lines are for, respectively,  $\phi=0^\circ$  and  $\phi=45^\circ$ , and the solid markers represent the experimental result. It is evident that the critical field is lowered at each temperature by the in-plane rotation of the transverse field. Due to the symmetry, it is foreseeable that the critical fields will increase back up to the original

value as  $\phi$  goes beyond 45° toward 90°, which equivalent of aligning the external field along the b-axis of LiHoF<sub>4</sub> .

In conclusion, the phase boundary is substantially revised by either rotation of the external magnetic field, and one should always bear this in mind when analyzing and comparing experimental results from different measurements.

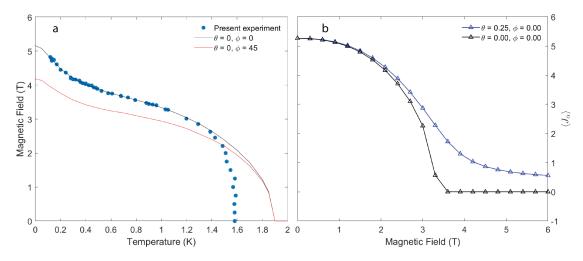


Figure 3.16: (a) Solid circles: experimentally extracted phase boundary of LiHoF $_4$  separating ferromagnetic and paramagnetic phases. Black curve: calculated phase boundary with an external magnetic field along the crystallographic a-axis of LiHoF $_4$ . Red curve: MFT calculated phase boundary with the external field rotated away from a-axis by  $\phi=45^\circ$  within ab-plane. Blue curve: MFT calculated phase boundary with the external field rotated away from a-axis by  $\theta=0.25^\circ$  out of ab-plane. (b) MF expectation values for the electronic spin in LiHoF $_4$  with an external magnetic field along a-axis (black marker-line) and that with the external field rotated away from a-axis out of ab-plane by  $\theta=0.25^\circ$ 

## 4 Experimental setup

In this section, we provide a description of the experimental setup. For conciseness, we place emphasis on the customized setup without providing unnecessary and redundant details regarding standard equipment or commercial products such as dilution refrigerator, vector network analyzer, and cryogenic superconducting magnet.

An overview of the measurement setup is illustrated in figure 4.1(a). The cavity loaded with a single crystal of LiHoF4 is placed in a dilution refrigerator (Kelvinox-400®) by Oxford Instrument. A superconducting (NbTi) coax cable mounted and thermalized to the fridge is connected between a vector network analyzer (VNA) by Rohde & Schwarz (ZVL-6 or ZNB-40) and the re-entrance cavity resonator. The RF signals generated by the VNA is injected into the cavity via a single-loop antenna, and reflected signals are collected by the same VNA for analysis of the  $S_{11}$  parameter. The red arrow denotes the relative orientation of magnetic polarization of cavity EM field  $(\vec{B}_{AC})$ , and that of the static magnetic field, labeled as  $\vec{B}_{DC}$ , is represented by the black straight arrows. The ZVL-6 unit is capable of generating RF signals at power up to +15 dBm, but in order to maintain the probe field within perturbative regime, all experimental data were taken at power less than -20 dBm, with the exception of power-dependence measurement, detailed discussion of which will be presented in Chpt. 5. The DC magnetic field is generated by a cryogenic superconducting magnet controlled by IPS-120® during the experiment and is continuously ramped at quasi-static rates in comparison to the sampling rate of VNA. In addition, the cavity temperature is measured via a thermometer mounted at the bottom of the cavity (fig. 4.1(e)), and monitored at the bottom of the cavity and measured continuously via a Lakeshore® 370 resistance bridge.

In fig. 4.1(b) we show a corner view of the design of the RF cavity in parts, with the inner

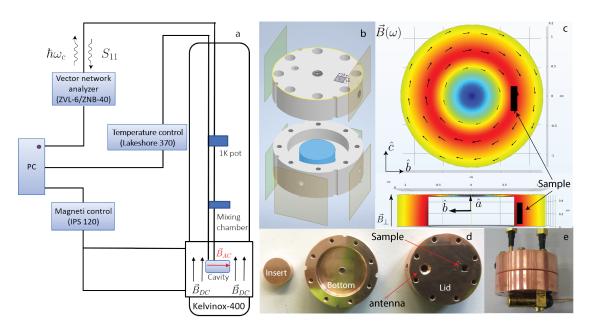


Figure 4.1: (a) Schematic illustration of the experimental setup. The red arrow denotes the orientation of magnetic polarization of the cavity EM field  $(\vec{B}_{AC})$ . Black straight arrows indicates the orientation of the external static magnetic field  $(\vec{B}_{AC})$ . Curly black arrows illustrates the traveling directions of the RF signals. (b) 3D corner view of the resonator cavity assembly used in the experiment. (c) Top view (upper panel) and side view (lower panel) of simulated magnetic flux density of the EM field inside the cavity. Small black arrows in the color plot indicates the orientation of the magnetic polarization. The black square marks the sample position inside the cavity to the scale. The black arrows at the corner of the upper panel and middle of the lower panel denote the crystallographic orientations of the sample with respect to the view angles. (d) An actual photo of the cavity assembly in parts for the present experimental study. (e) An actual photo of the assembled cavity for  $|S_{11}|/|S_{21}|$  measurements with two antennas attached to it at the top and a thermometer mounted at the bottom.

insert highlighted in blue. The cavity used in the present experiment makes use of the transverse magnetic mode in a typical cylindrical re-entrant cavity[21, 14] with a diameter of 24 mm, and height of 5 mm. Its design differs from a conventional cylindrical cavity by an inner metallic cylinder of 15 mm in diameter that protrudes out of the bottom of the cavity, but does not reach the top lid. Instead, the inner part forms a small gap from the ceiling of the cavity. In addition, apart from the screw holes along the edges that are used to assemble the cavity parts together, two openings symmetrically placed off the center can be see on the top lid, the square hole is used to orient and mount the sample holder. The four fold geometry ensures proper alignment of the crystallographic axis in relation to the magnetic polarization of the cavity field. In contrast, the round hold is for the single-loop antenna, and its high symmetry shape allows for the antenna to be rotated

continuously until the ideal matching condition is reached. Both the antenna and the sample holder are subsequently pinned down by side screws. Actual photos of the cavity assembly in parts and as a whole are given in figure 4.1(d,e). Due to the high magnetic field applied during the experiment, all parts of the cavity are made of high purity copper instead of superconducting materials. All the screws used are either made from brass or non-magnetic stainless steel to avoid distortion of field flux during the experiment, and the differential thermal contraction at low temperatures doesn't result in the loosening of the assembly.

Using COMSOL®, we are able to calculate magnetic flux density from the cavity EM field by the finite element method (FEM), and the results are presented in color plots in figure 4.1(c). The upper and lower panels of the figure show respectively top and side views of the cavity. The pairs of perpendicular arrows indicate the crystallographic orientation of the sample in each panel. The black arrows in the upper panel along the azimuthal direction indicate the magnetic polarization direction of the cavity field, which is parallel to the crystallographic c-axis of the sample as it was shown in Chpt. 3 that, the EM field couples much stronger to the spins in LiHoF4 when it is aligned such. Moreover, the color plot in both panels show the magnetic flux density from the EM field, and the sample is by design placed where the density is the highest to further maximize the coupling strength. In the lower panel, we also show the relative orientation of the static magnetic field, which is along the crystallographic a-axis of LiHoF4 and perpendicular to the magnetic polarization of the cavity field to avoid unintended AC modulation of the external magnetic field.

Owing to the small variable gap between the insert and the ceiling of the cavity, the cavity can, by design, have a fundamental mode between 1 GHz and 5 GHz for a gap size between 400  $\mu$ m to 150  $\mu$  respectively. Further more, a different diameter of the insert also affects the resonant frequency. In figure 4.2(a, b) we show simulated results of the resonant frequency of fundamental mode as a function of insert height and diameter respectively. The reason for the gap size and the insert diameter dependence of the resonant frequency can be easily understood by considering the cavity resonator again as an equivalent RLC circuit, whose resonant frequency is given by  $\omega_0 = 1/\sqrt{LC}$  and the insert forms the capacitor with the cavity ceiling. If we denote the gap size with h and the diameter of the insert as D, then the capacitance is given by  $C = \epsilon \pi D^2/4h$ , where  $\epsilon$  is the dielectric constant of the capacitor filling material, which in our case is vacuum. Combine the two expression, we easily obtain  $\omega_0 \propto 1/D \propto \sqrt{h}$ , which is fully consistent with the convex and concave shape of the curves in fig. 4.2(a, b).

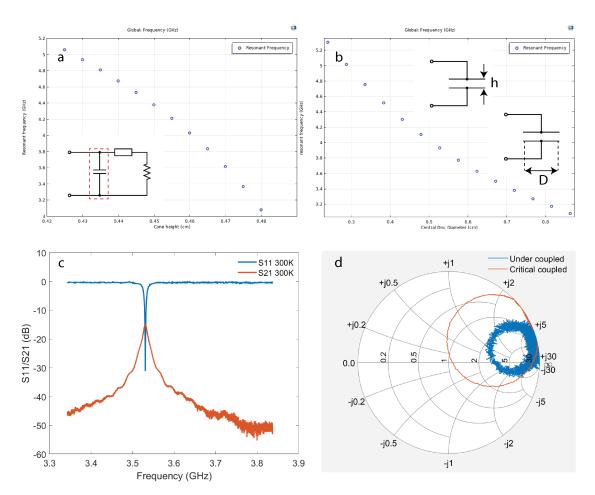


Figure 4.2: (a) Cavity resonance frequency as a function of the height of the metallic insert. Inset: the equivalent RLC circuit and the corresponding element to the insert. (b) Cavity resonance frequency as a function of the diameter of the insert. Inset: an isolated capacitor and its characteristic physical dimensions. (c) Experimentally measured  $|S_{11}|$  and  $|S_{21}|$  at room temperature of an empty re-entrant cavity used in the present work. (d) Smith chart of the experimentally measured  $|S_{11}|$  on a reentrant cavity (figure 4.1(d, e)) loaded with a single crystal sample of LiHoF<sub>4</sub> at the room temperature (~ 300 K) and at 800 mK.

The cavity is characterized without a loaded sample at room temperature, and the result is given in figure 4.2(c), where both  $|S_{11}|$  and  $|S_{21}|$  are given. A strong resonant peak is seen in  $|S_{11}|$  data between 3.5 GHz and 3.6 GHz, with a mildly noisy but mostly flat background. By the definition of quality factor  $Q = f_c/FWHM$ , where  $f_c$  stands for the resonant frequency of the cavity and FWHM is the full-width-half-maximum centered at the resonant frequency, we obtained a typical value of  $\sim$  4000 for the quality factor of the present cavity design. In contrast to measured  $|S_{11}|$ , the transmission data  $|S_{21}|$  show rather low transmission of signal even on resonance, and the background reveals

many fine structures resulting from parasitic capacitance and inductance. Partly due to this difference in data quality between  $|S_{11}|$  and  $|S_{21}|$ , all experimental data on LiHoF<sub>4</sub> in the present thesis were taken in the form of  $|S_{11}|$ . As mentioned earlier, the antenna that injects the signal into the cavity is allowed to rotate in order to fine tune the coupling condition. In practice, due to the dramatic change in magnetic properties of LiHoF4 between ordered and disordered states, it induces a drastic change of coupling condition between the two states as well, which is further aggravated by the change of impedance of the transmission line inside the dilution fridge as it cools down from room temperature to milli-kelvins. Consequently, in order to achieve (near) critical coupling at low temperatures when  $LiHoF_4$  is in ferromagnetic state, the coupling condition has to be tuned away from critical condition at room temperature. Though the amount of detuning is difficult to predict theoretically, it is possible to obtain through trial-and-error thanks to its decent reproducibility. In figure 4.2(d), we use the smith chart to show an example of such detuning and its result at low temperatures. The blue curve is the zero-field data taken at room temperature and can be seen, by large, in the over-coupled regime; whereas the red curve was taken at 800 mK and again at zero field is seen to be near critical coupling.

As previously discussed, the magnetic polarization direction of the cavity field in relation to the crystallographic orientation of LiHoF<sub>4</sub> is rather important. In Chpt. 3, we have shown how sensitive the experimental results are to misalignment of these two orientations. Therefore, to ensure a configuration where the external field and the crystallographic c-axis of  $LiHoF_4$  are as perfectly aligned as possible, a few measures are taken between sample is diced and the eventual mounting to the cavity. In figure 4.3, we use the X-ray diffraction pattern of the single crystal sample used in the present experiment, along with photos of it on the sample holder, to demonstrate the possibility of aligning the sample better than 1°. Both the cavity lid and the sample holder are made from high purity copper, and precision cut on CNC machines. While the precisely cut square guide in the cavity lid for the sample holder ensures a precise relative orientation of the sample holder to the cavity field, the contact surface between the sample holder and the crystal is made to be perpendicular to the longitudinal axis of the sample holder, and this ensures a precise relative orientation between the sample and the sample holder provided the orientation of the sample contact surface is precisely known. As a reminder, the desired relative orientation of the sample to the cavity field is illustrated in figure 4.1(b).

To achieve a precise cut surface of the sample, it is first mounted onto a goniometer with resolution finer than 0.5°. Then the sample is aligned by adjusting the three axes of

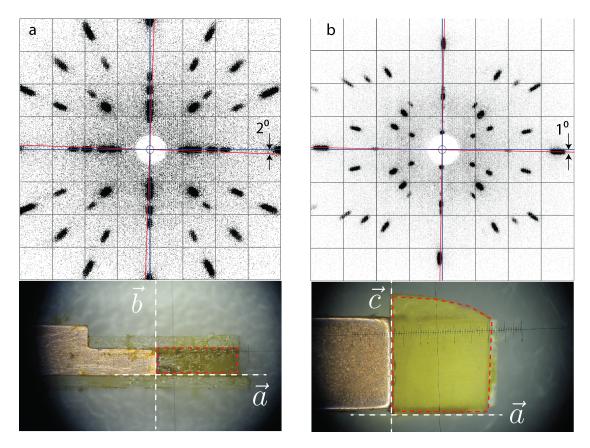


Figure 4.3: (a, b) X-ray Laue diffraction patterns of LiHoF $_4$  single crystals in crystallographic ab-plane and ac-place. The two sets of red and blue lines are guide to the eyes to demonstrate a relative rotation of  $1^\circ$  and  $2^\circ$ . (c,d) top and side views of a cut LiHoF $_4$  sample on its holder. White dashed lines give the crystallographic axes, and the red dashed boxes single out the LiHoF $_4$  crystal itself.

the goniometer under the guidance of real time Laue diffraction pattern. Examples of such diffraction patterns of LiHoF<sub>4</sub> along its crystallographic ab- and ac-planes are given respectively in figure 4.3(a, b), on top of which sets of blue and red guidelines that are rotated relative to each other are drawn to show that it is entirely possible to discern a deviation of 1° by naked eyes. To certain limit, the finer the collimator used, the better resulting angle resolution. The sample is then transferred together with the goniometer to a diamond wire saw so that the crystal can be diced precisely. In figure 4.3(c, d), we show photos of the cut sample (singled out by the red dashed lines) mounted on the holder along the contact surface, the crystallographic a, b, and c axes are marked using white dashed lines. In addition, the two bigger and exposed surfaces of the sample are reinforced with sapphire substrate to counteract the strong magnetic torque during the experiment when the transverse field is applied.

# **5** Experimental results and discussion

Here we present our experimental results and compare them to the calculations from the prior chapter. This chapter is roughly categorized under two sections: off-resonance and on-resonance experiments. The choices of cavity resonant frequencies are based on the energy scales of the first and second order modes of single-ion excitation spectrum within the electronic ground state manifold, which is presented in figure 5.1 using series of dashed lines. In both figures, the black curves represent excitations among the nearest neighboring eigen-states in energy ( $\delta I^z = 1$ ) while the blue curves are for those among the next-nearest neighboring states in energy ( $\delta I^z = 2$ ). The special excitation mode ( $|0\rangle \rightarrow |1\rangle$ ) between the ground state and the first excited electro-nuclear state is colored in red for convenience of comparing to the soft mode predicted by RPA, which is plotted also in red in the same figure in a dash-dotted line. Finally, the solid purple horizontal lines in the two figures mark the bare resonance frequencies of the cavity used for the measurements, with the two in figure 5.1(a) for off-resonance experiments and the four in figure 5.1(b) for on-resonance experiments. In practice, the experimental data are typically obtained by sweeping the cavity through a frequency window at fixed temperatures and magnetic fields at each time before stitching together individual frequency scans to form a 3D data set.

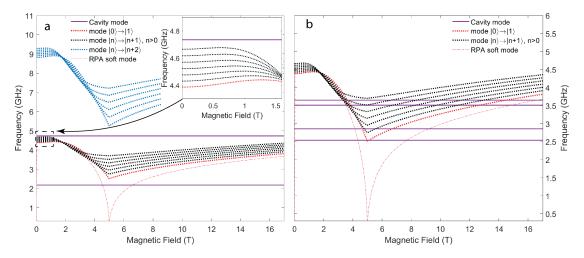


Figure 5.1: (a) Cavity resonant frequencies (purple solid lines) for the off-resonance experiments in relation to  $\delta I^z=1$  and  $\delta I^z=2$  excitation modes within the electronic ground state manifold. Inset: expanded view of the region enclosed by the dashed box in the main figure. (b) Single-ion excitation modes of  $\delta I^z=1$  and the RPA soft modes. Purple solid lines: Cavity resonance frequencies for the on-resonant experiments.

#### 5.1 Off-Resonance Results and Analysis

In off-resonance experiments, the cavity resonance frequency is detuned away from the of spin excitation modes. Hence there should be no coherent exchange of energies between the cavity photon field and the spin ensemble. The interaction between the two subsystems (the photon field and the spin ensemble) are purely classical and is expected to be characterized by classical electrodynamics. In our experiments, the scattering parameter  $|S_{11}|$  is measured as a function of magnetic field, temperature and frequency.

#### 5.1.1 Field-Ramping measurement ( $\sim 5 \text{ GHz}$ )

In the left panels of figure 5.2(a, c), we show two sets of 3D data of  $|S_{11}|$  measured at  $150 \pm 10$  mK while the magnetic field is swept from 0 to 9 T simultaneously with the frequency between 4.71 and 4.75 GHz. These data are obtained on the same sample and with the same cavity, and the only appreciable difference is that a finite longitudinal field is applied to the sample when obtaining figure 5.2(c). At first glance, the most striking feature is that the resonant frequency of the cavity changes as a function of magnetic field but remains singly peaked at the entire field range. Furthermore, the resonant frequency doesn't monotonically decrease or increase along the field axis, an inflection point can be clearly seen near the critical field ( $\sim 5$  T) in both sets of data. An important distinction

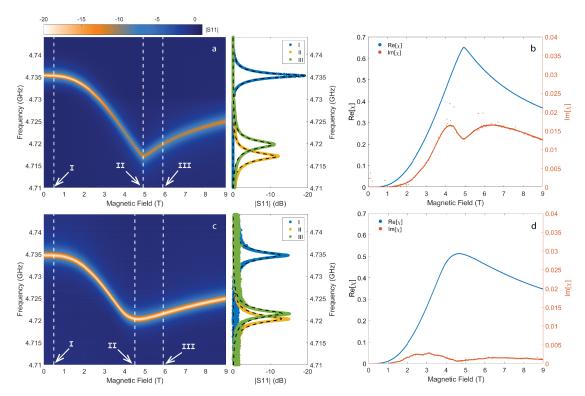


Figure 5.2: (a, c) Left panels: experimentally measured  $|S_{11}|$  parameter as functions of magnetic field and frequency on the same sample with (c) and without (a) a longitudinal field at  $\sim 150$  mK. Right panels: Individual slices of experimental data (solid markers) as functions of frequency at selected external magnetic field marked by both the arrows and white dashed lines, as the visual guide, in the left panels. Black dashed lines are numerical fits to these measurements using Eq. 2.38. Both color plots share the same color scale displayed on top of (a). (b, d) The real (blue dots) and imaginary (red dots) parts of the diagonal AC magnetic susceptibility along z-axis ( $\chi_{zz}$ ) obtained from numerical fits to experimental data in (a) and (c), respectively, as functions of magnetic field.

between these two sets of data are the shape of the inflection point, with the one in figure 5.2(a) being clearly sharper than the one in figure 5.2(c).

At each given magnetic field, the  $|S_{11}|$  response is fitted between 4.71 and 4.75 GHz using Eq. 2.38 to extract the real and imaginary parts of the AC susceptibility, examples of which at three different field values (marked by both the white dashed lines and arrows in the left panels) are given in the right panels of figure 5.2(a, c), and the experimental data is represented by color-coded markers while the fits are plotted using black dashed lines. The resulting off-resonance susceptibilities from these fits are shown in figure 5.2(b, d), whose real parts (blue dots) are seen to peak at the critical field, demonstrating a similar but inverted trend of the resonant frequency as expected. In contrast, the imaginary parts of

the susceptibilities show surprising double peaks on the opposite side of the critical field, whose origins are not obvious since, at  $\sim 4.73$  GHz, the cavity mode and electro-nuclear excitation modes in LiHoF<sub>4</sub> don't coincide in the given magnetic field range (see fig. 5.1 (a)).

To understand the behavior of the experimental data and its implication, we turn to our models. Since it is assumed that  $|\omega-\omega_c|\gg\gamma$  for single-ion excitations in an off-resonance measurement,  $\gamma$  in the denominator of Eq. 2.11 is of no importance. This enables us to calculate susceptibilities without the actual knowledge of spin line widths. By setting  $\gamma=9\times10^{-4}$  meV, we compute  $\chi_{zz}^{MF}$  from Eq. 2.11 and subsequently  $\chi_{zz}^{RPA}$  from Eq. 2.15 at experimental temperatures, which are eventually plugged into Eq. 2.37 to simulate measured  $|S_{11}|$  as functions of frequency and field.

The calculated resonance frequencies as functions of magnetic field are presented as black (MF) and red (RPA) dashed lines on top of experimental data in color maps in figure 5.3(a, b) to provide a direct comparison. In both figures, a small discrepancy can be seen between the experimental values and those from MFT, from which we deduce that the longitudinal field in figure 5.3(b) is of 0.26% of the transverse field, equivalent to a tilting angle less than 0.5° from the ab-plane. In contrast, the RPA results yield a much poorer agreement with the experiment. What's more, apart from the curvature discrepancy displayed by both comparisons, an additional discrepancy of the locations on the field axis of the cusps along the resonance frequencies between the experimental and theoretical values are also apparent in figure 5.3(b), which are highlighted using two vertical white dashed lines. We shall discuss this shortly.

The minute "amplitude" discrepancy along the frequency axis between the MF and experimental results, in both figure 5.3(a), is attributed to the imprecision of FEM modeling of the dimensions of LiHoF<sub>4</sub> and its position inside the cavity. In other words, it is considered an uncertainty originating from the filling factor ( $\eta$  in Eq. 2.30), and once corrected by a 6% inflation of the theoretical values for both figure 5.3(a, b), shown using solid black lines in figure 5.3(c, d), the model appears to achieve an excellent agreement with the experimental data. As for the RPA results however, the large discrepancy along the frequency axis is only resolved with a scaling of the filling factor by 32%, shown using solid red lines in figure 5.3(c, d). It is much too large to be considered a mere uncertainty and the resulting curves also displayed very different line shapes from the experimental data. Both imply that the RPA correction to the MF off-resonance susceptibility is beyond simple scaling of amplitudes, and therefore the resulting disagreement with the experimental data cannot

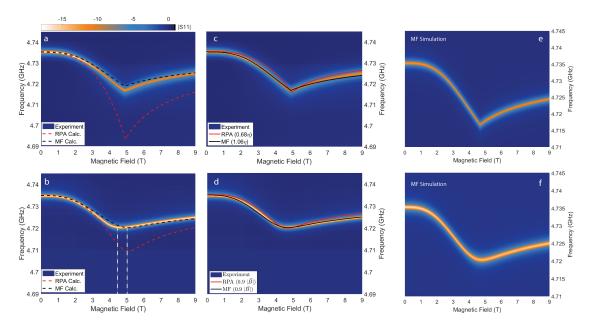


Figure 5.3: Color maps in (a-d): experimentally measured  $|S_{11}|$  parameter as functions of transverse magnetic field and frequency on the same sample and in the same cavity, without (a, c) and with (b, d) a longitudinal field of 0.26% of the transverse field. Dashed lines in (a, b): The resonance frequencies of the spin-cavity ensemble as functions of magnetic field without adjustment, calculated by the MFT (black) and MF-RPA (red). The white dashed lines in (b) are intended as visual guide to the QCP mismatch. Solid lines in (c, d): The resonance frequency with corrected filling factors (c) and adjusted critical field (d), obtained from the MFT (black) and MF-RPA (red) calculations. (e, f) Simulations of  $|S_{11}|$  shown in (a) and (b) respectively by the MFT.

be resolved by a simple multiplicative factor to the filling factor.

Since we were able extract the real and imaginary parts of AC susceptibility from the experimental data, we proceed to compare them to calculated values as well. In all four panels of figure 5.4, experimental values for the real and imaginary parts of susceptibility are presented in blue and red dots, while the theoretical values for those are given in black solid and dashed lines respectively. For both the cases without (figure 5.4(a)) and with (figure 5.4(b)) longitudinal field, MF calculations and experiment reached good agreements on the real part of susceptibility, whereas that between the RPA and experimental results shown in figure 5.4(c, d) did not, consistent with the observations on  $|S_{11}|$ .

Similar to figure 5.3(b), we used two vertical dashed lines as a visual guide in figure 5.4(d) to highlight the shifted critical field. On the surface, it is tempting to brush off this shift in critical field by projecting doubts onto the measurement accuracy of the sample temperature. However, a quick MF calculation reveals that only a temperature difference

greater than 100 mK can bring the theoretical and experimental results together, and it is achieved not without loss of agreements in other parts of the data. This value far exceeds any reasonable error tolerance for calibrated thermometers in this temperature range. Moreover, since both measurements with and without the longitudinal field were taken using the same setup, the same sample, and the same parameters, there is no apparent reason for one to treat their accuracy differently.

Thus we sought after explanations elsewhere, and incidentally, it appears to be consistent with a recent finding in Ref. [76], where a shift of critical field toward lower field in AC susceptibility measurement is discussed in detail. The author of this report concludes that the discrepancy roots from the symmetry breaking at the microscopic and the mesoscopic scales do not coincide with each other on the field axis as a result of finite longitudinal field. A detailed calculation and subsequently quantitative comparison to the experimental results is provided and presented in fig. 1(h) and fig. 3(e-i) of Ref. [76], and we refer readers to the literature for further details. According to Ref. [76], in order to predict the correct critical field, one in practice is required to take into consideration of the magnetic domain structure. In the present work, although the dipole-dipole interaction summation takes into consideration of the domain shape, it does not account for broken symmetries caused by the longitudinal field and therefore unable to capture the physical consequence of it. However, as noted in Ref. [61], the renormalization of the effective electronic spin from higher order contributions to the self-energy will result in a shift of the critical field without affecting the critical behavior itself. Therefore, instead of crudely scaling the data along the field axis, we fit for the best renormalization factor of the effective spin to yield the correct critical field in cases where the longitudinal field is finite. We note that such correction is always applied to the MF and MF-RPA results equally and simultaneously.

In moving forward, the theoretical predictions for the imaginary part of AC susceptibility in all four panels of figure 5.4 also show qualitatively different behaviors from those of experimental data that was not revealed in the previous comparison of  $|S_{11}|$ . In both fig. 5.3(a, b), a set of double peaks is observed surrounding the critical field in the fitted imaginary part of susceptibility, yet they are completely missing from both MF and MF-RPA calculated results. In addition, for the case without longitudinal field (fig. 5.4(a, c)), the amplitudes of the imaginary part, in contrast to the real parts, differ by up to one order of magnitude between theoretical and experimental values. For the case with longitudinal field (fig. 5.4(b, d)), though the magnitudes between MF predicted and measured values are in a reasonably good agreement in terms of the magnitude (fig. 5.4(b)), it is not the

case for the RPA results (fig. 5.4(d)).

What's most intriguing is that these double peaks in the imaginary part of the AC magnetic susceptibility surrounding the QCP, or conversely can be viewed as a dip at the QCP in an otherwise slow evolving curve, resemble the double peaks discussed in Ref. [45], in which they were taken as signatures of weakly interacting modes hybridizing with the cavity mode. Though this mechanism is entirely possible (since hybridization with extremely broad excitation mode does manifest as an elevated dissipation rate, which is characterized by the imaginary part of susceptibility), the observation in figure 5.4 is most definitely not the same spin excitation mode as observed in the aforementioned literature, because the cavity resonance frequency chosen here is above the first electro-nuclear excitation mode ( $|0\rangle \rightarrow |1\rangle$  in fig. 5.1(a)). Therefore if these double peaks were to be interpreted as hybridization between cavity field and spin excitation modes, it is not from the RPA soft mode discussed in Ref. [48] & Ref. [45]. However, it goes without saying that other possibilities exist, for example, it could be from a higher order correction to the MF eigenstates that resulted in excitation modes appearing in this frequency window, or it could be an outcome of mode-mode interactions that shifts the collective mode in energy. Both of these potential mechanisms are not included in our present model.

In spite of the failure of RPA in the present case, the good agreement between the MF results and the experiment nonetheless allows us to make some physical interpretations of the experimental data: On the one hand, the resonant frequency as a function of magnetic field experiences an inflection point exactly at the quantum critical point simply due to the divergence of the real part of AC susceptibility, as is described by the diverging denominator of Eq. 2.38. On the other hand, as we have already seen in figure 3.14, a small longitudinal field has the effect of "rounding" the quantum phase transition. This is directly manifested in figure 5.3(b, d), where a longitudinal field that is < 0.3% of the transverse field causes the loss of sharpness in the line shape of the resonance frequency trace. For a direct visualization, we simulate  $|S_{11}|$  using the single-ion susceptibility and present the results in figure 5.3(e, f) in the same fashion as the experimental data shown in figure 5.3(a-d).

In terms of the large discrepancy between the RPA and experimental results. It appears to be consistent with observations made in an recent report (Ref.[49]), where the authors hypothesized that, due to an ultra strong coupling to its environment, the coherence time of the collective mode predicted by RPA is extremely short and in the order of hundreds of GHz, causing the mode to rapidly decay into single-ion modes (MF modes) on a pico-second

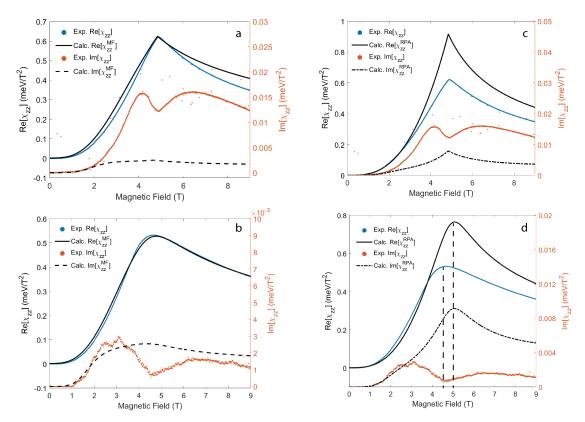


Figure 5.4: (a-d) Blue and red dots represent experimental values of the real and imaginary parts of the AC magnetic susceptibility of LiHoF $_4$  obtained from numerical fits to data presented in Fig. 5.3(a-d). Solid and dotted-dashed lines are theoretical predictions for the real and imaginary parts of the susceptibility under MFT (a, b) and RPA (c, d). The vertical dashed lines in (d) are for visual guide only.

time scale. Consequently, when probed in CW mode, one is effectively always measuring the single-ion excitation spectrum.

As the last remark, we comment on the appreciably smaller amplitude in the imaginary part of susceptibility when a longitudinal field is applied. The difference is readily seen by comparing Fig. 5.4(a) and Fig. 5.4(b). As previously stated, if we were to attribute the increase in  $\text{Im}[\chi_{zz}]$  to dissipative coupling between the cavity mode and spin excitation mode, we then can reasonably assume that a longitudinal field would suppress such dissipation channels by stabilizing spins through polarization, and effectively weaken the hybridization. We stress again that these are speculations rooted in our understanding of the system and experimental observations. The eventual resolution of these discrepancies between experiment and theories necessarily a requires more sophisticated theory that goes beyond MF-RPA, which lies both outside of the current expertise of the author and

the scope of this report, we therefore leave it for future projects.

We repeat these measurements at various temperatures up to 800 mK and show the results in figure 5.5, where we plotted real and imaginary parts of the susceptibilities in figure 5.5(a) and figure 5.5(b) separately, the temperature series are color coded in the same fashion for both experimental and simulation results, and are coordinated between the two panels. In response to the poor agreement between the RPA and experimental results demonstrated above, we now only compare the latter to MF calculations for analysis. But shall return to RPA from time to time for other measurements.

The same as previously with the real part of the susceptibility, MF results yield good agreement with the experiments at all temperatures across the entire field range except for the region near the critical fields. This is understandable, considering MF theory doesn't include spin-spin correlation, and hence ignores fluctuation altogether, while RPA introduces some corrections to that, it is only valid when the equal-time fluctuations are uncorrelated. Thus when the correlation length diverges near the critical field and the spin fluctuation becomes very strong, the MF calculated results deviate from the reality the most. For the imaginary part of the susceptibility on the other hand, the calculated values are again off by nearly an order of magnitude like before and neither capture the shapes of the experimental data. It is noted however, that the dip in the experimental data coincides with the predicted critical field, and deepens as the temperature rises. This offers another potential explanation to the observation: instead of viewing the double peaks as results of weakly interacting modes surrounding critical point hybridizing with the cavity mode, it is rather a dip at the quantum critical point in a broad "hump". However, due to a lack of further evidence and quantitative argument, the author refrains from postulating about the mechanism behind it and leaves the resolution to future work.

To further test the strength and weakness of our model, we repeat the same measurement with rotated transverse field on a much larger sample. The setup is shown along with the experimental results in figure 5.6. In this setup, in order to minimize uncertainties in the rotation angle, the inner cone and the cavity are machined as one piece (left panel of figure 5.6(c)). The side of the inner cone, on which the sample is attached along the ac-plane, was precision machined to lie at 45° with respect to the bottom of the cavity as seen in the technical drawing of the cavity in the right panel of fig. 5.6(c). Since the external magnetic field is applied perpendicular to the bottom of the cavity resonator as indicated by the black arrow in the actual photo of the cavity-LiHoF<sub>4</sub> setup in fig. 5.6(d), the field is now rotated by 45° within LiHoF<sub>4</sub> 's ab-plane. Furthermore, the volume ratio between the

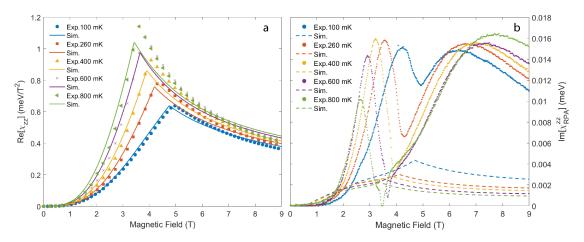


Figure 5.5: (a) The real part of the AC magnetic susceptibility of LiHoF<sub>4</sub> obtained from numerical fit to the experimental data (markers) and the MFT calculations (solid lines). (b) The same as (a) for the imaginary part of the susceptibility from experiments (dots) and calculations (dashed lines). Both figures share the same color code.

present sample and that in fig. 5.3 (as well as fig. 5.2) is  $\sim$  5.8, and we again modeled for the filling factor using FEM, which yield a value of, not 5.8 times bigger than that of fig. 5.2, but rather only 1.96 times bigger. This is primarily due to the inhomogeneity of the magnetic flux density in the cavity shown in fig. 4.1.

Taken into consideration of both the field rotation angle and the new filling factor, the resonance frequency is calculated and plotted in solid red line in figure 5.6(a) on top of the experimental data, and it is found that the best agreement between the two is reached when a tiny angle of  $0.05^{\circ}$  between the magnetic field direction and ab-plane is introduced, which necessarily introduces an extremely weak longitudinal field. We attribute this potential misalignment to human error when mounting the sample, in spite of which the result lends some further support to our model. In addition, MF-RPA calculated resonance frequency is also plotted in figure 5.6(a) using a red dashed line, and once again the calculation based on single-ion susceptibility agrees far better with the experiment than the result based on RPA susceptibility.

Subsequently, we present in figure 5.7(a) a  $\chi_{zz}^{MF}$ -based-simulation of  $|S_{11}|$  seen in figure 5.6(a). In addition, susceptibilities fitted from the experimental data as well as MFT calculated values are compared in 5.7(b). The two sets of values are again in good agreement with each other for the real part of susceptibility but not for the imaginary part. Moreover, two important features are noted to differ from previous cases. The first is that the discrepancy in  $\text{Im}[\chi_{zz}]$  between experimental and theoretical results is no longer as

large as orders of magnitude and is only limited to near the QCP. The second is the disappearance of the double peak surrounding the QCP. Given the small yet finite longitudinal field and previous observations in figure 5.4, it is reasonable to conjecture that the two features are related and due to the already weak hybridization between the cavity mode and the unspecified background mode being suppressed by the small longitudinal field. However, we emphasize again that the exact reason and mechanism is not known and more experimental investigation is required for any meaningful further discussion.

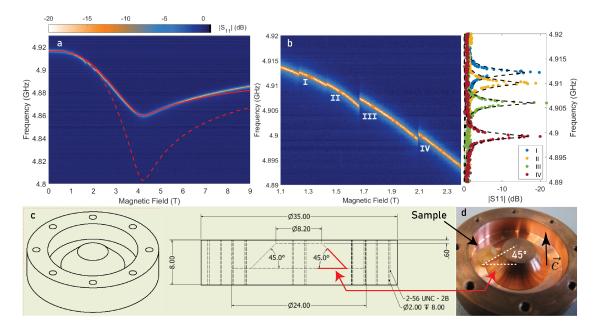


Figure 5.6: (a) Color map: experimental data of  $|S_{11}|$  as a function of magnetic field and frequency at 150 mK. Red solid line: cavity resonance frequency at the experimental condition obtained from MFT calculations with the inclusion of a longitudinal field that is only < 0.1% in amplitude of the transverse field. Red dashed line: cavity resonance frequency from the MF-RPA calculation (with the same parameters for the MFT calculation). (b) Left panel: expanded view of the small features present in the raw data in (a) at fields between 1 and 2 T. Right panel: Individual  $|S_{11}|$  measurements at field locations marked in the left panel by the roman numerals. (c) Technical drawing of the re-entrant cavity used for the present particular measurement. (d) An actual photo of the cavity with the sample on which data shown in (a) is measured. The upward black arrow indicates the external magnetic field direction, and the annotated white dashed lines show the angle between the crystallographic ac-plane and the normal plane to the external magnetic field.

A side note here is that new features appeared in the raw data upon increasing the sample size: a closer examination of the data at the low field region between 1 and 2 T reveals some disruption to the resonance frequency as shown in figure 5.6(a), which is clearly not present in our simulation in fig. 5.7(a). Carefully repeated measurements confirm

that these features were not from instrument fault or artifacts, and very sensitive to temperature changes. Upon discussions with authors of Ref. [45], the author takes the liberty and postulate that the origin of these features is likely a hybridization between the cavity mode and so called Walker's mode, or magnetostatics mode. However, sliced data given in the right panel of fig. 5.6(b) show no sign of branching, implying the potential line widths of these Walker modes are much finer than the experimental resolution of magnetic field. In light of the fact that these modes don't affect the discussion of the main focus of the present thesis, and only scarce amount of data are available, we refrain from digressing into discussing them further and leave the issue for future development.

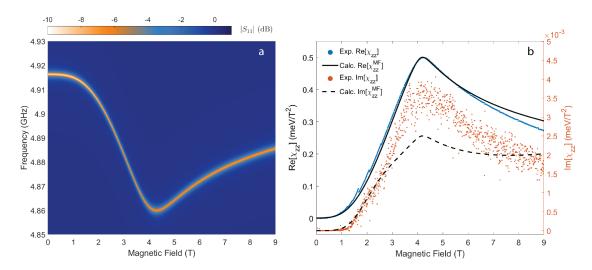


Figure 5.7: (a) Simulated  $|S_{11}|$  using the single-ion susceptibility under the same experimental conditions as those for the measurement shown in fig. 5.6(a). (b) Fitted values for the real (blue dots) and imaginary (red dots) parts of the AC susceptibility from the measurement shown in fig. 5.6(a). Black lines: The real (solid line) and imaginary (dashed line) parts of the single-ion susceptibility of LiHoF<sub>4</sub> (along the quantization axis) calculated by the MFT

#### 5.1.2 Field-Ramping measurement ( $\sim 2 \text{ GHz}$ )

In complement to off-resonance measurements in the previous section, a series of experiments was also carried out at a frequency (~ 2.2 GHz) below the single-ion excitation modes predicted by MFT, but will intercept the collective mode around the QCP according to calculations under MF-RPA as is shown in figure 5.1. Incidentally, this is also the frequency at which the authors of Ref. [45] chose to detect the RPA predicted soft mode.

The experimentally measured  $|S_{11}|$  is as usual presented as a color map in figure 5.8(a),

and again we see the trace of the resonance frequency taking on a familiar line shape as a function of the magnetic field. As with the previous case, we had to correct for the filling factor (the same value for both MF and MF-RPA calculations), but since it is of no relevance to the current discussion we omit it to avoid confusion and instead show only corrected results. In figure 5.8(a), plotted on top of the experimental data are two sets of MF results with different spin line widths ( $\gamma$ ). While the solid red curve was obtained with  $\gamma$  set to  $9\times 10^{-5}$  meV (21.7 MHz) as before, the dashed curve was calculated using  $\gamma=9\times 10^{-2}$  meV (21.7 GHz). It is obvious from the direct inspection that the latter theoretical result drastically deviates from the experimental values, and the discrepancies cannot be eliminated by simple scaling. On the contrary, the results from  $\gamma=9\times 10^{-2}$  meV achieved an excellent agreement with the experiment across the entire field range. Furthermore, to achieve such a degree of agreement, a longitudinal field of 0.1%, or equivalently a tilting angle of 0.05° out of crystallographic ab-plane, had to be introduced. This angle, despite being tiny in value, translates to visible and consequential changes to the eventual result of  $|S_{11}|$ .

The same comparison between two values of  $\gamma$  is also done with the MF-RPA calculations, and the resulting resonance frequencies are presented in figure 5.8(b). Since the MF-RPA calculation predicts a soft mode that traverses through this frequency and field window, unlike the previous case with the MF calculations, we expect it to directly hybridize with the cavity mode. This is indeed the case, and is more apparent for when  $\gamma = 9 \times 10^{-5}$  meV as shown in the inset of figure 5.8(b), where the color map is the calculated  $|S_{11}|$ , and the two white dotted lines are the predicted soft modes. In the present example, a small spin excitation line width (along with a small cavity line width) produces a higher cooperativity that contributes to the formation of an avoid-crossing-pattern[66, 33, 37]. Upon increasing the spin line width, the avoid-crossing-pattern eventually goes away even though the two modes still cross paths. This is precisely the case for the RPA results represented by the white dashed line in the main frame of figure 5.8(b). Furthermore, the line shape now resembles that of the MF result with  $\gamma = 9 \times 10^{-5}$  meV, and exhibits vastly different behavior from the experimental results. The author would also like to note that, this line shape shown by the RPA results (white dashed line in figure 5.8(b)) is consistent with what is given in Ref. [49] (fig. 2(b) & fig. 5(c)).

Since the discrepancy in  $|S_{11}|$  eventually boils down to that in the AC susceptibilities between experimental and theoretical results, we compare as before directly the theoretically calculated and the experimentally fitted values of  $\chi_{zz}$  in figure 5.8(c). All numerical results

shown in this figure are done by calculations with  $\gamma=9\times10^{-2}$  meV, and we see that, in accordance with figure 5.8(a), the MF results (red solid line) for the real part of the susceptibility again agree very well with fitted values from experiments (blue markers for the real part and red markers for the imaginary part). Moreover, the imaginary part of the MF susceptibility (red dashed line) is within the same order of magnitude of the experimental data (red solid markers), and exhibits qualitatively the same overall trend, despite not being able to capture the double peaks surrounding the QCP as in previous cases. In the inset, we provide an expanded view on the imaginary part of the susceptibility in order to show the double peak feature that is now drown out by the noise but still discernible. The black curve in the figure is intended for visual guide only. The elevated noise level found here may be an impact from a change of coupling conditions between the cavity and the antenna.

In contrast, values for the AC susceptibility obtained from RPA calculations are strongly peaked at the QCP and in poor agreement with the experiment. The contrast between these two results once again indicate the necessity to go beyond MF-RPA on the theoretical front. To reiterate, as postulated by the authors of Ref. [45, 49], the difficulty of RPA in describing experimental observations for the present case (or similar experimental schemes) may be the result of a short coherence time of the soft mode, which causes the collective mode to quickly decay into the single-ion mode, giving the latter substantially more weight in contribution to the eventual effect after integration over the time. Hence the more suitable model to use for CW measurements is always the MFT in the frequency domain. Furthermore, if we assume that, for the specific example of figure 5.8, the good agreement between the MF result based on a  $\gamma = 9 \times 10^{-2}$  meV and the experimental one is not coincidental, and we recall the fact established previously that, when the cavity is far enough off-resonance from the spin excitation modes, it is insensitive to the spin line width, then it implies that the present cavity resonance frequency may be sensing, but not direct hybridizing to, a magnon mode that is much closer in proximity than what the MFT predicted (see figure 5.1). Thus in a combined view, one necessarily has to go beyond MF-RPA, that will actually change the eigen-states and eigen-energies, in order to obtain a more satisfying description of the physics involved in these experiments.

To verify from a different angle that the predicted sharp peak of susceptibility is missing from experiment, we compare the present set of numerically fitted susceptibility from experiments at  $\sim 2$  GHz to those at  $\sim 5$  GHz at the same temperature in figure 5.8(d), where the blue and black dots represent the experimental values of the real part of susceptibility

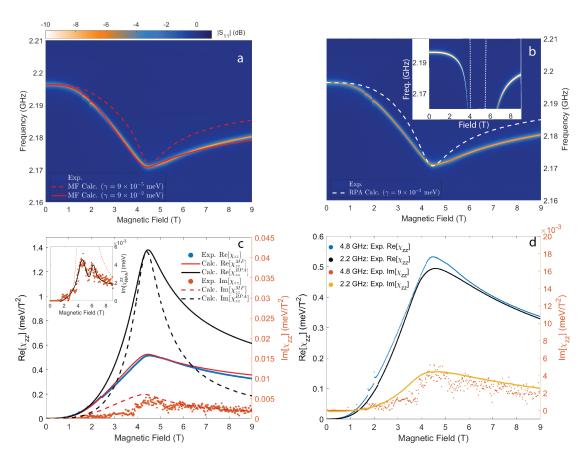


Figure 5.8: (a) Color map: experimentally measured  $|S_{11}|$  as a function of magnetic field and frequency at 150 mK between 2.10 GHz and 2.21 GHz. Red dashed line: MFT calculation of cavity resonance frequency as a function of magnetic field based on  $\gamma=9\times10^{-5}$  meV. Red solid line: MFT calculation of cavity resonance frequency based on  $\gamma=9\times10^{-2}$  meV. (b) Color map: experimentally measured  $|S_{11}|$ . White dashed line: MF-RPA calculation of cavity resonance frequency based on  $\gamma=9\times10^{-2}$  meV. Inset: MF-RPA simulated  $|S_{11}|$  based on  $\gamma=9\times10^{-5}$  meV, the white dotted lines are the soft mode predicted by RPA. (c) Fitted values of  $\chi_{zz}$  in real (solid blue markers) and imaginary (solid red markers) parts from experimental data given in (a). Solid lines: calculated values for the real (solid lines) and imaginary (dashed lines) part of susceptibility from MFT (red) and MF-RPA (black). (d) Comparison of fitted values for AC susceptibilities in real and imaginary parts from experiments carried out at  $\sim 4.8$  GHz and  $\sim 2.2$  GHz.

from 4.8 GHz and 2.2 GHz experiments respectively, and the red and yellow dots are the imaginary parts of those measurements. The two sets of data on the real part of susceptibilities agree very well throughout the field range, with the exception of the peak sharpness that has been shown to be related to the longitudinal field. The imaginary part of susceptibility also agree with each other rather well in terms of both the amplitudes and the general line shapes. This comparison indicates that there may be no qualitative

differences in the off-resonance susceptibility between the two frequency windows (one above and one below the spin excitation modes inside the electronic ground state manifold), and hence provides further evidence that the current theoretical description at the lower energy scale calls for further considerations.

As we have seen that, in spite of the double peak in the imaginary part of the susceptibility surrounding the QCP is still visible in the inset of figure 5.8(c), the increased noise level begin to mask any potential features, rendering it difficult to pinpoint the spin excitation modes underneath if there is any. To amend the issue, we recall that the quality factor (Q) is also a measure of dissipation rates. we can therefore make use of the inverse of Q-factors to keep track of any potential "leaky channels" coupled to the cavity mode as in Ref. [41] and Ref. [45].

To that end, we use the usual definition of quality factor:  $Q = \omega_0/\Delta\omega$ , where  $\omega_0$  is the resonance frequency of the resonating structure, and  $\Delta\omega$  is the spectral bandwidth of resonant peak. The inverse of thus measured Q from experimental data are then plotted using solid markers in figure 5.9(d), in a series of data sets taken at different temperatures.

The most striking features of these 1/Q measurements are the presence of two peaks surrounding the critical field at each temperature. Furthermore, the peaks above the critical fields, when the sample is expected to be in the (polarized) paramagnetic state, have much sharper profile than those below the critical fields when the sample is in ferromagnetic state. Moreover, As the temperature is raised, the critical field shifts lower, and so do the two peaks surrounding it. More importantly, the peak amplitudes also go down with raised temperatures, while at the same time don't exhibit obvious broadening. These observations thus appear to suggest lower dissipation rates for higher temperatures at the location of these two peaks. This is quite counter-intuitive, since we assume they are caused by mode hybridizing with the spin system, and a higher temperature usually tends to shorten the spin lifetime and consequently broaden the corresponding absorption peak, contrary to what we are seeing here.

In order to compare to calculations and make physical sense of these peaks, we turn to MF-RPA calculations to obtain soft modes as functions of the magnetic field, and then compute for the field locations of expected crossing points between these modes and the cavity mode. Examples at 150 mK and 280 mK are given in figure 5.9(a, b), where experimental data are given as color maps as before, plotted on top of which are pairs of white dashed lines that represent the soft modes from calculations. It is clear from these two figures that

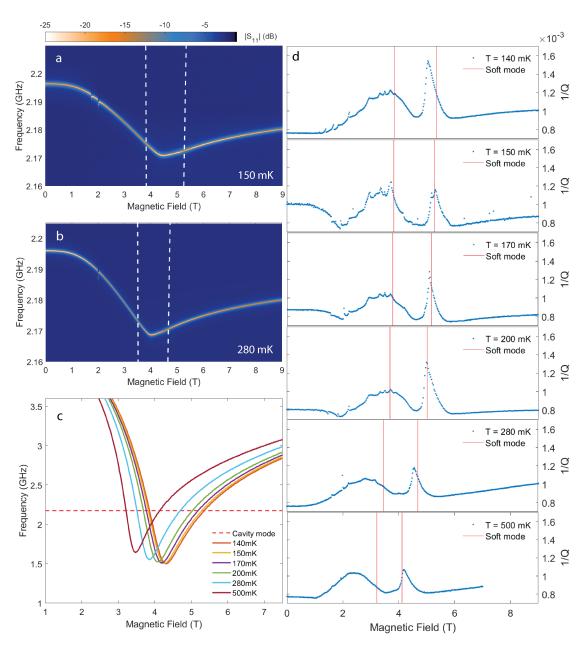


Figure 5.9: Color map: experimentally measured  $|S_{11}|$  as a function of magnetic field and frequency at 150 mK (a) and 280 mK (b) between 2.10 GHz and 2.21 GHz. White dashed line: MF-RPA predicted soft mode in LiHoF<sub>4</sub>. (c) Estimates of crossing points between the cavity mode (red dashed line) and MF-RPA predicted soft modes (solid lines) at various temperatures. (d) Temperature series of the inverse of quality factors (Q) as functions of magnetic field, obtained from experimental results at ~ 2.2 GHz. The red vertical lines indicate the locations on the field axis of the corresponding crossing points with the MF-RPA predicted soft mode.

within the given frequency window, they are nearly vertical. Consequently, one need not to take into consideration of the bending of the cavity resonance frequencies at different field when estimating for the crossing points between them and the soft modes. Subsequently, we carry out this estimate for all temperatures listed in Fig. 5.9(d) and summarize it in figure 5.9(c), where the cavity mode now is simply represented by a straight line (red dashed line).

The crossing points are then translated into red solid vertical lines in figure 5.9(d) in order to compare their field locations with those of the peaks in the 1/Q measurement. We see the two in fact do agree with each other rather well across a wide temperature range, with a worsening of agreement toward higher temperatures. In addition, there is a minor but notable difference in the agreement with calculations between the case at 140 mK and the one at 150 mK. However, this is potentially explained by the inaccuracy of temperature measurement, considering that all other measurements follow a consistent pattern. If this is true, then the actual temperature of the sample in the first panel of figure 5.9(d) is likely slightly higher than the reading (at  $\sim 170$  mK).

Thus it indeed appears that we are detecting the RPA predicted soft mode using peaks in the experimentally measured 1/Q data, consistent with previous studies[45, 49]. However, the author would like to remark that the evidence provided here is more qualitative than quantitative, and taking into considerations of the inadequacy of RPA in capturing other aspects of the experimental observation as the present report has already outlined, more definitive experimental evidence as well as quantitative comparisons to theoretical predictions are imperative. Furthermore, as the authors of Ref. [49] have already noted that CW measurement scheme may be inherently unsuitable for the detection of the expected soft mode in LiHoF<sub>4</sub> due to its extremely fragile collectiveness. Therefore, it is likely that a more quantitative measurement on the collective soft mode can only be obtained through other experimental schemes in the time domain.

#### 5.1.3 Temperature-Ramping Measurement (~5 GHz)

Since the inflection point in the trace of resonance frequencies, or equivalently the peak position of the real part of susceptibility, gives away the critical field, a phase diagram can thus be constructed by recording the field position of this cusp at various temperatures. However, this method fails at higher temperatures near 1.5 K when the phase boundary takes on a much steeper slope along the field axis, which is evident from previously reported data (solid red circles) in figure 5.11(c). This creates difficulties for reliably pinpointing

critical points from field-sweeping measurements at fixed temperatures.

The problem is more evident by examining data taken at 1.48 K, 1.66 K, 1.92 K and 4.27 K shown in figure 5.10, all of which were taken on the same sample in a cavity whose resonant frequency is 4.755 GHz. In the left panels of figure 5.10(a-d), the 3D raw data of  $|S_{11}|$  are given in color plots as before, whereas the right panels provide examples of fitted data (the black dashed lines are fits and the colored markers are experimental data) at three selected magnetic fields (the field locations are marked by both the white dashed lines and the arrows in the left panels). The fitted real and imaginary parts of susceptibilities are given in figure 5.10(e-h) in the corresponding order. Although the temperatures of these four sets of data spread across a wide range that encloses the known zero-field critical temperature[9, 61], there is virtually no difference in the collected data to differentiate the ferromagnetic and paramagnetic phases. This is particularly the case when contrasting data taken at 1.48 K and 1.66 K, despite of being on opposite sides of the critical temperature (1.53 K)[9], there are neither obvious changes to the features in the color plot (fig. 5.10(a, c)), nor substantial differences in the fitted susceptibilities (fig. 5.10(b, d)). Moreover, in a wide field range between 0.5 T and 2.5 T, the measured  $|S_{11}|$ peaks become too broad and shallow to be used for the search of inflection points along the trace of resonance frequencies.

We make a remark here regarding the broadened peaks of measured  $|S_{11}|$  in figure 5.10(a-d): the broadening is entirely possible due to strong damping resulting from changes of coupling conditions between the cavity system and the transmission line, which itself is potentially caused by changes in the permeability of LiHoF<sub>4</sub> when the magnetic field is swept. However, since an increased amplitude of the imaginary part of AC susceptibility, such as those in figure 5.10(e-h), implies an elevated dissipation rate, or photon loss rate, there is another possible explanation to the broadened peaks, which is weak mode hybridization between the LiHoF<sub>4</sub> sample and the cavity photon field. Given that the peak positions in the imaginary parts of the susceptibility at temperatures below and above the critical temperature don't appear to differ from each other, it necessarily implies an excitation mode that persists through the phase transition, which is unusual and in itself an interesting topic. The intuitive approach is to compare experimental data to calculations, but since MF is known to overestimate the critical temperature and completely ignore fluctuations, it prevents us from comparing the two in a meaningful way. We therefore only stress the potential importance here and leave the issue for future investigations.

As a consequence of this inability to discern the critical points from field-sweeping data

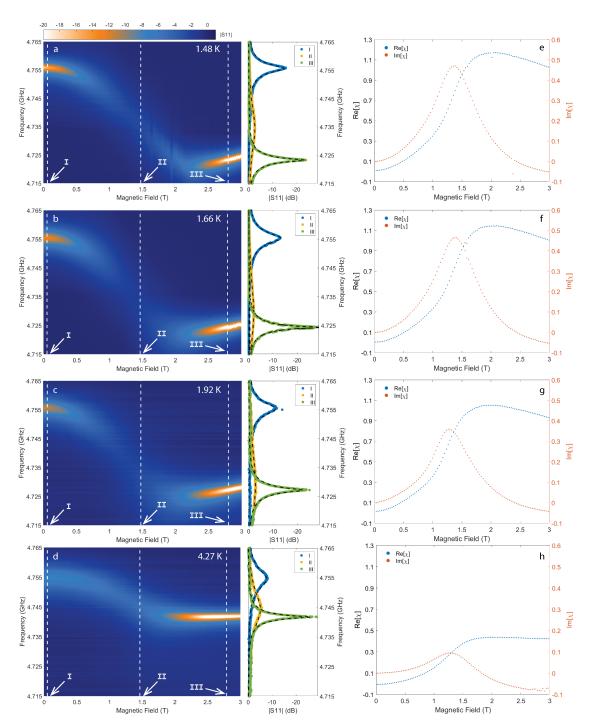


Figure 5.10: (a-d) Left panels: Experimental results of  $|S_{11}|$  as functions of magnetic field and frequency at 1.48 K, 1.66 K, 1.92 K, and 4.27 K, obtained from Field-Ramping measurements. Right panels: Individual measurements (markers) at selected external magnetic field locations marked by the white arrows and roman numerals in the left panels. Black dashed lines: corresponding numerical fits to the data using Eq. 2.38. All color plots share the same color scale displayed above (a). (e-h) Fitted real (blue dots) and imaginary parts (red dots) of the AC magnetic susceptibilities of LiHoF<sub>4</sub> from measurements shown in (a-d) in corresponding order.

at high temperatures, we resort to temperature-sweeping measurements at constant magnetic field for this region of the phase space. Figure 5.11(a) shows, again in the left panel, raw data taken at zero magnetic field and, in the right panel, fits to individual measurements at selected temperatures. An immediate observation from figure 5.11(a) is that the  $|S_{11}|$  peak position remains more or less constant along the temperature axis, whereas its width and depth change dramatically. The first observation is quantified in figure 5.11(b) by extracting the resonance frequencies through numerical fits. The second observation is presented using both the imaginary part of sample susceptibility from the same fit routine as a function of temperature (blue dots) as well as the inverse of quality factor (Q) of the CMP system (red dots), defined by the ratio between its bandwidth and its resonant frequency in figure 5.11(c). All three variables show drastic changes of curvatures at the same temperature, which is taken as the critical temperature.

By complementing field-sweeping data at low temperatures with temperature-sweeping measurements near the zero-field-critical-temperature, we map out the magnetic phase diagram of LiHoF $_4$  and present it in figure 5.11(d), where the constructed phase diagram is given in two parts: the solid blue triangle markers are from temperature-sweeping measurements while the solid circles of matching color are from field-sweeping data. We also plotted previous experimental results from Ref. [9] in solid red circles for comparisons, and within the entire phase space considered, the two agree reasonably well with only small discrepancies, which may be a result of small misalignment of crystal orientation in relation to the external magnetic field (see fig. 3.16). Furthermore, in order to test the reproducibility of the measurement, we repeated the measurements on another sample of identical geometry and orientation. The result is represented by the solid black squares in the same figure and is in excellent agreement with the other set of data.

We note that the experimentally measured phase boundary near the zero-field critical-temperature (blue triangles in figure 5.11(d)) appears to "zig-zag" along the vertical axis. All temperature-sweep data used for the phase diagram mapping have clear inflection points as those shown in figure 5.11(b,c). Despite the presence of fluctuations of data points around the mean, they are not enough to account for the significant shift along the temperature axis of the phase diagram shown in 5.11(d). According to the experimental data, the phase boundary indeed shows re-entrance features in this region, which is consistent with the previous report[63] and raises unanswered interesting questions. However, due to the limited availability of experimental data and the inadequacy of MF and RPA models near critical temperatures, we will leave the study of underlying

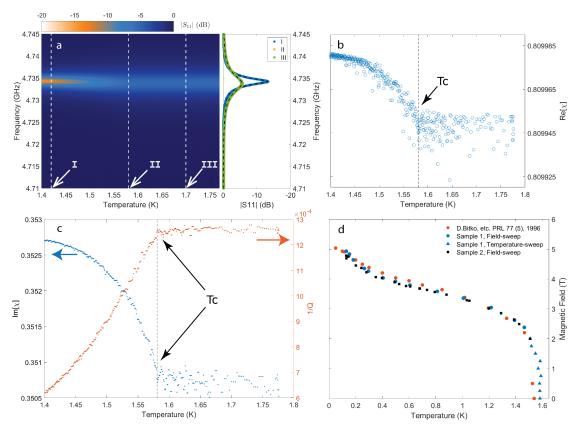


Figure 5.11: (a) Left panel: Measurement of  $|S_{11}|$  as a function of temperature and frequency at zero magnetic field. Right panel: Individual measurements (markers) at selected external magnetic field given by the arrows and roman numerals in the left panel. Black dashed lines are numerical fits to the data using Eq. 2.38. (b) The real part of the AC magnetic susceptibility of LiHoF<sub>4</sub> obtained from fitting to experimental data shown in (a). (c) Fitted imaginary part of the susceptibility (blue dots) and the inverse of quality factors (red dots). (d) Magnetic phase diagram of LiHoF<sub>4</sub> constructed in the present experiment (blue solid circles, triangles, and black solid squares) and that from a previous literature (red solid circles)[9].

mechanism for future effort.

### 5.2 On-Resonance Results and Analysis

As per its definition, the cavity resonance frequency during an on-resonance measurement matches at least one of the energy gaps between spin states, and thus it allows for coherent exchange of energy quanta between the spin ensemble and cavity photon field. The choices of cavity resonance frequency were previously given in figure 5.1. Based on both the MF and MF-RPA excitation spectra, we expect on-resonance hybridization at multiple points

along the field axis across the QCP. However, due to the failure of RPA results previously shown, we will focus primarily on analysis based on MF calculations, but will provide a brief comparison to RPA results toward the end of the chapter.

#### 5.2.1 Low Power Excitation

The raw data of experimentally measured  $|S_{11}|$  at 150 mK is shown in figure 5.12(a) as a function of magnetic field and frequency. Apart from the now familiar QPT induced cusp in the resonant frequency that is marked by the white arrow in the same panel, multiple new features that weren't present in off-resonance data emerged. The white dashed boxes single out some of these features, the zoomed-in images are given in panel (c), (d), and (e) respectively with adjusted color scales. In addition to these local features, near 12 T (inside the box III in fig. 5.12(a)), the cavity resonance peak becomes extremely broad, implying a strong damping effect.

It is known that when two modes hybridize strongly enough the collective mode splits in two and the phenomenon is described as "level repulsion". This is both well recorded in the literature [35, 66, 57], and consistent with what we found in figure 2.5 in Chpt. 2. In fig. 5.12, two of such avoid-crossing-patterns are clearly visible and are located at  $\sim 3.3$  T and 13.4 T on the opposite side of the critical field. These two regions are blown up in panel (c) and (e) for closer inspection with a slice of data shown in the right panels at magnetic field indicated by the white dashed lines in the left panels. In both cases, we see clear patterns of mode branching where a single cavity resonance mode branches into two. The distance between the two peaks when they are roughly equal heights give an estimate of twice the coupling strength between the spin excitation mode and cavity mode[30, 67]. In fig. 5.12(c), this coupling strength is measured to be 54 MHz, and in fig. 5.12(e), it is 42 MHz.

Apart from these strong coupling features, five weak coupling features are also visible to varying degrees between 5 T and 14 T, where the cavity mode shows no branching effect throughout the region. An example of these features is isolated and shown in fig. 5.12(d), and even the data slice at exactly the field when the spin excitation mode and cavity mode are expected to coincide has a single peak. However, from the color map, a discontinuity of the cavity resonance frequency takes place and is accompanied by a broadening of the peak.

In order to extract the resonance frequencies, spin line width, and coupling strength, the experimental data in close vicinity of these features are fitted. Unlike in the off-resonance

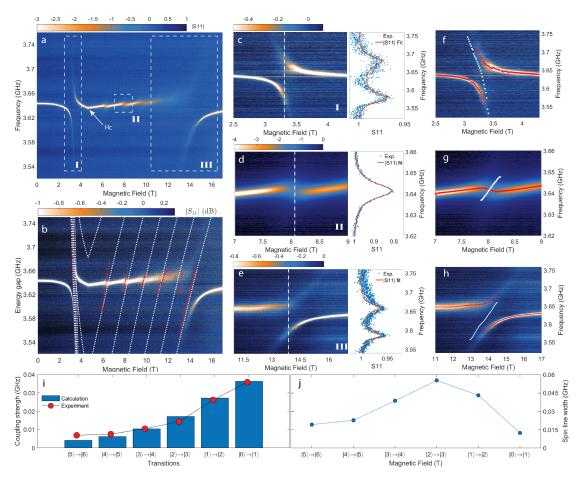


Figure 5.12: Color plots in (a-h) are the same experimentally measured  $|S_{11}|$  in parts (c-h) or in whole (a, b) as a function of magnetic field and frequency on a single crystal sample of LiHoF<sub>4</sub> at 150 mK in a reentrant cavity with a resonant frequency at 3.63 GHz. (b) White dotted lines: calculated  $\delta I^z=1$  excitation spectra within the electronic ground state manifold. Red dots: Numerically fitted values for the spin excitation modes. (c-e) Expanded views with adjusted color scales of regions enclosed by white dashed boxes in (a). The roman numerals indicate the correspondence. (f-h) The fitted values for the resonance frequencies (red dots) of the spin-cavity ensemble and the electro-nuclear spin excitation spectra (white dots) plotted on top of the experimental data also shown in (c-e) in the corresponding order. (i) The coupling strength between the cavity mode and  $\delta I^z=1$  excitation modes in LiHoF<sub>4</sub> obtained from MF calculations (blue bars) and fits to the experimental data (Solid red markers). (j) Excitation linewidth from numerical fits to the experimental data.

case, the AC susceptibility can no longer be treated as frequency independent. Instead,

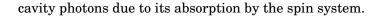
the susceptibilities are again split into parts, the explicit function reads:

$$|S_{11}| = \left| 1 + \frac{2\kappa_e}{i(\omega - \omega_c) - (\kappa_e + \kappa_i) + \chi_{\text{off}} + \frac{\tilde{G}^2}{i(\omega - \Omega_0) - \gamma_0}} \right|$$
 (5.1)

where  $\omega_c$  is the bare cavity resonance frequency,  $\chi_{\rm off}$  contains contributions from all the locally off-resonance spin modes and is assumed to be frequency independent. In contrast,  $\Omega_0$  is the spin excitation mode that is locally on-resonance with the cavity mode, and  $\tilde{G}^2 = |\tilde{g}(\omega_c)|^2 \sum_{i,f} \langle i|\tilde{\mu}_{k_c}^z|f\rangle \langle f|\tilde{\mu}_{-k_c}^z|i\rangle \langle f-P_f\rangle$  characterizes the coupling strength between the two modes. Recalling from the previous text,  $\kappa_e$  and  $\kappa_i$  are again the external and internal dissipation rates of the cavity and  $\omega$  represents the frequency as the variable. Here, in comparison to Eq. 2.37, we assumed that there is only one on-resonance mode and isolated it from the rest, hence reducing the number of necessary fitting parameters.

This fitting approach is entirely justified for data of LiHoF<sub>4</sub> in the paramagnetic state according to our MF calculations. In fig. 5.12(b), a series of white dotted lines on top of the experimental data is used to represent the spin excitation modes in LiHoF<sub>4</sub>, and we can see the modes are well separated along the field axis above the critical field near 5 T. Conversely, in the ferromagnetic state, these excitation modes appear to be in a close bundle but not entirely degenerate according to MF predictions. However, recalling that these modes are  $\delta I^z = 1$  excitations and thus only one of them starts from the ground state, it is safe to assume that, at very low temperature in mK range and with comparable  $exp(\beta\Delta E(\delta I^z))$  among the modes, the excitation mode originating from the ground state will dominate simply due to its high occupation number. Therefore, to a good approximation, we can fit the experimental data assuming only one spin mode hybridizing with the cavity mode locally.

Part of the numerical fits to experimental data shown in figure 5.12(c, d, e) are respectively given in figure 5.12(f, g, h), where the fitted values are plotted on top of the experimental data. The red dots are fitted collective modes of cavity-LiHoF<sub>4</sub> system, and the white dots represent the local on-resonance spin excitation mode. Fit results to the slices of data given in the right panels of figure 5.12(c, d, e) are also shown in the same panels to provide a visual confirmation of the goodness of fit. These results provide some insights into the new features that emerged in the on-resonance data. Apart from the expected branching due to strong hybridization with the spin mode, the shifts that cavity mode exhibits in the weak coupling regime are also a direct consequence of mode coupling. A temporarily broadened resonant peak at the location of mode hybridizing tokens an increase of dissipation of



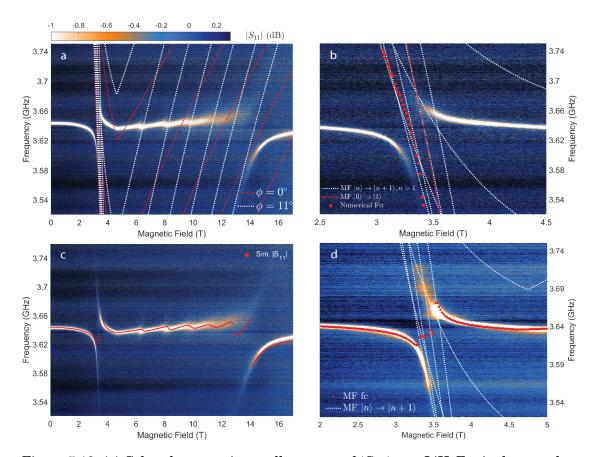


Figure 5.13: (a) Color plot: experimentally measured  $|S_{11}|$  on a LiHoF<sub>4</sub> single crystal at 150 mK. Dotted lines:  $\delta I^z=1$  excitation spectra within the electronic ground state, with an angle of 0° (red dashed lines) and 11° (white dashed lines) between the transverse field and the crystallographic a-axis within the ab-plane. (b) Expanded view of (a) at the anticrossing below the QCP. Dotted lines: MF excitation spectra of  $\delta I^z=1$ . The red dashed line highlights the fundamental mode of the spectrum. Red solid circles: single-ion excitation mode according to numerical fit to the experimental data. (c) Comparison between the MFT calculation of the resonance frequency of the spin-cavity ensemble (red dots) and the experimental data (color plot). (d) Expanded view of (c) below the critical field.

In figure 5.12(b), we compare MF calculated  $\delta I^z=1$  eigen-modes (white dotted lines) to fitted values (red solid markers), a reasonably good agreement is seen across the entire field range with some exceptions. It is found that these discrepancies in terms of field locations at which mode hybridization happen cannot be reconciled by simple scaling, demonstrating an aspect of inadequacy of the mean field approach in the present context and need for more sophisticated theory. Moreover, in order to achieve the shown agreement, a small in-plane rotation of  $\phi=1.0^{\circ}$  of the magnetic field within ab-plane is imperative,

which is demonstrated in fig. 5.13(a), where the  $\delta I^z=1$  spin excitation spectra from MF calculations with (white dotted lines) and without (red dotted lines) such a rotation are shown together on top of the experimental data for a visual comparison. Furthermore, though the assumed degenerate spin mode below the critical point indeed appears to follow the bundled spin excitation spectra predicted by MF calculations, a closer inspection of zoomed in figure of this region shown in figure 5.13(b) reveal some important discrepancies. In fig. 5.13(b), the solid red circles represent fitted spin excitation spectrum, and the dashed lines are those from MF calculations. Among the calculated spectra, the excitation mode originating from the ground state is specially highlighted in red for comparison to fitted results since we expect this mode to dominate the contribution. Though the two sets of values follow each other closely, the curvature/slope appear to disagree.

There is another way of testing the adequacy of our approximation of treating these closely bundled transitions as a single excitation mode. As we can see in fig. 5.13 (b, d) that, the coupling strengths between the cavity and the electro-nuclear excitation modes are of the order of 50 MHz, while these modes themselves are of the order of 3.6 GHz, which is much bigger than the former. Consequently, we are allowed to employ the second order perturbation theory to fit these two branching modes in close proximity in order to obtain the underlying spin excitation mode. To do so, we also assume the spin excitation spectra are locally linear functions of magnetic field, which is reasonable according to MF calculations. A brief description of the fit is given as following:

Denote the creation and annihilation operators for the cavity photon field by  $\hat{a}^{\dagger}$  and  $\hat{a}$ , then similarly denote those for the single magnon mode by  $\hat{m}^{\dagger}$  and  $\hat{m}$ , thus we construct a Hamiltonian that hybridizes them at a real valued coupling strength of g:

$$\hat{\mathcal{H}} = \hbar \omega_a \hat{a}^{\dagger} \hat{a} + \hbar \omega_m \hat{m}^{\dagger} \hat{m} + g(\hat{a}^{\dagger} \hat{m} + \hat{a} \hat{m}^{\dagger}) \tag{5.2}$$

Hence this is a two-level system, and we use  $|g\rangle$  to label the ground state where there is a photon but no magnon, and  $|e\rangle$  to label the excited state where there is no photon but one magnon. Then by assuming there exists an eigen-state of the total hamiltonian denoted by  $|\psi\rangle$ , we have

$$\hat{\mathcal{H}}|\psi\rangle = \begin{pmatrix} \hbar\omega_{a} & g \\ g & \hbar\omega_{m} \end{pmatrix} \begin{pmatrix} |g\rangle\langle g|\psi\rangle \\ |e\rangle\langle e|\psi\rangle \end{pmatrix} = E|\psi\rangle \tag{5.3}$$

Following through the procedure of standard second order perturbation theory[31], we

arrive at the eigen-frequencies given by:

$$\omega_{\pm} = \omega_c + \frac{\omega_+ - \omega_-}{2} \pm \frac{\sqrt{(\omega_+ - \omega_-)^2 + 4(g/\hbar)^2}}{2}$$
 (5.4)

where  $\omega_c$  is the resonant frequency of bare cavity, and we used subscript + and – to indicate the upper and lower branch of the eigen-state at higher orders. Next we parametrize the magnon mode in the close vicinity of the anti-crossing (mode hybridization) as a linear function of magnetic field. Then, with the split expression (Eq. 5.4), we can fit separately the upper and lower branches, extracted from experimental data by simple minimum search algorithm, with the appropriate sign of slope and reiteratively until it converges. The results are presented in figure 5.14(a) and (b) respectively using blue dot-dashed lines. For comparison, we also plot in black dashed lines the MF result of the first order magnon mode originated from the electro-nuclear ground state. An excellent agreement in the higher field case (Fig. 5.14(b)) is reached, whereas that for the low field case (Fig. 5.14(a)) has considerable discrepancies. This again hints that the excitation modes in the ferromagnetic states are likely not fully degenerate.

Given the agreement between the MF prediction and the experimental data in figure 5.12, we can attribute each feature to a specific spin excitation mode. By denoting the electro-nuclear eigen-states with an ascending numeral  $|n\rangle$ , n=1,2,3,..., the six visible features starting from higher field near 14 T toward the critical field at 5 T correspond respectively to  $|0\rangle \rightarrow |1\rangle$ ,  $|1\rangle \rightarrow |2\rangle$ ,  $|2\rangle \rightarrow |3\rangle$ ,  $|3\rangle \rightarrow |4\rangle$ ,  $|4\rangle \rightarrow |5\rangle$ ,  $|5\rangle \rightarrow |6\rangle$ .

In addition to the spin resonance mode, the coupling strength as well as the spin line widths were also fitted from experimental data. In particular, the coupling strength, as seen in Eq. 5.1, can be computed under MF approximation. Therefore we plot both its experimental and calculated values in fig. 5.12(i) using solid markers and bars respectively, and the two agree with fitted values very well. At the same time, since we do not have a microscopic model for the spin lifetime in LiHoF<sub>4</sub>, we simply present the fitted values as it is in fig. 5.12(j). However, here we make a remark about the spin line width: since the transition line width between two states are affected by the lifetime of both states, the transition from the ground state should exhibit finer line width due to the infinitely long lifetime of ground state. This is indeed observed in Fig.5.12(i), but at the same time, the spin line width of the highest transition is also lower than others. We understand this by considering the stimulated absorption rate, which is increased when the cavity mode is on-resonance with the excitation mode, however, this rate is vanishingly small for the highest state of the manifold since the energy required for the next excitation lies far out

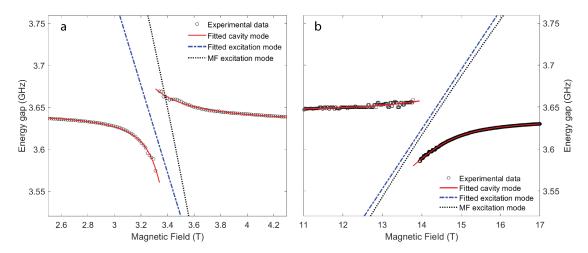


Figure 5.14: Fitting using second order perturbation theory of the anti-crossings found in the experimental data near 3.3 T (a) and 14 T (b). The open circles are cavity mode extracted from the experimental data, the red curves are that from numerical fitting. The blue dot-dashed lines are fitted spin excitation mode and the black dashed lines are those from MF calculations.

of the present cavity frequency, hence the lifetime of the top state is in comparison longer than it would have been for an intermediate state. Therefore, when stimulated emission and absorption rates dominate the decay rate, the excitation line width should always take a "bell" shape across a set of nearly equal distant states.

We repeated this fit routine at five different temperatures. Examples at the highest and lowest temperatures are given in figure 5.15(a, b), aligned by the field axis. Fitted values for the coupling strengths of the lowest six magnon modes and corresponding spin line widths are presented in figure 5.15(d, e). The calculated values of the coupling strength agree with the experimental values reasonably well at all five fitted temperatures. Some data points are missing due to a strong damping that prevented the author from carrying out the fit, examples of which are presented using the raw data between 8 and 12 T panel in figure 5.15(b), where the cavity resonant peaks are extremely broad, hindering meaningful extraction of physical parameters. The exact origin of this broadening is not known, but it is reflected in the excitation mode line width. In figure 5.15(e) we show the fitted spin line width in the similar fashion as in Fig.5.12(j) but for all five temperatures measured. Apart from the missing data points, the line width of the same excitation mode indeed appear to broaden with raised temperature, and we postulate this is related to stronger fluctuations by raised temperature, which results in inhomogeneous broadening owing to the long range interaction between spins.

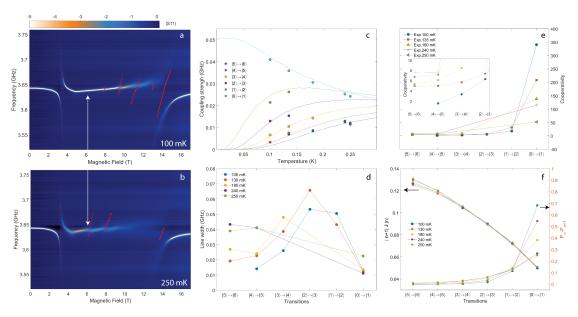


Figure 5.15: (a, b) Color plot: experimentally measured  $|S_{11}|$  at 100 mK and 240 mK. Red dots: Fitted magnon modes. White arrow: expected location of hybridization between the fundamental magnon mode ( $|0\rangle \rightarrow |1\rangle$ ) and the cavity mode. (c) Solid lines: Coupling strengths between the cavity mode and different magnon modes at, respectively, 100 mK, 130 mK, 180 mK, 240 mK, and 260 mK from MFT calculations. Solid markers: fitted values from experimental data for the coupling strengths between the cavity mode and magnon modes. (d) Numerically fitted values for the spectral line-width of different magnon modes at various temperatures, (e) Cooperativity of hybridized modes at various temperatures, calculated from the experimental data. Inset: expanded view of cooperativity for the higher magnon modes. (f) Calculated off-diagonal matrix element and population factor of the magnon modes at different temperatures. Color code is shared among (c-e) and indicate correspondence.

An ascending trend of the coupling strength toward lower excitation mode is evident from both calculations and experimental results for all data in the temperature series given in figure 5.15(c). The tendency is also most prominent at lower temperatures, which is best visualized in figure 5.12(i). Though according to linear response theory, both off-diagonal matrix element as well as population factor  $(P_{n+1}-P_n)$  contribute to the overall amplitude of coupling strength, based on MF calculations, the latter is primarily responsible for the ascending trend. We show in figure 5.15(f) both the population factors (squares on the right axis) as well as the off-diagonal matrix elements (circles on the left axis). Contrary to the ascending trend of the coupling strength for the lower modes, the lower states actually overlaps less with each other than the higher ones and this tendency barely changes with the temperature. However, the Boltzmann distribution dictates that more spins are at lower states and participate the coherent exchange of energies with the photon field, and it

is apparent that the population factor dominated in its product with the off-diagonal matrix element and determined their eventual weight in the mode hybridization. This changes slightly as the sample is warmed up when the higher states become more populated, resulting in an overall stronger coupling of these modes to the cavity mode. The described mechanism is directly manifested in the raw data when comparing figure 5.15(a) and figure 5.15(b) at locations pointed out by the white double arrow between these two figures, the hybridization between the cavity mode and excitation mode ( $|5\rangle \rightarrow |6\rangle$ ) is clearly visible in figure 5.15(b) at 240 mK, while being missing in figure 5.15(a) at 100 mK.

Another useful measure of coupling strength is a dimensionless ratio called cooperativity, which essentially measures the coupling strength against dissipation rates and is usually defined as  $C = G_{mn}^2/\gamma_{mn}(\kappa_e + \kappa_i)$ [66, 37, 29]. In figure 5.15(e) we plot the calculated cooperativity for different magnon modes at five temperatures using fitted values from experiments, where a trend of higher cooperativity for lower modes is obvious and consistent with the raw data. Furthermore, the cooperativity of the fundamental mode progressively lowers as the temperature rises, a tendency that also agrees with the raw data where a less severe branching accompanied by broader peaks is observed in figure 5.15(b) than (a). In the inset the cooperativity for higher modes clearly increases with the temperature, presumably due to an increase of population as in the previous analysis.

Now with fitted values of spin excitation line widths, we can again use the combination of Eq. 2.11, Eq. 2.15, and Eq. 2.37 to simulate  $|S_{11}|$  at experimental temperatures. For the missing values of the spin line width of specific modes, we use the value of its nearest neighbor as an approximation. As for all other excitation modes, since they are off-resonance and their line widths are thus less relevant, we therefore assume a value of  $9 \times 10^{-5}$  meV uniformly for all of them.

In the first row of figure 5.16(a-c) we show respectively  $|S_{11}|$  calculated from the single-ion susceptibility (a), RPA susceptibility (b) and the experimentally measured values (c). In the second row of panels, we show the corresponding susceptibilities between 1 and 5 GHz in figure 5.16(d, e). The biggest difference between the two susceptibilities is still the complete softening of the fundamental mode that is only predicted by the RPA. The resulting consequence in the relevant frequency window that is decided by the present set of experimental data (3.52 - 3.76 GHz) reveals that the crossing point between the cavity and soft mode is further to the right on the field axis comparing to that between the cavity mode and the single-ion fundamental mode. This is demonstrated in figure 5.16(f), where the horizontal line represents the cavity resonant frequency, and the two aforementioned

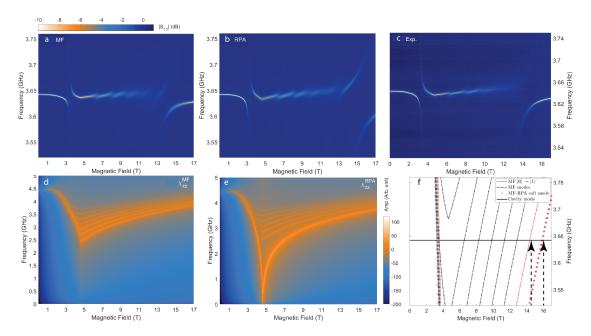


Figure 5.16: (a, b) Simulated  $|S_{11}|$  at 130 mK based on the single-ion susceptibility (a) and RPA susceptibility (b). (c) Experimentally measured  $|S_{11}|$  on a single crystal of LiHoF<sub>4</sub> in a re-entrance cavity at 130 mK. (d, e) The corresponding susceptibility used for  $|S_{11}|$  simulations in (a, b) respectively. (f) Dashing lines: the single-ion excitation spectra of  $\delta I^z=1$  within the electronic ground state manifold. The fundamental mode ( $|0\rangle \rightarrow |1\rangle$ ) is highlighted in red. Dotted line: The soft mode predicted by MF-RPA calculation at the same temperature.

crossing points are singled out by the black arrows in the figure, the distance between which is measured to be more than 1 T along the field axis. This is indeed reflected in the eventual simulation of  $|S_{11}|$  as seen by comparing the MF results in figure 5.16(a) to the RPA results in fig. 5.16(b), where the cavity line in the latter is pushed further toward the right end of the figure, in apparent contradiction to what is observed in the experimental data given in fig. 5.16(c). Comparatively, the MF results struck an excellent agreement with the measured data. Another relatively smaller feature is that, due to the stronger diverging behavior of the soft mode at the QCP, the cusp along the resonance frequency near 5 T is much more pronounced in fig. 5.16(b) than in fig. 5.16(a), and again the latter of which appears to be in a better agreement with the experimental data even by just visual inspection.

Thus we have shown again that the MF predictions appear to be more accurate without RPA corrections for the present measurement scheme. Prompted by this observation, we again proceed to simulate  $|S_{11}|$  using only MF susceptibilities at other temperatures. The

results are presented in in figure 5.17(d-e) in order to provide a side-by-side comparison to the experimental results (figure 5.17(a-c)). A good overall qualitative agreement is seen across different temperatures with the high field data at 250 mK displaying some visible discrepancies, presumably due to the inaccuracy of mode line widths as a result of missing fits for these modes. To better visualize the agreement, we also plot the calculated cavity resonance frequency as a function of magnetic field on top of experimental data in figure 5.13(c), and there is a small discrepancy at the anti-crossings near 3.5 T, an expanded view of which is given in panel fig. 5.13(d). At this anti-crossing, the MF-RPA model predicted a "multi-anti-crossing" due to the excitation modes being not completely degenerate locally, which is not visible in the experimental data, suggesting a potential deficiency of the MF model. However, we make a remark about an observation of the raw data: while the lower branch has a long tail with vanishing amplitudes going from low to high field, the the upper branch at the anti-crossing doesn't exhibit such a tail symmetrical to the lower one, but rather it starts abruptly with a broad peak at the anti-crossing, potentially due to spectral diffusion that would necessarily implies non-degenerate excitation modes. The spectroscopic method in the present report failed to resolve this feature at better resolution, we hence reserve the discussion of it for future work when more detailed experimental data is available.

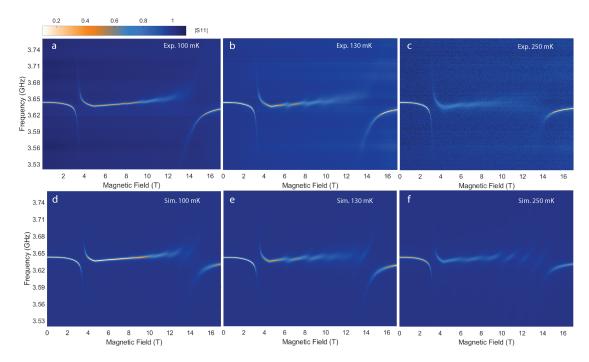


Figure 5.17: (a-c) Experimental data of  $|S_{11}|$  measured at 100, 130, and 250 mK. (d-f) Simulation of (a-c) using the single-ion susceptibilities.

An important and controversial issue involving LiHoF4 is the soft mode near the quantum critical point. Previous literature has suggested a complete softening of the first excited electro-nuclear state at QPT[48]. Only recently, experimental evidence[45] has emerged surrounding this soft mode, but the issue is far from concluded. In search of this soft mode, we therefore repeat on-resonance measurement at five different frequencies as indicated earlier in figure 5.1 on the same sample. The overview of measured  $|S_{11}|$  is given in color maps in figure 5.18(a), and avoid-crossing-patterns that are tokens of mode hybridization can be observed over a wide frequency range until 2.2 GHz. By contrasting these sets of data, the absence of experimental evidence of mode hybridization below 2.2 GHz imply that no excitation mode visibly softened through this frequency. This combined with the previous observation of that the two dissipative peaks in off-resonance data surrounding the critical field are found both above and below first order excitation spectra of the electronic ground state manifold, it is safe to draw the conclusion that no single-ion electro-nuclear state softens completely at QPT. However, limited by the MF-RPA approach, we could not explain the aforementioned double peaks around the critical point, nor rule out existence of collective modes that soften completely at QPT in LiHoF4 .

For comparison to MF results, we plot calculated excitation spectra with the fundamental mode highlighted in red on top of experimental data in figure 5.18(a). Over a large frequency and field range, calculated results appear to predict correctly locations of mode hybridization, particularly for those at higher frequencies shown in more detail in figure 5.18(b). However, at lower frequencies, expanded views in fig. 5.18(c, d, e) reveal some discrepancies. Most importantly, the anti-crossing patterns in the experimental data in panel (b) clearly suggest at least three spin modes present locally yet the MF calculation predicted that only the fundamental mode is in the vicinity. Since where the mode hybridization takes place in this case is very close to the critical point, it is not a complete surprise that MF prediction fails here, but the difference between experimental data and MF calculations is striking. We thus refrain from further interpretation of experimental data with MF-RPA calculations and leave for future endeavor the search of a suitable model in this particular region of phase space.

#### 5.2.2 High Power Excitation

For the very last presentation of experimental data, we briefly discuss the power dependence of measured  $|S_{11}|$ . The motivation for investigating excitation power dependence is two fold: 1. Since the foundation of our quantitative analysis is linear response theory,

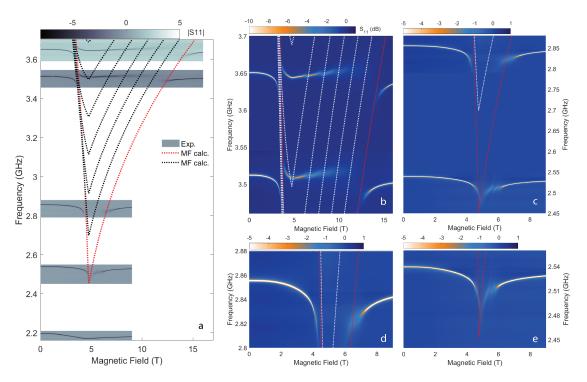


Figure 5.18: (a) Color map: experimental data of  $|S_{11}|$  measured at 130 mK near 2.2, 2.5, 2.8, 3.5, and 3.6 GHz. (b) Expanded view of (a) between 3.45 GHz and 3.7 GHz. (c) Expanded view of (a) between 2.45 GHz and 2.56 GHz. (d, e) Isolated and expanded view of (c). Dotted lines in all panels: the  $\delta I^z=1$  excitation spectra of LiHoF<sub>4</sub> from MF calculations with the mode originating from the ground state colored in red.

it is imperative to keep probing field power down in the perturbative regime in order for the analysis to be valid; 2. Since at low temperatures ( $\leq 400$  mK), the upturning of the magnetic phase boundary of LiHoF<sub>4</sub> is caused by the mixing of nuclear spin states with the electronic spin states, there exists an intuitive and appealing idea of driving the quantum phase transition by actively decoupling the nuclear spin degree of freedom from that of electronic spin via population inversion of the hyperfine levels. It was proposed theoretically that it can be done using AC magnetic field modulation[41, 28]. As far as the author is concerned, there hasn't been any report of experimental success on the effort.

We first establish the perturbative regime, this is done by both searching for the heating effect from the RF excitation, and comparing  $|S_{11}|$  signal change among different excitation powers  $(P_{ex})$ . To maximize the change, we use small samples  $(\vec{a} \times \vec{b} \times \vec{c} = 2.5 \times 1.0 \times 0.5 \text{ mm})$  so that the saturation limit is lower and hence easier to reach. In figure 5.19(a), we present experimentally measured  $|S_{11}|$  at 400 mK and  $P_{ex}=-10$  dBm, or equivalently 0.1 mW, and the expected anti-crossing pattern is clearly visible around 2.5 T below the critical

field. The measurement was repeated at the same temperature and  $P_{ex}$  = -30 dBm (0.001 mW), -20 dBm (0.01 mW), and the peak intensity at each magnetic field is recorded and plotted together in figure 5.19(c). No significant difference was found among the three sets of data, particularly at 2.3 T where the magnon modes are expected to hybridize with the cavity mode, which indicate all three values for the excitation power are well below the saturation limit in the linear response regime.

Having established the baseline, the power is increased in order to reach or approach the saturation limit. Experimental data of  $|S_{11}|$  collected with an excitation power at +15 dBm (~ 32 mW) is presented in figure 5.19(b) for a side-by-side comparison to (a), and there is an apparent and dramatic change in the line shape as well as noise level. At higher excitation powers, the avoid crossing patter disappears, and the measured  $|S_{11}|$  appears to be single peaked at the entire field range. Violent fluctuation of both peak position and peak intensity emerges near the location where mode hybridization would have been, accompanied by large heating effect: the dilution fridge was kept at the base temperature ~ 100 mK before the RF signal was turned on to sweep continuously, after which measured temperature of the cavity eventually stabilizes at ~ 400 mK. This provides a retrospective explanation for the choice of 400 mK to collect power-dependence data at low excitation powers. In other words, it was determined by the temperature of the steady state at the highest RF excitation power, all measurements at lower powers were carried our subsequently by stabilizing the cavity at the same temperature in order to have a valid comparison.

We similarly collected the same peak intensity data shown in figure 5.19(c) for  $P_{ex}=0$  dBm (1 mW), +7 dBm (~ 5 mW), and +15 dBm (~ 32 mW), the results are plotted together with that for  $P_{ex}=-30$  dBm (0.001 mW) in figure 5.19(d). In addition to the elevated noise level, the peak intensities at 2.4 T are significantly reduced comparing to that under  $P_{ex}=-30$  dBm. Though we have yet to develop a quantitative model to account for the observation, a hand-waving interpretation purely from physical intuition is attainable. Consider the extreme case of reaching the saturation limit, where photon emission and absorption rates reach a dynamical equilibrium, which diminishes further coherent energy exchange between the magnon modes and cavity mode, effectively cutting off the coupling between the subsystem. As a consequence, the spectroscopic signal from the cavity should reflect this decoupling by returning to the line shape of an empty cavity. In the present case, this means the measured  $|S_{11}|$  should return to being single peaked and field-independent. In figure 5.19(b), the situation can thus be deemed to be in between the above extremity and

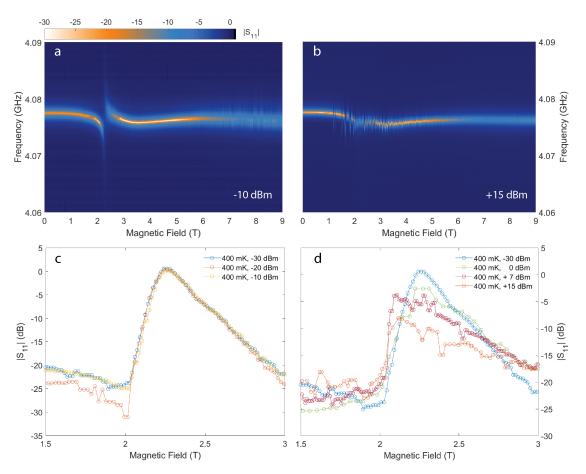


Figure 5.19: (a) Experimentally measured  $|S_{11}|$  at 400 mK and -10 dBm RF excitation power as a function of magnetic field and frequency. (b) Same measurement as (a) but at +15 dBm. (c) Peak amplitude of experimentally measured  $|S_{11}|$  at 400 mK and different excitation powers in the perturbative regime. (d) Same measurement as (c) but with excitation powers near the saturation limit.

perturbative regime, where the photon absorption rate is approaching the saturation limit, and hence reduces density of state for the magnon modes, lowering its effective coupling to the cavity field.

It is important to note that electro-nuclear excitations in  $LiHoF_4$  do couple to phonons, and consequently the energies these magnons carry dissipate in the form of heat as well, which is particularly pronounces at high RF excitation power and in CW mode. However, even at higher temperatures, magnon modes would nonetheless cross path, and hence hybridize, with the cavity mode, which would manifest as avoid-crossing patterns as usual should the coupling strength, that hinges on the population factor, is strong enough. Thermal excitations from simple heating effect would not level the population distribution enough

#### Chapter 5. Experimental results and discussion

to suppress completely the branching of resonance frequency.

Furthermore, as figure 5.19(c) shows that the hybridization between the cavity mode and the magnon modes results in a peak in the minimal  $|S_{11}|$  along the field axis, one can infer from figure 5.19(d) the locations of such hybridization, from which it is clear that the sample temperatures at higher RF excitations aren't far from the those at lower RF excitation powers. This on the one hand lends support for comparing data under different RF excitation powers at the same nominal temperature, and on the other hand implies a continuous and gradual change as the excitation power is raised, in contrast to the qualitatively different appearances between 5.19(a) and 5.19(b).

However, one should be bear in mind that, due to the continuous nature of the current experimental setup, although measurements were taken at steady states, they aren't necessarily measurements of equilibrium states. Consequently, the usual magnetic phase transition and critical point for  $LiHoF_4$  may be ill defined in this case. In author's opinion, in order to meaningfully discuss change of the magnetic phase of  $LiHoF_4$  in response to the decoupling of electronic and nuclear degrees of freedom, measurements of transient states with pulsed RF excitation is a better suited experimental scheme for the purpose.

### 6 Summary & Outlook

In summary, we have carried out both on-resonance and off-resonance measurements of  $|S_{11}|$ , at dilution temperatures and across a wide magnetic field range that encloses a quantum critical point (QCP), on a cavity-magnon-polariton system that consists of a high-finesse reentrant cavity and a single crystal of LiHoF4. The theoretical model, based on the mean field theory (MFT), generalized susceptibility in linear response regime, and input-output formalism, that we have developed can adequately explain and simulate direct experimental observations over a large area in the phase space, and is capable of being readily applied to other systems alike owing to its generality. Through offresonance experiment, we demonstrated reliable measurement method on the AC magnetic susceptibility of LiHoF<sub>4</sub>, which can in turn be used to map out its magnetic phase diagram, and detect weakly interacting or fast decohering modes such as the soft mode predicted by RPA calculations[48, 45]. In the meantime, on-resonance experiments have shown the possibility of strongly hybridizing a cavity photon field at a few GHz with individual electro-nuclear spin states in LiHoF<sub>4</sub>. Furthermore, we have taken the first experimental step of illustrating the potential of driving a dynamical quantum phase transition through high power magnon pumping.

However, we have conversely also shown that some significant inconsistencies exist between RPA predictions and experimental results. More specifically, we have demonstrated that the MFT calculations appear to consistently show better agreement with the experimental data than the MF-RPA calculations in many aspects (fig. 5.4, fig. 5.16, etc). Moreover, despite of that both Ref. [45] and the present work have found indications of the soft mode predicted by RPA in the experimental data (fig 5.9), major difficulties persist for the MF-RPA calculation to reproduce experimental results (fig. 5.8). Although this

difficulty was addressed in Ref. [49] and attributed to the extremely short coherence time ( $\sim 1~\rm ps$ ) of the collective mode, large discrepancies, such as the line shapes of the resonant frequencies, is not eliminated by this explanation. Furthermore, another disagreement of great importance takes place at frequencies above 2 GHz but below 3 GHz and near QCP, where the experimental data (fig. 5.18 (c-e)) showed clear signatures of strong hybridization between the cavity mode and spin excitation modes in LiHoF4, yet it is not predicted by either the MFT nor the MF-RPA calculations. These unexplained yet unequivocal features may signal non-trivial physics that is yet to be described by our current model, and raise important questions with respect to the nature of quantum phase transition in LiHoF4 as well as the expected soft mode. With the progress and puzzles, we summarize bellow some promising prospects of LiHoF4 as a quantum magnet lay ahead that could be further studied using RF spectroscopy:

- As mentioned above, in spite of the success of the MFT description of LiHoF $_4$  over a vast area of the parameter space, major discrepancies between theoretical and experimental results for both off- and on-resonance measurements of  $|S_{11}|$  persist and cannot be cured by the RPA corrections. These issues are particularly pronounced at low frequencies as demonstrated in fig. 5.8 and fig. 5.18. For the former example, existing data suggest that the required revision to the model is beyond simple scaling, while for the latter, the multiple features of unclear origins open doors to many possibilities. Therefore, more sophisticated model beyond MF-RPA is needed to adequately account for the discrepancies, the resolution of which is likely to provide new insights into the quantum criticality in LiHoF $_4$ .
- One of the central issues concerning LiHoF<sub>4</sub> is the soft mode at the QCP. The double peaks in the imaginary part of AC magnetic susceptibility at low frequencies indeed suggest weak hybridization to such collective modes (fig. 5.9 (d)), that soften near the QCP to energies below the cavity resonance frequencies used in either the present work or in the previous literature[48, 45]. However, at the same time, the RPA that predicts such a soft mode also creates more difficulties than explanations to the experimental observations in nearly all other aspects, which casts doubts on the truthfulness of the MF-RPA picture, including its description of the collective mode. Thus more quantitative comparison between experimental and theoretical data is needed for a better understanding of these collective modes.
- In matters related to the soft mode in LiHoF<sub>4</sub>, similar dual peaks were observed in the experimental data of the imaginary part of AC susceptibility at frequencies

much higher than the predicted soft mode (fig. 5.5). These features are not explained by neither the MFT or the MF-RPA. In consideration of their similarities to the manifestation of the soft mode in LiHoF<sub>4</sub> and yet distinctively different behaviors. It is in the author's opinion that it is worth the effort to attempt understanding their mechanisms. One possible origin of these modes could arise if the next-nearest-neighbor-state excitation spectra is dramatically revised (e.g. lowered in energy) due to higher order effects, then the cavity mode can potentially cross path with these magnon modes in this frequency window (fig. 5.1 (a)). Then according to fig. 3.11,  $\chi_{zz}$  may only produces a weak coupling to the cavity mode, resulting in the fable signals that we see in fig. 5.5 (b). However, given that this is the first observation of these features and hence only limited data exists, both experimental and theoretical work are likely required for further study.

- In both Fig. 5.9(a, b) and fig. 5.6(a), we see strong disturbance of cavity resonant frequency, potentially caused by mode hybridization with the magneto-static mode known as the Walker mode with extremely fine line width. Due to its close relation to the geometry of the sample at macroscopic level, a strong coupling of it to the photon field in an RF cavity is thus very relevant and interesting for investigations of magnetic domain dynamics.
- Not until recently, some progresses were made in advancing the theoretical description of the high temperature part of the phase diagram for LiHoF<sub>4</sub> [19], and a complete theoretical description of LiHoF<sub>4</sub> in this regime is still out of reach. Furthermore, as it has been shown both in Ref.[63] and the present experiment that the high temperature part of the phase boundary appears to exhibit re-entrance character that may signal some type of ordering instability. Given the fact that LiHoF<sub>4</sub> is one of the best materialization of the 3D Ising magnet, an understanding of its critical behavior potentially has profound impact. It is therefore well worth the effort to complete our grasp of the system near critical points. However, at the moment, detailed data on the subject in this part of phase space remain scarce, thus further work on both experimental and theoretical front are much needed.
- Last but not the least, both theoretical and experimental results have attributed the enhancement of critical field to the hyperfine interaction present in LiHoF<sub>4</sub>. This in turn motivated the question of whether or not this effect, and subsequently its influence on the phase boundary, can be removed by decoupling the nuclear spin degree of freedom of from that of electronic spins. In principle, this is achievable

#### Chapter 6. Summary & Outlook

through the so called "population inversion" by active pumping of spins to excited state as briefly discussed in the last part of Chpt. 5. In spite of a potentially strong magnon-polariton coupling that could lead to heating effect, it is entirely foreseeable to reach, in a pulse experiment, a transient/non-equilibrium state with skewed Boltzmann distribution of spins before the energy dissipates as heat[28], so that one avoids the potential confusion from crossing the phase boundary by warming up the sample. Being able to drive the quantum phase transition with RF electromagnetic wave would then open doors for many interesting research topics such as non-equilibrium states and spin dynamics near quantum phase transition.

# A MF-RPA Susceptibility Tensor

Applying Eq. 2.11 and Eq. 2.15 to all combinations of Cartesian component pairs, the imaginary part of AC susceptibility tensors are calculated for LiHoF $_4$  at 300 mK. The results calculated under the mean field (MF) approximation and the random phase approximation (RPA) are presented respectively in figure A.1 and figure A.2 as functions of external magnetic field and frequency. The panels arrangement are in accordance with the placement of tensor elements:

$$\bar{\bar{\chi}} = \begin{pmatrix} \chi_{xx} & \chi_{xy} & \chi_{xz} \\ \chi_{yx} & \chi_{yy} & \chi_{yz} \\ \chi_{zx} & \chi_{zy} & \chi_{zz} \end{pmatrix}$$
(A.1)

the relative amplitude between different tensor elements clearly show, for both MF and RPA results, that the element  $|\chi_{zz}|$  has the largest amplitude, implying the strongest AC magnetic response to the EM field polarized along this orientation.

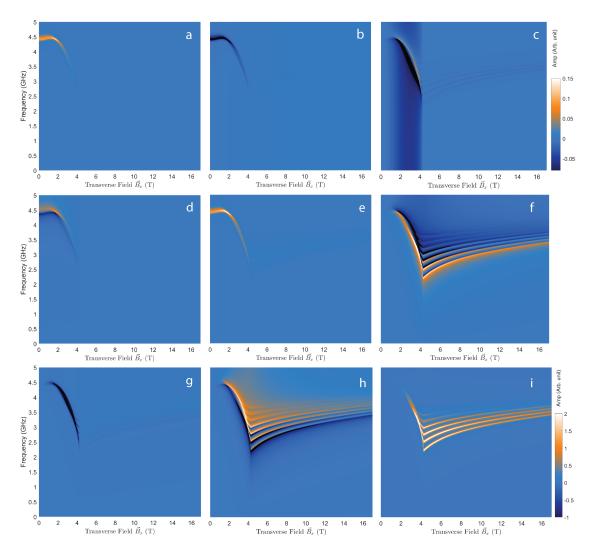


Figure A.1: (a-i) Matrix elements of MF susceptibility of LiHoF $_4$  at 300 mK and in magnetic field up to 17 T. The arrangement of the panels is consistent with the elements' relative location within the susceptibility tensor. All panels except for (i) share the color scale in (c), and panel (i) uses its own color scale for clarity.

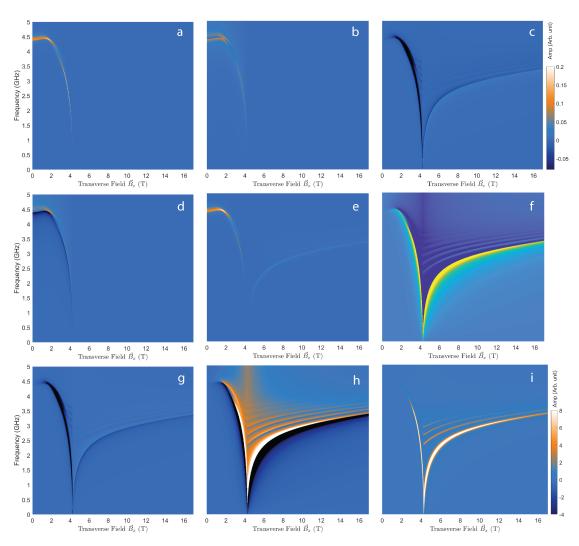


Figure A.2: (a-i) Matrix elements of MF-RPA susceptibility of LiHoF $_4$  at 300 mK and in magnetic field up to 17 T. The arrangement of the panels is consistent with the elements' relative location within the susceptibility tensor. All panels except for (i) share the color scale in (c), and panel (i) uses its own color scale for clarity.

### **B** CEF parameter choice

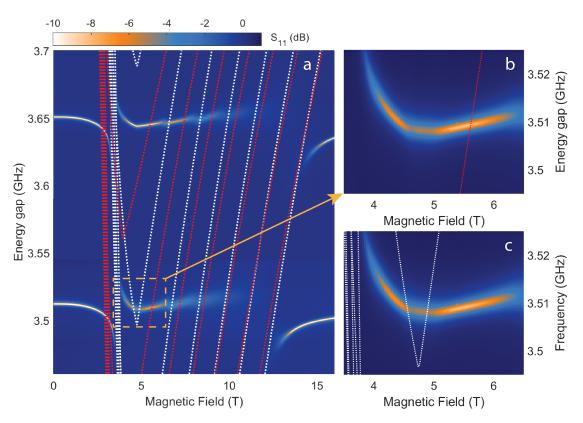


Figure B.1: (a) Colormap: Experimentally measured  $|S_{11}|$  parameter with cavities having resonance frequencies at 3.52 and 3.65 GHz respectively. Data were taken separately on the same single crystal of LiHoF<sub>4</sub> and then stitched together postproduction. (b, c) Expanded views of the same region singled out by the yellow dashed box in (a). White dashed lines in all panels represent calculated magnon modes in LiHoF<sub>4</sub> using adjusted CEF parameters. Red dashed lines in all panels represent calculated magnon modes in LiHoF<sub>4</sub> using the original values of CEF parameters supplied in Ref. [61].

#### Appendix B. CEF parameter choice

Coefficient	$10^3 B_2^0$	$10^3 B_4^0$	$10^3 B_6^0$	$10^3 B_4^4(c)$	$10^3 B_4^4(s)$	$10^6 B_6^4(c)$	$10^6 B_6^4(s)$
Ref. [4] Value	-57.9	+0.309	+0.54	+3.51	0.00	+63.1	+17.1
Uncertainty[4]	±3.2	$\pm 0.047$	±0.13	$\pm 0.60$	_	±12.0	±3.3
Ref. [61] Value	-60.0	+0.350	+0.40	+3.60	0.00	+70.0	±9.8
Present report	-60.0	+0.350	+0.40	+3.60	0.00	+65.5	+9.8

Table B.1: The crystal field parameters used in Ref. [61] and the present work.

For all the calculations carried out in the present study, we adopt the same set of expansion coefficients for the Steven's operators from Ref. [61] with minor revision, both of which are given in Table B.1. The 0.7% adjustment of coefficient  $B_6^4(c)$  comes from noting a weak hybridization between the cavity mode and the magnon mode between |6\rangle nad |7\rangle at 3.51 GHz and near 4.8 T. The experimental data is shown in colormaps in figure B.1(ac) with panel (b, c) being the zoomed-in displays of the same region singled out by the yellow dashed square in panel (a). In all three panels of fig. B.1, the white dashed lines are magnon modes calculated under MF approximation using adjusted CEF parameters, whereas the red dashed lines are those calculated from the original values. It is easy to see in Fig. B.1(a) that there is a large discrepancy between the two results with the one with adjusted parameters providing a much better agreement with the experimental data. In fig. B.1(b), a small feature can be spotted near 5 T along the cavity resonance line, yet the predicted MF mode from the original set of CEF parameters is located far away from the feature. In the meantime in fig. B.1(c), the calculated modes from adjusted CEF parameters yield a very precise coincidence between predicted location of hybridization and that of experimentally observed feature. Further prompting the choice of the latter for all computations of the present study.

However, in a more recent report, by fitting to experimental data from neutron powder diffraction measurement, a different set of parameters, which is also given in Table B.1. To again compare results from the literature and our values, we repeat the same calculations from the two sets of CEF parameters and compare to the experimental data. The results are presented in In fig. B.1(a), where again the white dashed lines are computed from adjusted CEF parameters and the red ones are from those provided in Ref. [4]. Again the results from the former set of parameters yield a visibly better agreement with the experimental data.

Since the set of CEF parameters from Ref. [4] was obtained by fitting to experimental data

as well. We further compare the three sets of parameters by computing from them the zero field CEF levels at 4 K. We first include, in fig. B.2 (b), the original experimental data and corresponding fit from Ref. [4], in which markers represent experimental data and the solid red curve represents the fit. Then we plot in figure B.2 (c) calculated crystal field levels from the three sets of CEF parameters tabulated in Tab. B.1 together. Immediately we can see that all three curves capture the lowest peak around 1 meV adequately while missing the small peak at 5 meV completely. In addition, they disagree with one another to varying degrees for all other small peaks located near 2 and 8 meV. It's worth noting that the parameters used in the present study, despite being numerically very close to those from Ref. [61] (identical except for the minor difference in  $B_l^4(s)$ ), produced a result that agrees much better with the experimental data and corresponding fit from Ref. [4] at higher energies between 5 and 8 meV than the original values. However, it also produced a large discrepancy from the experimental data for the peak located near 3 meV.

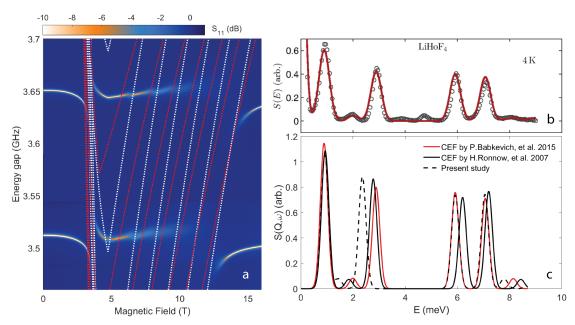


Figure B.2: (a) Colormap: Experimentally measured  $|S_{11}|$  parameter with cavities having resonance frequencies at 3.52 and 3.65 GHz respectively. Data were taken separately on the same single crystal of LiHoF<sub>4</sub> and then stitched together postproduction. White dashed lines: calculated magnon modes in LiHoF<sub>4</sub> using adjusted CEF parameters. Red dashed lines: calculated magnon modes in LiHoF<sub>4</sub> using the CEF parameters provided in Ref. [4]. (b) Original neutron powder diffraction data and corresponding fit from Ref. [4]. Figure credit: Ref. [4]. (c) Calculated differential scattering cross-section of LiHoF<sub>4</sub> using CEF parameters tabulated in Tab. B.1.

### **Bibliography**

- [1] Abe, Eisuke, Wu, Hua, Ardavan, Arzhang, Morton, and John JL. Electron spin ensemble strongly coupled to a three-dimensional microwave cavity. *Applied Physics Letters*, 98(25):251108, 2011.
- [2] C. Ancona-Torres, D. M. Silevitch, G. Aeppli, and T. F. Rosenbaum. Quantum and classical glass transitions in  $\text{LiHo}_x Y_{1-x} F_4$ . *Physical Review Letter*, 057201, 2008. ISSN 101.
- [3] J-P. Ansermet. Spin Dynamics-Foundation for Spintronics. In preparation, 2021.
- [4] P. Babkevich, A. Finco, M. Jeong, B. D. Piazza, I. Kovacevic, G. Klughertz, K. W. Krämer, C. Kraemer, D. T. Adroja, E. Goremychkin, T. Unruh, T. Stässle, A. D. Lieto, J. Jensen, and H. M. Rønnow. Neutron spectroscopic study of crystal-field excitations and the effect of the crystal field on dipolar magnetism in LiRF<sub>4</sub> (R = Gd, Ho, Er, Tm, and Yb). *Physical Review B*, 92(144422), 2015.
- [5] L. Bai, M. Harder, P. Hyde, Z. Zhang, C-M. Hu, Y. P. Chen, and J. Q. Xiao. Cavity mediated manipulation of distant spin currents using a cavity-magnon-polariton. *Physical Review Letter*, 118:217201, 2017.
- [6] P. Beauvillain and J. P. Renard. Critical behavior of the magnetic susceptibility of the uniaxial ferromagnet LiHoF<sub>4</sub>. *Physical Review B*, 18(7):714–715, 1978. ISSN 3360-3368.
- [7] P. Beauvillain, J. P. Renard, and J. Magarino. Determination of crystal field parameters of LiReF<sub>4</sub> (R = Tb, Ho, Er) by high temperature susceptibility measurements. Journal of Magnetism and Magnetic Materials, 15-18:31–32, 1980.
- [8] M. X. Bi, X. H. Yan, Y. Xiao, and C. J. Dai. Magnon dark mode in a strong driving microwave cavity. J. Appl. Phys., 173902, 2019. ISSN 126. doi: 10.1063/1.5121618.

- [9] D. Bitko, T. F. Rosenbaum, and G. Aeppli. Quantum critical behavior for a model magnet. *Physical Review Letters*, 77(5):940, 1996.
- [10] G. Boero, G. Gualco, R. Lisowski, J. Anders, D. Suter, and J. Brugger. Room temperature strong coupling between a microwave oscillator and an ensemble of electron spins. *Journal of Magnetic Resonance*, 231:133–140, 2013.
- [11] I. Boventer, C. Dörflinger, T. Wolz, R. Macêdo, R. Lebrun, M. Kläui, and M. Weides. Control of the coupling strength and linewidth of a cavity magnon-polariton. *Physical Review Research*, 2:013154, 2020.
- [12] H. P. Breuer and F. Petruccione. The Theory of Open Quantum Systems. Oxford University Press, 2010.
- [13] P. B. Chakraborty, P. Henelius, H. Kjønsberg, A. W. Sandvik, and S. M. Girvin. Theory of the magnetic phase diagram of LiHoF<sub>4</sub>. *Physical Review B*, 144411, 2004. ISSN 70.
- [14] T. J. Clark, V. Vadakkumbatt, F. Souris, H. Ramp, and J. P. Davis. Cryogenic microwave filter cavity with a tunability greater than 5 GHz. *Rev. Sci. Instr.*, 114704, 2018. ISSN 89. doi: 10.1063/1.5051042.
- [15] A. A. Clerk, M. H. Devoret, S. M. Girvin, F. Marquardt, and R. J. Schoelkopf. Introduction to quantum noise, measurement, and amplification. *Rev. Mod. Phys.*, 82, 2010. ISSN 1155. doi: 10.1103/RevModPhys.82.1155.
- [16] Kevin C. Cox, David H. Meyer, Zachary A. Castillo, Fredrik K. Fatemi, and Paul D. Kunz. Spin-wave multiplexed atom-cavity electrodynamics. *Physical Review Letter*, 123, 2019. ISSN 0031-9007. doi: 10.1103/physrevlett.123.263601.
- [17] W. Dankworth and J. Ferch. Reevaluation of the atomic  $g_J$ -factor and the nuclear  $g_I$ -factor of  $^{165}$ Ho.  $Z.\ Physik.$ , 267:239, 1973.
- [18] R. H. Dicke. Coherence in spontaneous radiation processes. *Physical Review*, 93: 99–110, 1954. ISSN 0031-899X. doi: 10.1103/physrev.93.99.
- [19] T. Dollberg, J. C. Andresen, and M. Schechter. Effect of intrinsic quantum fluctuations on the phase diagram of anisotropic dipolar magnets. *Physical Review B*, 105 (L180413), 2022.
- [20] P. Fazekas. Lecture Notes on Electron Correlation and Magnetism. World Scientific Publishing Co., 1999.

- [21] J-M. Le Floch, Y. Fan, M. Aubourg, D. Cros, N. C. Carvalho, Q. Shan, J. Bourhill, E. N. Ivanov, G. Humbert, V. Madrangeas, and M. E. Tobar. Rigorous analysis of highly tunable cylindrical transverse magnetic mode re-entrant cavities. *Rev. Sci. Instr.*, 125114, 2013. ISSN 84. doi: 10.1063/1.4848935.
- [22] Graeme Flower, Maxim Goryachev, Jeremy Bourhill, and Michael E. Tobar. Experimental implementations of cavity-magnon systems: from ultra strong coupling to applications in precision measurement. *New J Phys*, 21:095004, 2019. ISSN 1367-2630. doi: 10.1088/1367-2630/ab3e1c.
- [23] C. W. Gardiner and M. J. Collett. Input and output in damped quantum systems: Quantum stochastic differential equations and the master equation. *Physical Review A*, 31, 1985. ISSN 3761. doi: https://doi.org/10.1103/PhysRevA.31.3761.
- [24] C. W. Gardiner, A. S. Parkings, and P. Zoller. Wave-function quantum stochastic differential equations and quantum-jump simulation methods. *Physical Review A*, 7, 1992. ISSN 46.
- [25] J. C. Garrison and R. Y. Chiao. Quantum Optics. Oxford University Press, 2008.
- [26] S. Ghosh, R. Parthasarathy, T. F. Rosenbaum, and G. Aeppli. Coherent spin oscillations in a disordered magnet. *Science*, 296(5576):2195–2198, 2002. doi: 10.1126/science. 1070731.
- [27] M. J. P. Gingras and P. Henelius. Collective phenomena in the  $\text{LiHo}_x Y_{1,x} F_4$  quantum ising magnet: Recent progress and open questions. *J. Phys.: Conf. Ser.*, 320:012001, 2011. doi: 10.1088/1742-6596/320/1/012001.
- [28] A. Gomez-Leon and P. C. E. Stamp. Dynamical quantum phase transitions in presence of a spin bath. *Physical Review B*, 95, 2017. ISSN 054402. doi: 10.1103/PhysRevB.95. 054402.
- [29] M. Goryachev, W. G. Farr, D. L. Creedon, Y-H. Fan, M. Kostylev, and M. E. Tobar. High-cooperativity cavity qed with magnons at microwave frequencies. *Physical Review A*, 054002, 2014. ISSN 2.
- [30] W. Greiner. Quantum Mechanics: Special Chapters, 2nd Ed. Springer, 2001.
- [31] W. Greiner. *Quantum Mechanics: Introduction*. Springer, 2001. doi: 10.1007/978-3-642-56826-8.

- [32] J. A. Griffin, M. Huster, and R. J. Folweiler. Critical behavior of the spontaneous magnetization at marginal dimensionality in LiHoF<sub>4</sub>. *Physical Review B*, 22(9): 714–715, 1980. ISSN 4370-4378.
- [33] V. L. Grigoryan, K. Shen, and K. Xia. Synchronized spin-photon coupling in a microwave cavity. *Physical Review B*, 98:024406, 2018.
- [34] P. E. Hansen, T. Johansson, and R. Nevald. Magnetic properties of lithium rare-earth fluorides: Ferromagnetism in LiErF<sub>4</sub> and LiHoF<sub>4</sub> and crystal-field parameters at the rare-earth and Li sites. *Physical Review B*, 12, 1975. ISSN 11.
- [35] M. Harder, L. Bai, C. Match, J. Sirker, and C-M. Hu. Study of the cavity-magnon-polariton transmission line shape. *Science China*, 59(11):117511, 2016.
- [36] T. Holstein and H. Primakoff. Field dependence of the intrinsic domain magnetization of a ferromagnet. *Physics Review*, 58:1098, 1940. doi: https://doi.org/10.1103/PhysRev. 58.1098.
- [37] H. Huebl, C. W. Zollitsch, J. Lotze, F. Hocke, M. Greifenstein, and A. Marx. High cooperativity in coupled microwave resonator ferrimagnetic insulator hybrids. *Physical Review Letter*, 111:127003, 2013.
- [38] E. T. Jaynes and F. W. Cummings. Comparison of quantum and semiclassical radiation theories with application to the beam maser. *Proc. IEEE*, 51:89–109, 1963. doi: 10.1109/PROC.1963.1664.
- [39] J. Jensen. Rare Earth Magnetism. Clarendon Press, 1991.
- [40] J. Jensen. 1/z renormalization of the mean-field behavior of the dipole-coupled singlet-singlet system HoF<sub>3</sub>. *Physical Review B*, 49(17), 1994.
- [41] I. Kovacevic, P. Babkevich, M. Jeong, J. O. Piatek, G. Boero, H. M. Rønnow, et al. Probing strongly hybridized nuclear-electronic states in a model quantum ferromagnet. *Physical Review B*, 94(21):214433, 2016.
- [42] C. Kraemer, N. Nikseresht, J. O. Piatek, N. Tsyrulin, B. D. Piazza, K. Kiefer, B. Klemke, T. F. Rosenbaum, G. Aeppli, C. Gannarelli, K. Prokes, A. Podlesnyak, T. Strässle, L. Keller, O. Zaharko, K. W. Krämer, and H. M. Rønnow. Dipolar antiferromagnetism and quantum criticality in LiErF<sub>4</sub>. Science, 336(6087):1416–1419, 2012. doi: 10.1126/science.1221878.

- [43] K. Kurokawa. Power waves and the scattering matrix. *Transactions on Microwave Theory and Techniques*, 13, 1965. ISSN 2. doi: 10.1109/TMTT.1965.1125964.
- [44] Melvin Lax. Quantum noise iv. quantum theory of noise sources. *Physical Review*, 145(1):110, 1966.
- [45] M. Libersky, R. D. McKenzie, D.M. Silevitch, P. C. E. Stamp, and T. F. Rosenbaum. Direct observation of collective electronuclear modes about a quantum critical point. *Physical Review Letter*, 207202, 2021. ISSN 127.
- [46] N. Majlis. The Quantum Thoery of Magnetism. World Scientific Publishing Co., 2007.
- [47] G. Matmon, S. A. Lynch, T. F. Rosenbaum, A. J. Fisher, and G. Aeppli. Optical response from terahertz to visible light of electronuclear transitions in LiYF<sub>4</sub>:Ho<sup>3+</sup>. *Physical Review B*, 94(205132), 2016.
- [48] R. D. McKenzie and P. C. E. Stamp. Thermodynamics of a quantum ising system coupled to a spin bath. *Physical Review B*, 97, 2018. ISSN 214430. doi: 10.1103/physrevb.97.214430.
- [49] R. D. McKenzie, M. Libersky, D. M. Silevitch, and T. F. Rosenbaum. Thermodynamics of a quantum ising system coupled to a spin bath. *Physical Review A*, 106, 2022. ISSN 043716. doi: 10.1103/PhysRevA.106.043716.
- [50] L. McKenzie-Sell, J. Xie, C.-M. Lee, J. W. A. Robinson, C. Ciccarelli, and J. A. Haigh. Low-impedance superconducting microwave resonators for strong coupling to small magnetic mode volumes. *Physical Review B*, 99:140414, 2019.
- [51] G. Mennenga, L. J. de Jongh, and W. J. Huiskamp. Field dependent specific heat study of the dipolar ising ferromagnet LiHoF<sub>4</sub>. Journal of Magnetism and Magnetic Materials, 44:59–76, 1984.
- [52] P. Meystre and M. Sargentill. *Elements of Quantum Optics*, 4th edition. Spinger, 2007.
- [53] K. Momma and F. Izumi. Vesta3 for three-dimensional visualization of crystal, volumetric and morphology data. J. Appl. Cryst., 1272, 2011. ISSN 44. doi: 10.1107/S0021889811038970.
- [54] A. Morin, C. Lacroix, and D. Menard. Effect of dipolar interactions on cavity magnon polarions. *Physical Review B*, 102:224421, 2020.

- [55] T. Niemczyk, F. Deppe, H. Huebl, E. P. Menzel, F. Hocke1, M. J. Schwarz, J. J. Garcia-Ripoll, D. Zueco, T. Hümmer, E. Solano, A. Marx, and R. Gross. Circuit quantum electrodynamics in the ultrastrong-coupling regime. *Nature Physics*, page 772–776, 2010. ISSN 6. doi: 10.1038/nphys1730.
- [56] W. Nolting and A. Ramakanth. Quantum Theory of Magnetism. Springer, 2009.
- [57] I. Proskurin, R. Macedo, and R. L. Stamps. Microscopic origin of level attraction for a coupled magnon-photon system in a microwave cavity. *New J. Phys.*, 21:095003, 2019. doi: 10.1088/1367-2630/ab3cb7.
- [58] J. A. Quilliam, S. Meng, C.G.A. Mugford, and J.B. Kycia. Evidence of spin glass dynamics in dilute LiHo<sub>x</sub>Y<sub>1..x</sub>F<sub>4</sub>. *Physical Review Letters*, 101(187204), 2008.
- [59] B. Z. Rameshti, S. V. Kusminskiy, J. A. Haigh, K. Usami, D. Lachance-Quirion, Y. Nakamura, C-M. Hu, H. X. Tang, G. E.W. Bauer, and Y. M. Blanter. Cavity magnonics. *Physics Reports*, 979:1–61, 2022. ISSN 0370-1573.
- [60] H. M. Rønnow, R. Parthasarathy, J. Jensen, G. Aeppli, T. F. Rosenbaum, and D. F. McMorrow. Quantum phase transition of a magnet in a spin bath. *Science*, 308(5720): 389–392, 2005.
- [61] H. M. Rønnow, J. Jensen, R. Parthasarathy, G. Aeppli, T. F. Rosenbaum, D. F. McMorrow, and C. Kraemer. Magnetic excitations near the quantum phase transition in the ising ferromagnet LiHoF<sub>4</sub>. *Physical Review B*, 75(5), 2007.
- [62] T. F. Rosenbaum, W. Wu, B. Ellman, and J. Yang. Dipolar ferromagnets and glasses. J. Appl. Phys., 5946, 1991. ISSN 70. doi: 10.1063/1.350087.
- [63] F. S. A. Rucker. *Transverse Susceptibility of Complex Magnetic Textures*. PhD thesis, Technische Universität München, Arcisstraße 21, 80333 Munich, 2018.
- [64] S. Sachdev. Quantum Phase Transition. Cambridge Press, 2011.
- [65] Subir Sachdev. Atom in a damped cavity. Physical Review A, 29(5):2627, 1984.
- [66] D.I. Schuster, A.P. Sears, E. Ginossar, L. DiCarlo, L. Frunzio, J..J.L. Morton, H. Wu, G.A.D. Briggs, B.B. Buckley, D.D. Awschalom, and R.J. Schelkopf. High-cooperativity coupling of electron-spin ensembles to superconducting cavities. *Physical Review Lett*, 105:140501, 2010.
- [67] M. O. Scully and M. S. Zubairy. Quantum Optics. Cambridge University Press, 1997.

- [68] D. M. Silevitch, D. Bitko, J. Brooke, S. Ghosh, G. Aeppli, and T. F. Rosenbaum. A ferromagnet in a continuously tunable random field. *Nature*, 448:567, 2007.
- [69] Ö. O. Soykal and M. E. Flatté. Strong field interactions between a nanomagnet and a photonic cavity. *Physical Review Letter*, 104:077202, 2010.
- [70] S. Säubert, C.L. Sarkis, F. Ye, G. Luke, and K.A. Ross. Microscopics of quantum annealing in the disordered dipolar ising ferromagnet  $\text{LiHo}_x Y_{1,x} F_4$ . ArXiv, 2021. doi: 10.48550/arXiv.2105.03408.
- [71] J. Sugar. Nuclear magnetic dipole moment of <sup>165</sup>Ho. J. Opt. Soc. A., 58:11, 1968.
- [72] S. M. A Tabei, M. J. P. Gingras, Y. J. Kao, and T. Yavors'kii. Perturbative quantum monte carlo study of LiHoF<sub>4</sub> in a transverse magnetic field. *Physical Review B* 78, 184408, 2008. doi: 10.1103/PhysRevB.78.184408.
- [73] M. Tavis and F. W. Cummings. The exact solution of n two level systems interacting with a single mode and quantized radiation field. *Physics letter A*, 25:714–715, 1967. ISSN 0375-9601. doi: 10.1016/0375-9601(67)90957-7.
- [74] D. F. Walls and G. J. Milburn. Quantum Optics. Springer, 2008.
- [75] Y-P. Wang and C-M. Hu. Dissipative couplings in cavity magnonics. *J. Appl. Phys.*, 127:130901, 2020. doi: 10.1063/1.5144202.
- [76] A. Wendl, H. Eisenlohr, F. Rucker, C. Duvinage, M. Kleinhans, M. Vojta, and C. Pfleiderer. Emergence of mesoscale quantum phase transitions in a ferromagnet. Nature, 609:65, 2022. doi: 10.1038/s41586-022-04995-5.
- [77] R. M. White. Quantum Theory of Magnetism. Springer, 2007.
- [78] Y. Yang, Y-P Wang, J-W. Rao, Y-S. Gui, B-M. Yao, W. Lu, and C-M. Hu. Unconventional singularity in anti-parity-time symmetric cavity magnonics. *Physical Review Letter*, 125, 2020. ISSN 147202. doi: 10.1103/PhysRevLett.125.147202.
- [79] R. W. Youngblood, G. Aeppli, J. D. Axe, and J. A. Griffin. Spin dynamics of a model singlet ground-state system. *Physical Review Letter*, 49(23), 1982.
- [80] X. Zhang, C-L. Zou, N. Zhu, F. Marquardt, L. Jiang, and H. X. Tang. Magnon dark modes and gradient memory. *Nature communication*, page 8914, 2015. ISSN 6. doi: 10.1038/ncomms9914.

### **Bibliography**

[81] X-F. Zhang, C-L. Zou, L. Jiang, and H-X. Tang. Strongly coupled magnons and cavity microwave photons. *Physical Review Letter*, 113:156401, 2014.

## Yikai Yang (杨意凯)

PH D2 435 (station 3), EPFL 1015 Lausanne, VD, CH +41 79 835 06 76 yikai.yang@epfl.ch

#### RESEARCH INTERESTS

- · Collective behavior & Emergent phenomena in many-body systems
- · Quantum phase transitions (QPT) & Critical phenomena
- · Unconventional & Topological superconductors

#### **EDUCATION**

**Doctor of Philosophy** (in progress) in Experimental Physics.

EPFL (September 2018 - September 2022)

Lausanne, VD, Switzerland

Master of Science in Experimental Physics.

University of Alberta (September 2011 - January 2014)

Edmonton, AB, Canada

Bachelor of Science in Theoretical Physics.

Lanzhou University (September 2006 - August 2010)

Lanzhou, GS, China

#### **WORKING EXPERIENCE**

Research Assistant (Supervisor: Dr. Rønnow, H. M. & Dr. Živković, I.) EPFL

Lausanne, VD, Switzerland

- Experimental studies on quantum phase transition and spin dynamics of the hybridized electronuclear spin levels in LiHoF<sub>4</sub> as a long range 3D Ising ferromagnet.
- Experimental studies of emergent magnetic phenomena due to hyperfine interaction in LiHoF<sub>4</sub> in strongly hybridized Cavity-Magnon-Polariton systems.
- Theoretical/numerical studies of effective dimension reduction of critical exponents in LiErF<sub>4</sub> as a 3D dipolar anti-ferromagnet.
- Routine maintenance and repair of the cryogenic laboratory
- Develop interactive demonstration tools (SoliDRIL) for undergraduate solid state physics courses with open source programming.

Salesperson 2014.06 - 2018.07

Flooring Superstore Edmonton, AB, Canada

- Service existing clients, provide project outlines, cost projections, and product suggestions.
- Negotiate sales contracts, manage logistics and keep schedules for projects.
- Coordinate and mediate conflicts among suppliers, contractors, and clients.

129

- Optimize inventories storage, routine maintenance equipment, and update purchase plans.
- Source potential sales lead from both commercial and private customers.

#### Research Assistant (Supervisor: Dr. Davis, J. P.)

University of Alberta

Edmonton, AB, Canada

- Experimental studies on critical temperature enhancement in granular superconducting film (Al-Ge).
- Experimental and theoretical/numerical studies of vortex dynamics in high-temperature superconductor (YBa<sub>2</sub>Cu<sub>3</sub>O<sub>7</sub>).
- Assist experimental studies of Superfluid (<sup>3</sup>He and <sup>4</sup>He) at low dimensions and in confinement.
- Design, Machine, and assemble experimental setups for various cryogenic systems, optical measurement, and gas handling systems in assisting the construction of a new low temperature laboratory.
- Develop graphical user interface (GUI) and established operation procedures for new instruments included various cryogenic, vacuum, and optical systems.

#### Research Assistant (Supervisor: Dr. Xi, L.)

Lanzhou University

Lanzhou, GS, China

- Powder sample synthesis using hydrothermal and solid-reaction methods.
- Experimental studies on AC susceptibility and microwave absorption in CrO<sub>2</sub> as a spintronic material.
- Experimental studies on Tunnel Magnetoresistance (TMR) effects in CrO<sub>2</sub>.
- · Routine maintenance and trouble-shooting on experimental setups.

#### **Teaching Assistant**

University of Alberta & EPFL

Canada & Switzerland

- Teach physics laboratory courses at undergraduate level (1st to 3rd year)
- Grade assignments and exams at undergraduate level (1st to 3rd year)
- Mentor undergraduate/master intern students for semester/thesis projects
- · Assist curriculum and exam design for undergraduate physics course

#### **SKILLS**

- Language: English (fluent), French (A2), Mandarin (native).
- Programming and software: C++, Python, MATLAB, LabView, AutoCAD Inventor, COMSOL, LATEX.
- **Workshop skills**: Operating forklifts; Metal, wood, and plastic Machining (turning, milling, *etc*); Nano/micro fabrication (Focus-ion-beam/electron-beam lithography, photo-lithography).
- First-Aid certified.

#### **PUBLICATIONS**

Y Yang, P Babkevich, R Gaal, I Živković, H Rønnow. "Resolving strongly hybridized electronuclear spin states in LiHoF<sub>4</sub> across a quantum critical point using cavity-magnon-polariton technique" (in preparation)

K Ma, K Gornicka, R Lefèvre, Y Yang, H Rønnow, HO Jeschke, T Klimczuk, and FO von Rohr, "Superconductivity with High Upper Critical Field in the Cubic Centrosymmetric  $\eta$ -Carbide Nb<sub>4</sub>Rh<sub>2</sub>C<sub>1- $\delta$ </sub>", ACS Mater. Au. June 2021.

Z Wang, L Xi, Y Yang, Y Li, X Han, Y Zuo, and J Wang, "Spin-dependent Transport Properties of CrO2 Micro Rod", Nano-Micro Lett. October 2014.

X Rojas, BD Hauer, AJR MacDonald, P Saberi, Y Yang, and JP Davis, "Ultrasonic interferometer for first-sound measurements of confined liquid <sup>4</sup>He", Phys. Rev. B, May 2014.

L Xi and Y Yang, "Ultrawide Band Microwave Absorption Properties of Ultrasound Processed CrO<sub>2</sub>-Paraffin Wax Composites", Jpn. J. Appl. Phys. March 2011.

#### **VOLUNTEER EXPERIENCE**

Patroller & Dispatcher

September 2012 - December 2014

University of Alberta Safewalk Edmonton, AB, Canada

- · Campus patrol in teams for crime prevention.
- Dispatching teams to provide safety escort services for clients.
- Design and optimizing patrolling route and area.
- Handle general and emergency situations. Cooperate with Edmonton Police Service (EPS), Emergency Medical Services (EMS), *etc*.
- Compose written reports on daily basis for meetings, team leaders, and the president of the organization.

**Conference interpreter** 

June 2010 - August 2010

Lanzhou University
Lanzhou, GS, China

- Oral and text translation of conference materials between Chinese and English.
- English tour guide on- and off-campus for conference attendants.